Oxygen Loss in Layered Oxide Cathodes for Li-Ion Batteries: Mechanisms, Effects, and Mitigation

Hanlei Zhang[1, 2], Hao Liu[2], Louis F. J. Piper[2, 3], M. Stanley Whittingham[2] and Guangwen Zhou[1, 2*]

1. Materials Science and Engineering Program & Department of Mechanical Engineering, State University of New York, Binghamton, New York 13902, United States

2. NorthEast Center for Chemical Energy Storage, State University of New York, Binghamton, New York 13902, United States

3. WMG, University of Warwick, Coventry CV4 7AL, United Kingdom

Abstract

Layered lithium transition metal oxides derived from $LiMO_2$ (M = Co, Ni, Mn, etc.) are widely adopted as the cathode of Li-ion batteries for portable electronics, electric vehicles and energy storage. Oxygen loss in the layered oxides is one of the major reasons leading to the cycling-induced structural degradations and the associated fade of electrochemical performances. Herein, we review the recent progress towards understanding the oxygen loss phenomena and resultant structural degradations in the layered oxides. We first present the major driving forces leading to the oxygen loss and then describe the associated structural degradations resulting from the oxygen loss. This is followed by a discussion on the kinetic pathways enabling the oxygen loss. The correlative electrochemical fade from the oxygen loss is then addressed. Finally, we review the possible approaches towards mitigating oxygen loss and the associated electrochemical fade, as well as detailing novel analytical methods for probing the oxygen loss.

*To whom correspondence should be addressed:
gzhou@binghamton.edu

Contents

1. Introduction

Li-ion batteries have been widely used in portable electronics[1,2], electric vehicles[3–5] and grid energy storage[6–11], creating a global business of billions of U.S. dollars.[12–14] In the large family of cathode materials, layered lithium transition metal oxides rise as a shining star, which are generally described with a formula of $LiMO_2$ (M stands for Ni, Co, Mn, Ti, Al, etc. or their combinations) and the crystallographic space group $R\bar{3}m$.[15–20] A capacity of ~200 mAh/g and a cutoff voltage as high as ~4.6 V can be expected from the layered oxides to meet the current requirements in the automotive and electronics industries.[21–24] Nevertheless, these cathodes suffer from fades in output voltage and capacity during service,[6,17,25–27] which have been attributed to the cycling-induced structural degradation.[22,28–31] That is, the transformation of the defect-free layered $R\bar{3}m$ structure into less electrochemically active structures or the formation of unfavorable structural defects.[32–34] To improve the lifetime performance of the layered oxide cathodes, it is critical to investigate the nature of the structural degradations and develop viable synthesis & operation strategies to mitigate the cycling-induced fade in the electrochemical performance.[35–37]

Extensive work has been conducted and reported on the understanding of structural degradations within layered cathodes. The known structural degradation patterns include chemical dissolution,[38–40] phase transformations,[24,41–44] mechanical damage (cathode cracking),[29,45–47] formation of cavities (loss of mass),[48,49] lattice amorphization,[50–52] surface roughing (micro-fracturing),[53,54] etc. Most of the structural degradations are driven by oxygen loss from the crystal lattice of the layered oxides, which results in an undermined oxygen framework and a shifted chemical environment.[55–

[58] Since the oxygen framework provides fundamental support for the whole oxide,[59,60] its damages can further develop into the aforementioned extended structural defects and finally impair the overall electrochemical performance. The correlation between the loss of lattice oxygen and structural degradations has been regarded as a critical issue in understanding the cycling-induced structural and electrochemical degradations.[61–63]

Although lattice oxygen plays a critical role in the structural integrity of the layered cathodes, tracking the activity of oxygen in the cathodes during electrochemical cycling is a technically challenging task. This is because oxygen is a light element and only yields weak signals with electron-beam-based characterization techniques,[64,65] thereby making it difficult to detect. Probing oxygen with spectroscopic methods, such as electron energy loss spectroscopy (EELS),[66–69] X-ray photoelectron spectroscopy (XPS)[70–72] and X-ray imaging[73,74], can sufficiently reveal the chemical condition of oxygen, but they lack the required spatial (nanometer-scale or atomic-level) resolutions to reveal the dynamic evolution of oxygen that typically initiates from the surface region of the cathode partices.[75–78] To overcome the aforementioned difficulties in tracing the oxygen loss, spectroscopic and microscopic techniques were combined in the study of oxygen loss in the past several years.[50,74,79–81] Significant progress has been made in understanding the oxygen-loss induced structural degradations, although *in-situ/operando* techniques are still urgently demanded for directly probing the activity of oxygen and electrochemical cycling induced oxygen evolution. To directly monitor the oxygen evolution dynamics, the characterization techniques should be capable of tracing the activity and reactivity of off-lattice oxygen with sufficient temporal, spatial and energy resolutions.

The last decade has seen an explosion of innovative experimental and modeling methods to interrogate complex materials at multiple scales. Figure 1[82–85] summarizes the state-of-the-art approaches towards probing the oxygen evolution and activity within the layered oxide cathodes. Each of these approaches has its own advantages and disadvantages. While gas analysis methods can directly detect gaseous oxygen released from the electrode,[38,86,87] the electrochemical test is the most feasible approach for revealing the overall kinetics of oxygen loss.[88,89] However, neither approach yields much information regarding the structural or electronic evolution in the cathode. Electron microscopy provides spatially-resolved observations of the oxygen loss kinetics at the atomic level.[90,91] It can also probe the chemical and compositional evolution with the use of EELS and energy dispersive X-ray spectroscopy (EDXS). The local information regarding the morphological, structural, and electronic features from the electron microscopy tools can be complemented with the ensemble chemistry and structure measurements via spectroscopy and X-ray scattering to understand the oxygen-loss induced structural and electronic evolution on the global scale.[92,93] The spectroscopy methods, such as XPS and nuclear magnetic resonance (NMR), can reveal the electron transfer accompanying the oxygen loss, yielding the chemical nature of the lost/released oxygen.[94] In parallel, *in-situ*/*operando* techniques of electron-based imaging and diffraction, as well as synchrotron-based X-ray scattering and imaging have been developed and employed to study the working mechanisms of electrodes and the oxygen-loss induced dynamic properties of cathode materials.[95,96] In addition to the experimental observations, computational and simulation approaches such as the density functional theory (DFT) and molecular dynamics (MD) are useful supplementary tools to address

the atomistic mechanisms of the oxygen loss process. To fully take advantage of their strengths, the aforementioned techniques are usually combined to yield a comprehensive picture of the oxygen loss kinetics and mechanisms.

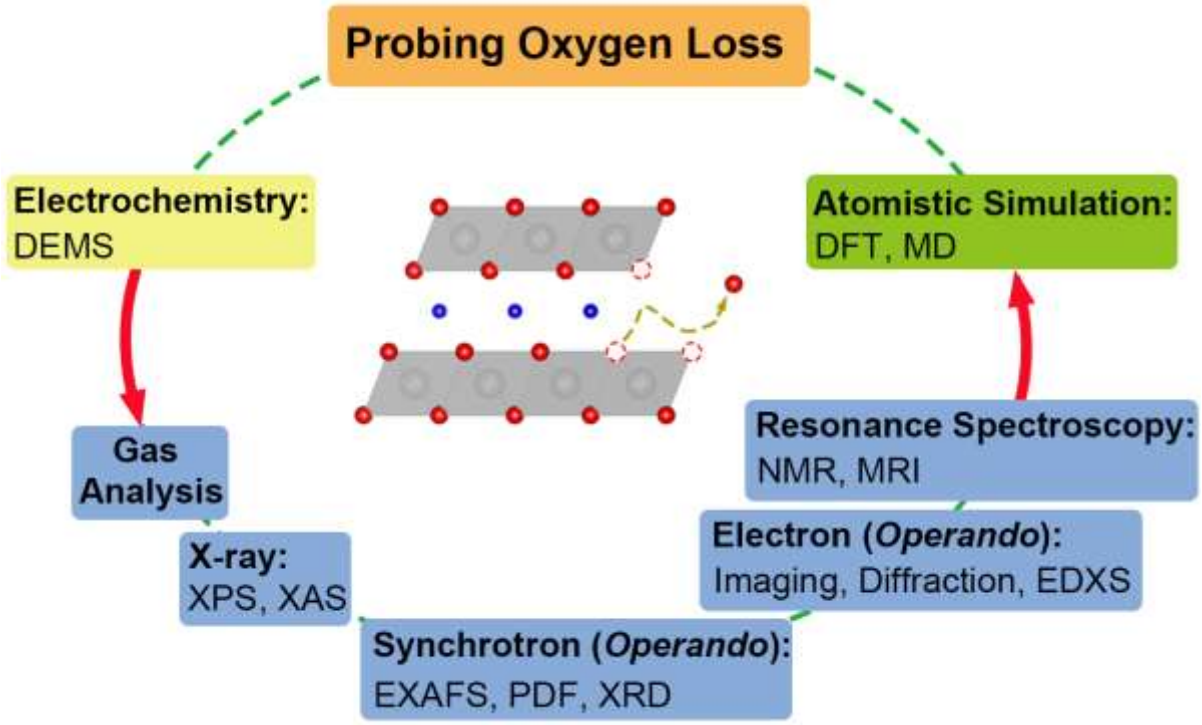

Figure 1 | State-of-the-art approaches towards probing the oxygen loss kinetics and mechanisms in layered oxide cathodes.

The purpose of this review is to give a full account of the fundamental mechanisms of the oxygen loss phenomena in the layered oxides gained from the experimental and theoretical methods. The paper is organized as follows: first the driving forces leading to the loss of lattice oxygen are described, which is followed by the discussions on the more complicated aspects of the oxygen-loss induced structural degradations and the associated kinetic pathways. Afterwards, we discuss the detrimental effects of oxygen loss on the electrochemical performance, as well as the experimental strategies

developed to mitigate the oxygen loss. A perspective on the future research is also presented. The causal relationship between the aforementioned topics is schematically illustrated in Figure 2. During the electrochemical cycling, there exist various driving forces influencing the kinetics and pathways of oxygen loss. With the various pathways of oxygen loss, several different structural degradations develop, which in turn affect the electrochemical performance of the cathodes. Two practically important layered cathodes, namely the stoichiometric layered oxides ($LiMO_2$) and Li-rich compounds ($Li_{1+x}M_{1-x}O_2$), are used as examples to elaborate the oxygen loss mechanisms. Oxygen loss dynamics differ drastically among the large family of layered compounds, but here we focus on the fundamental mechanisms governing the oxygen loss other than the specific differences among the various layered oxides. For more detailed information regarding the crystal structures, chemical composition and electrochemical performance among different layered oxides, the reader is referred to the review articles by Whittingham[7], Goodenough et al.[97], Myung et al.[6], Xu et al.[98] and Hy et al.[99] The readers are also referred to the recent reviews by Sharifi-Asl et al.[58] for a detailed summary of different structural degradation patterns, by Hausbrand et al.[22] for the degradation mechanisms of layered oxides, and by Chakraborty et al.[100] for the computational design and correlative electrochemistry of layered oxides.

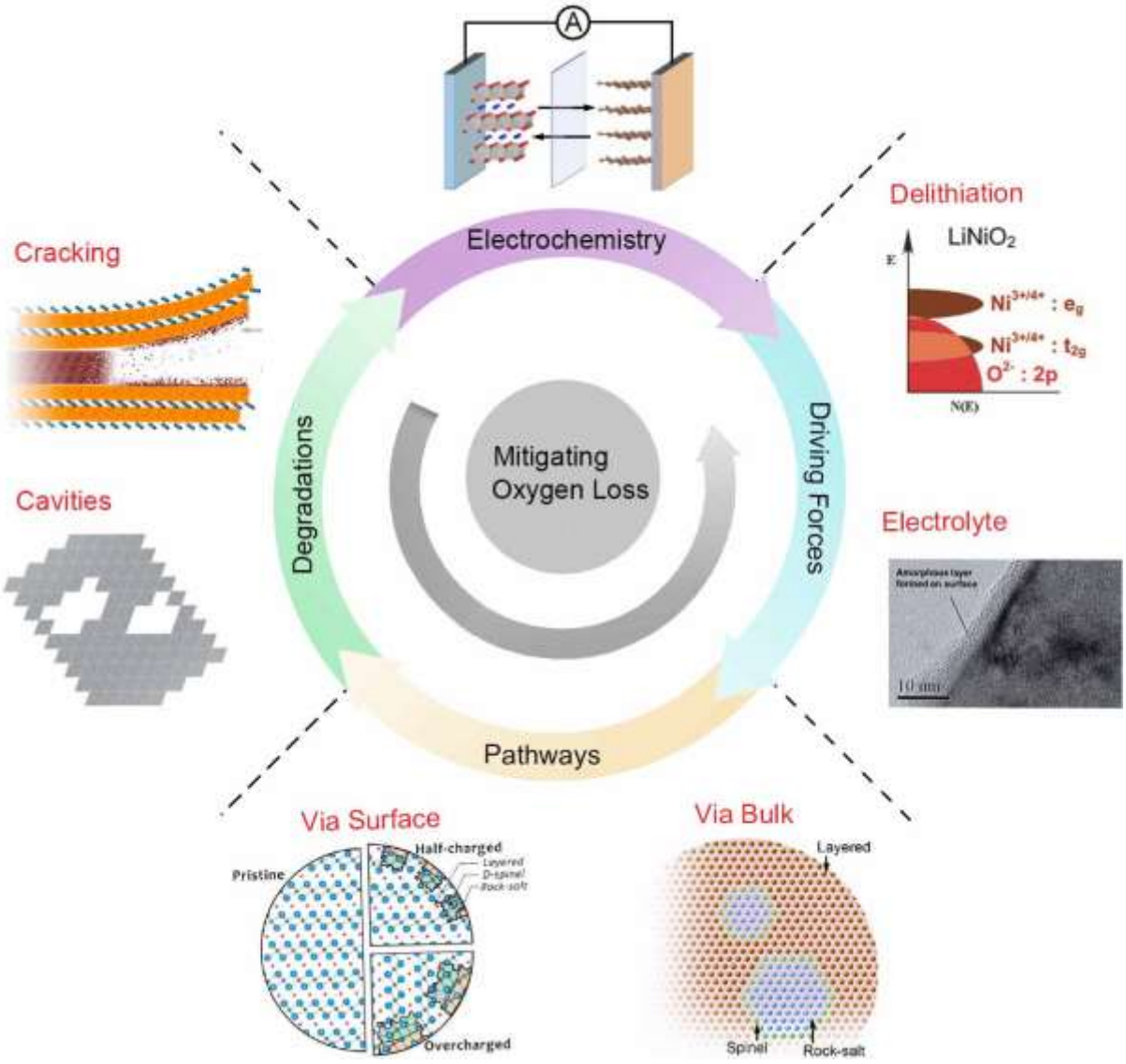

Figure 2 | Causality between the driving forces, kinetic pathways, structural degradations, and fade in the electrochemical performance associated with the oxygen loss. Examples of each topic are illustrated. 1) Delithiation: adapted with permission from ref [101].Copyright 2008 Royal Society of Chemistry. 2) Electrolyte: adapted with permission from ref [50]. Copyright 2012 American Chemical Society; 3) Surface: adapted with permission from ref [48]. Copyright 2014 American Chemical Society; 4) Bulk: adapted with permission from ref [102]. Copyright 2017 American Chemical Society; 5) Cracking: adapted with permission from ref [103]. Copyright 2017, American Chemical Society.

Besides the structural degradations of the layered cathodes induced by lattice oxygen loss, another important aspect of research is to understand the evolution of off-lattice

oxygen after escaping from the cathode. Some experiments have shown that the escaped singlet oxygen can oxidize the electrolyte and result in its decomposition,[50,104] which can potentially trigger rollover effects,[105] such as thermal runaway of the battery cell and even explosion.[58,106,107] Also, some off-lattice oxygen accumulates in the sealed cell in the form of gaseous O_2, which increases the internal pressure and acts as another source of burning and explosion.[108–110] Besides the fire and explosion, the free O_2 is also suspected to react with the binder in the cathode, resulting in a reduced attachment between the current collector and the cathode,[111–113] as well as the macroscale cracking within the cathode.[114,115]

2. Driving the Oxygen Loss

2. 1 Delithiation

Delithiation upon the charging of batteries is believed to be a major factor driving the oxygen loss in layered cathodes.[116–119] Extraction of Li^+ from the crystal lattice results in the oxidation of the transition metal (TM) cations from the valence state of 3+ towards 4+,[38,61,67,120,121] which become more oxidative and easier to obtain electrons from the lattice oxygen (O^{2-}),[122–124] eventually resulting in the release of gaseous O_2 to the surrounding environment.[125,126] The net loss from the pristine oxide is a Li_xO compound.[127] Studies[128–130] indicate that the charging-induced oxygen loss exacerbates when cut-off voltages above 4.4 V are adopted, which equals to an extraction of over 65% lithium from the cathode.[131–133] By contrast, cycling the electrodes under 4.3 V (Li^+ extraction <60 %) usually results in reduced kinetics of oxygen loss.[134] A higher charging

voltage results in pronounced extraction of the Li^+ cations and a higher oxidation state of the TM cations, which thus accelerates the oxidation of lattice O^{2-} as well as the associated release of gaseous oxygen.[135] Figure 3(a)[38] shows mass spectrometry (MS) analysis of O_2 release upon the charging of a $Li[Ni_{0.2}Li_{0.2}Mn_{0.6}]O_2$ cathode, which explicitly confirms the critical role of the higher voltage in accelerating the oxygen loss from the cathode. When the charging voltage is below 4.5 V, only minimum oxygen loss occurs. As the voltage reaches 4.5 V, an evident peak of gaseous oxygen shows up. It is worth noticing that the chemical composition of the layered cathode also plays an important role in the charging-induced oxygen loss. For instance, NMC 811 (NMC = $LiNi_{0.8}Mn_{0.1}Co_{0.1}O_2$) and NCA ($NCA = LiNi_{0.80}Co_{0.15}Al_{0.05}O_2$) cathodes with their transition metals composed of 80% Ni exhibit enhanced oxygen participation via metal rehybridization and the associated lattice contraction.[136] Compared with the low-Ni cathodes, the same extent of delithiation can be achieved with a lower cutoff voltage in NMC 811 and NCA, meaning that these layered oxides undergo severe oxygen loss at the lower charging voltages. More discussion can be found in Table 2 of subsection 4.2.

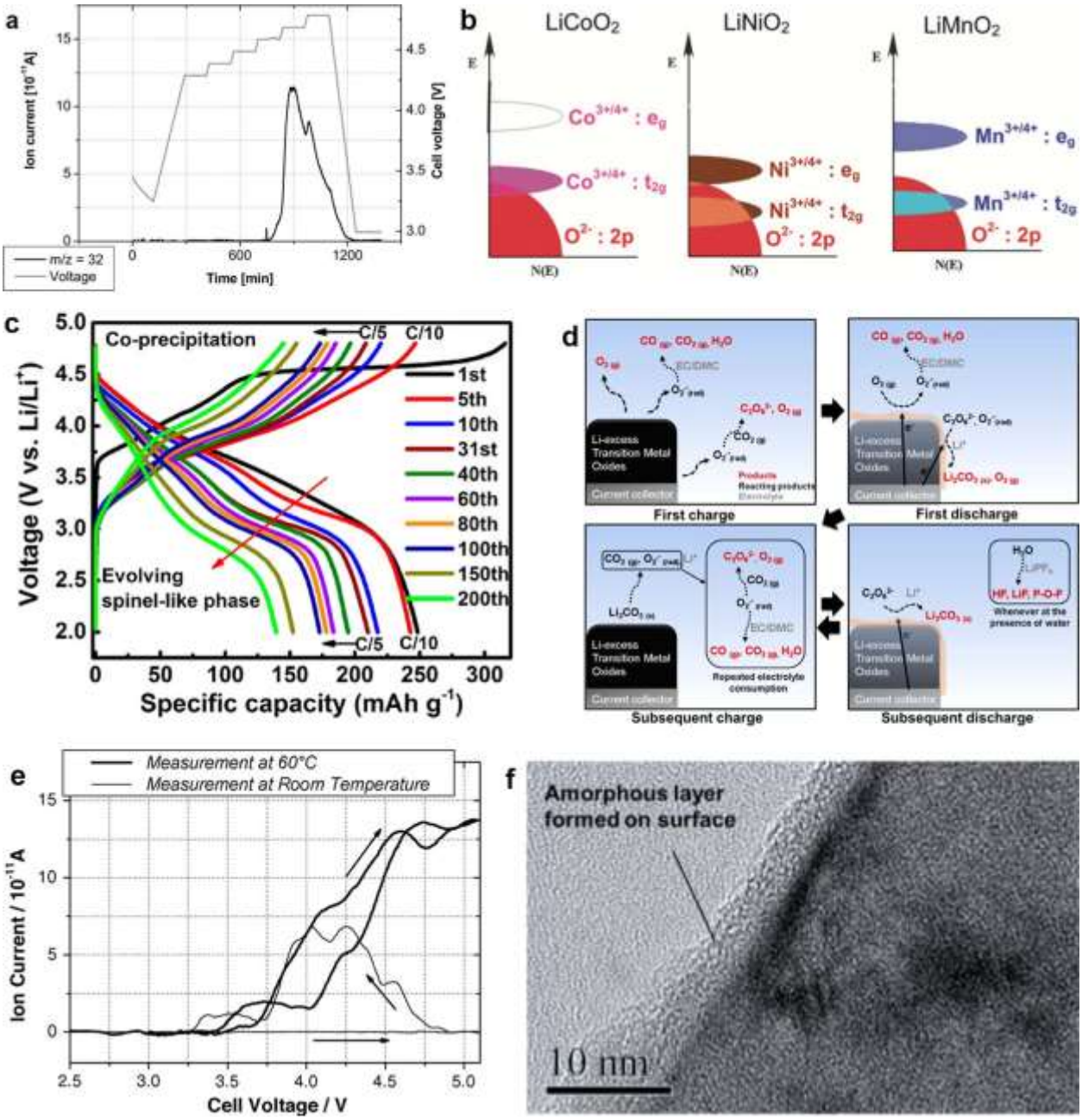

Figure 3 | Driving the oxygen loss in layered oxide cathodes. (a) Mass spectrometry observation of oxygen loss upon the charging of $Li[Ni_{0.2}Li_{0.2}Mn_{0.6}]O_2$. Reproduced with permission from ref [38]. Copyright 2006 American Chemical Society. (b) Comparing the electron shell energy diagrams of $Li_{1-x}CoO_2$, $Li_{1-x}NiO_2$ and $Li_{1-x}MnO_2$. Reproduced with permission from ref [101]. Copyright 2008 Royal Society of Chemistry. (c) First 21 galvanostatic charge/discharge cycles of LMR-NMC *vs.* Li in the 2.0-4.7 V range at 30°C, showing a 1st charge plateau associated with enhanced oxygen loss. Reproduced with permission from ref [137]. Copyright 2014 American Chemical Society. (d) Schematic summarizing the side reactions between the Li/O elements from the layered cathode and the electrolyte. Reproduced with permission from ref [50]. Copyright 2012 American Chemical Society. (e) CO_2 evolution in cells with a $Li(Ni,Co,Al)O_2$ cathode during the first cycle, operated at the room temperature and 60°C. Reproduced with permission from ref [138]. Copyright 2007 Elsevier. (f) HRTEM image showing the formation of an amorphous Li_2CO_3 + LiF mixture layer in the surface of an

electrochemically cycled particle. Reproduced with permission from ref [50]. Copyright 2012 American Chemical Society.

Qualitative electron shell energy diagrams of $Li_{1-x}CoO_2$, $Li_{1-x}NiO_2$ and $Li_{1-x}MnO_2$ are presented in Figure 3(b) and explain why the higher cut-off voltage accelerates the oxygen loss.[101,118] In the case of $LiCoO_2$ with a low spin Co^{3+}, the e_g band is completely empty while the t_{2g} band is completely filled. Upon delithiaton, electrons are removed from the t_{2g} band to induce the oxidation of Co^{3+}. As shown in Figure 3(b), the top of the O : 2p band overlaps with the bottom of the t_{2g} band. The initial delithiation removes electrons from the top of the t_{2g} band, and high-voltage delithiation removes electrons from the bottom, that is, the overlapped part of the t_{2g} band with the O : 2p band. In this case, electrons from the top of the O : 2p band is also removed, and oxidation of lattice O^{2-} occurs, thereby engendering the release of oxygen. By contrast, even the high cutoff voltage oxidation of the Ni^{3+} cations can only remove electrons from the e_g band that barely overlaps with the O : 2p band, and the same goes for the Mn^{3+} cation. By this means, Ni^{3+}/Ni^{4+} and Mn^{3+}/Mn^{4+} cations are more stable redox couples against the high-voltage-induced oxygen loss, although there are other factors making them less stable in the layered oxides.[131,139]

Distinctively, a voltage plateau is present during the first charge of lithium-manganese rich (LMR) layered cathodes,[140,141] as demonstrated in Figure 3(c).[137] The ~4.5 V plateau is attributed to intensive oxygen loss and the associated structural degradations (e.g., phase transformation), which is termed as “cathode activation”.[127,142] The absence of this plateau in the following electrochemical cycles corresponds to attenuated oxygen loss. This voltage plateau does not show up in the layered cathodes

other than LMR, majorly because they do not have such pronounced oxygen loss in the first cycle. Even though, oxygen loss in the oxides other than LMR is still pronounced in the first tens of cycles,[91,103] after which the fresh particle surface is stabilized by reaction with the electrolyte, and the oxygen loss slows down. In these cases, other evidence can be collected to monitor the cycling-induced subtle oxygen loss, which will be discussed later in this review.

2.2 Side Reactions (Electrolyte)

The lithium and oxygen from the cathode can react with the surrounding electrolyte and result in the formation of multiple compounds, which are collectively termed as “side reactions” of the electrochemical cycling.[119,143,144] The side reactions consume Li and O from the cathode as reactants, thus driving the loss of Li and O.[145,146] The participation of electrolyte in the side reactions leads to its partial decomposition.[4,147,148] Byproduct compounds are generated on the surface of the cathode particle or within the electrolyte. Figure 3(d)[50] summarizes some byproducts of the side reactions, including CO_2, H_2O, Li_2O, Li_2CO_3, LiF and multiple organic compounds. Regardless of the large number of the byproducts, here we only discuss a few major ones that pertain to the O/Li loss.

A key step in oxygen-loss-involved side reactions is the reduction of O_2. The gaseous O_2 from the cathode is highly oxidative and can be easily reduced by the electrolyte,[145,149–151] which is the major reason for the decomposition of the electrolyte. The reduction of O_2 results in the formation of free oxygen radicals (majorly O^{2-}) in the electrolyte,[152,153] which can subsequently combine with other components in the

electrolyte and results in the formation of the multiple byproducts. It is worth mentioning that the state of delithiation of layered oxides plays a factor in forming the reactive singlet O_2, while the stability of the electrolytes also determines their decomposition, meaning that the cathode/electrolyte reactions are complex processes. The readers are referred to the work by Strehle et al.[86] for detailed discussions.

The reduction of gaseous O_2 by the carbon black and the carbon species in the organic electrolyte results in the formation of CO_2.[38,154–156] Figure 3(e)[138] presents mass spectrometry showing the formation of CO_2 in an NCA cathode during the first charge, indicating that both a higher voltage and a higher temperature accelerate the production of CO_2 and thus the loss of oxygen, which confirms the driving effects of the higher cutoff voltages on accelerating the oxygen loss, as discussed in Figure 3(a).

Another side reaction is the formation of Li_2O via combining Li^+ from the cathode with O^{2-}.[157,158] As mentioned in section 2.1, the oxygen loss is accelerated by delithiation, meaning that the removal of Li and O from the cathode can be a synchronously coupled process, making the Li_2O a popular byproduct. Even without the electrochemical delithiation, the $2Li^+ + O^{2-} = Li_2O$ reaction chemically drives the outward diffusion of both Li and O from the cathode.[79,159] The electrochemically compatible Li_2O can further react with the acidic components from the electrolyte and transforms to less electrochemically active phases, such as LiF:[160]

$$LiPF_6 + H_2O + Li_2O \rightarrow 2HF + LiF\downarrow + 3Li_xPOF_y \quad (1)^{143}$$

Also, Li_2O can react with HF from the electrolyte or binder to form LiF.[161] LiF is usually imbedded in the solid-electrolyte interface (SEI) layer.

The gaseous CO_2 from the side reaction can easily combine with the Li_2O in the surface of cathode particles, resulting in the formation of Li_2CO_3.[50,162] The lithium carbonate together with LiF can form an amorphous SEI layer coated on the particle surface (Figure 3(f))[50], which reduces the ionic conductivity of the cathode and undermine the connectivity between neighboring cathode particles.

Table 1 summarizes the electrochemical conditions under which the formation of Li_2O-like compounds and the associated Li_2CO_3/LiOH occurs. Regardless of the accelerating effect of the high cutoff voltage on its formation,[163] Li_2O has been observed across NMC, $LiCoO_2$ and LMR cathodes under varied electrochemical conditions, including simple immersion of the layered oxide in electrolyte without cycling. The maximum Li_2O is generated at the activation of the cathode, which is progressively transformed to Li_2CO_3, LiOH or LiF compounds as the electrochemical cycling proceeds.[163,164]

Table 1 | Electrochemical conditions for the formation of Li_2O-like compounds.

Reference	Cathode	Electrolyte	Voltage (V)	Current Rate	Cycles
Cherkashinin et al.[165]	$LiNi_{0.4}Mn_{0.4}Co_{0.2}O_2$; $LiCoO_2$	$LiPF_6$ + EC + DMC	2.7~4.1; 2.7~4.5	C/2	Uncycled; 30-cycles
Hy et al.[127]	Li_2MnO_3; $LiNi_{0.5}Mn_{0.5}O_2$; $Li_{1.2}Ni_{0.2}Mn_{0.6}O_2$	$LiPF_6$ + EC + DMC	2.0~4.8	C/10	1st and 2nd
Cho et al.[166]	$LiNi_{0.7}Mn_{0.3}O_2$	$LiPF_6$ + EC + DMC	3.0~4.3	50 mA/g	100

Yabuuchi et al.[167]	$Li_{1.2}Ni_{0.13}Co_{0.13}Mn_{0.54}O_2$	$LiPF_6$ + EC + DMC	2.0~4.8	C/20	1

2.3 Intrinsic Instability

A full development of the coupled O-Li loss results in complete decomposition of the layered oxide. This can be described with the following reaction by taking $LiCoO_2$ as the example,

$$LiCoO_2 \leftrightarrow Li_2O + CoO \quad (2)[168]$$

Reaction (2) is a reversible process. Thermodynamically, the formation of $LiCoO_2$ via the combination of Li_2O and CoO is energetically favorable at room temperature (RT).[169] However, this does not mean that the layered oxide is very stable during the electrochemical cycling and its decomposition is a trivial process. A major factor driving the decomposition of the layered oxides (e.g., $LiCoO_2$) is that the Li_2O product can be consumed by further reaction with the electrolyte, as discussed in Section 2.2, transforming Li_2O into compounds such as LiF and Li_2CO_3. The consumption of Li_2O continuously drives the forward proceeding of reaction (2), namely the decomposition of $LiCoO_2$. In the meantime, the CoO formed via reaction (2) accumulates on the cathode particle surface.[170]

For a better understanding of reaction (2), a calculated $LiCoO_2$/(Li_2O + CoO) phase diagram is presented in Figure 4(a).[169] As can be seen, both high temperature and low oxygen pressure accelerate the decomposition of $LiCoO_2$, indicating that these two

factors thermodynamically accelerate the loss of oxygen. Since elevated temperatures are present in the synthesis of layered oxides as well as during the operation of battery cells, it is important to understand the thermal stabilities of layered oxides, as will be discussed in the next section.

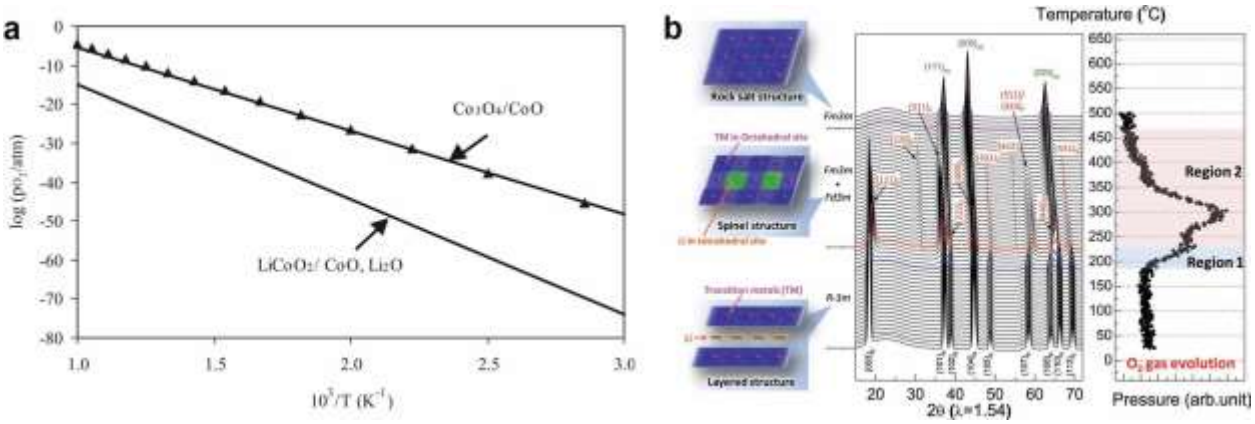

Figure 4 | Stabilities of layered oxides. (a) Calculated phase diagram of the Li-Co-O system. Reproduced with permission from ref [169]. Copyright 2004 Elsevier. (b) Coupled *in-situ* XRD and mass spectroscopy analysis of the heating-induced oxygen loss in $Li_{0.33}Ni_{0.80}Co_{0.15}Al_{0.05}O_2$. Reproduced with permission from ref [55]. Copyright 2013 Wiley-VCH.

2.4 Thermal Effects

As discussed in subsection 2.3, elevated temperatures accelerate the loss of Li and O, and thus the thermal decomposition of layered oxides, which is termed as “thermal instability” of the layered oxides. Studies of the thermal instability indicate that the thermally-induced structural degradations are very similar to the electrochemically induced ones,[8,171] which is a surprising conclusion considering that the impulses from these two treatments are intrinsically different. Clearly understanding the similarity and dissimilarity between the thermal and electrochemical instabilities will greatly enhance our understating of the structural stability of the layered cathodes.

Figure 4(b)[55] illustrates a coupled, temperature-resolved *in-situ* XRD and mass spectroscopy (MS) analysis of the thermal decomposition of $Li_{0.33}Ni_{0.80}Co_{0.15}Al_{0.05}O_2$ (NCA) from RT to 500ºC, which shows that heating above 200ºC induces significant oxygen loss from the cathode, transforming the oxygen-rich layered phase towards the oxygen-deficient rock-salt phase via an intermediate spinel phase. This trend is almost the same as the electrochemically induced oxygen loss, as demonstrated in Figure 5. The similarity between the thermally- and electrochemically-induced structural degradations is attributed to the fact that both impulses enhance the diffusion kinetics of oxygen and thus the oxygen loss, although the underlaying mechanism governing their similarity remains unresolved.[7] As the electrochemical cycling induces heat accumulation in battery cells, the accelerating effects of heating and electrochemical cycling on the oxygen loss promote each other, working as the major driving forces for the structural degradations in layered oxides.

3. Structural Degradations Induced by Oxygen Loss

Microstructural degradations are the direct results from the oxygen loss, and responsible for the degraded electrochemical performance of the cathode.[172–174] Due to the abundance of analytical methods for probing the structural degradations, they are extensively utilized in today's research for elucidating the oxygen loss kinetics and mechanisms. Intensive work has been performed in understanding the patterns of structural degradations as well as the mitigating methods. In this section, we will discuss

the structural degradations induced by oxygen loss and their generation pathways and mechanisms.

3. 1 Phase Transformations

Phase-transformation-associated structural degradations are frequently observed in both electrochemically-cycled and heat-treated layered oxide cathodes.[8,56,60,175–181] In a general description, the phase transformation in the layered cathodes follows a pathway of layered (*R*$\bar{3}$*m,* formula $LiMO_2$) → spinel (*Fd*$\bar{3}$*m,* formula LiM_2O_4) → rock-salt (*Fm*$\bar{3}$*m,* formula MO).[15,44,182–186] Due to its metastability, the spinel phase is usually considered as an intermediate status of the layered → rock-salt transformation.[187–189] The atomic configurations of these phases are schematically shown in Figures 5(a-c), and the corresponding scanning transmission electron microscopy high angle annular dark field (STEM-HAADF) images are presented in Figures 5(d-f).[28,69,179] An example of the phase transformation pathway is $LiNiO_2$ (layered) → $LiNi_2O_4$ (spinel) → NiO (rock-salt).[190]

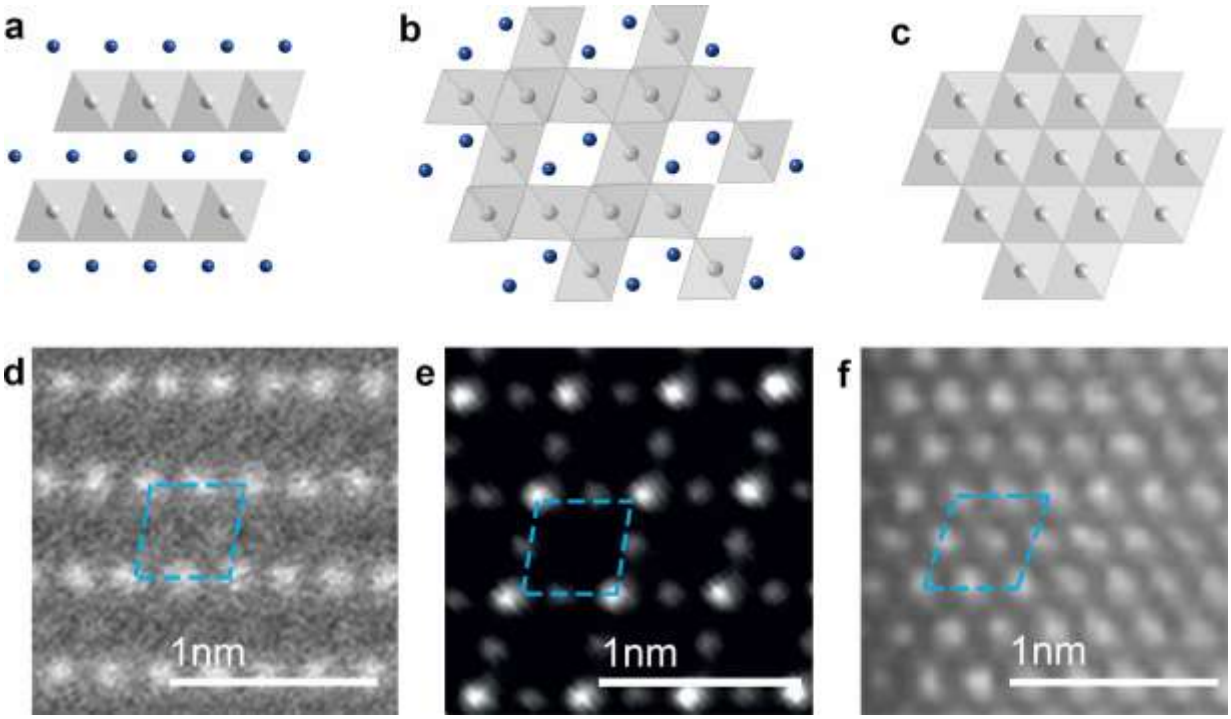

Figure 5 | Configurations of the layered, spinel and rock-salt phases. (a-c) Schematic atomic configurations of the layered, spinel and rock-salt phases. (d) STEM-HAADF observation of the layered phase. Adapted with permission from ref [69]. Copyright 2018 American Chemical Society. (e) STEM-HAADF observation of the spinel phase. Adapted with permission from ref [179]. Copyright 2015 Wiley-VCH. (f) STEM-HAADF observation of the rock-salt phase. Adapted with permission from ref [28]. Copyright 2013 American Chemical Society. The schematics in (a-c) were drawn using the VESTA crystallographic software.[191]

It is worth noticing that the layered and spinel phases have permeable lattice channels that allow for the diffusion and intercalation of lithium cations,[51,192–194] which are the structural foundation for their electrochemical properties. In contrast, the ideal rock-salt phase provides no lithium diffusion channels.[195] Therefore, the rock-salt phase is "electrochemically dead" because of its lack of the structural foundation for ion intercalation reaction.[62,196,197] However, electrochemically cycled electrode particles with a rock-salt surface layer do show electrochemical activity,[198,199] suggesting the presence of a percolating Li-channel network in the surface rock-salt phase. As opposed to the ideal rock-salt phase with only M^{2+} cations, a cation disordered/defective (e.g., TM

vacancies) rock-salt structure can allow for Li ion diffusion and even redox reaction. For example, the work by Ceder et al.[182,200,201] showed that the lithium excess disordered rock-salt cathode can exhibit a high capacity of > 280 mAh/g. The excess of lithium is necessary to open a percolating network of Li channels in the rock-salt structure, and thus promotes the insertion and extraction of Li^+. Elucidating the structural defects and Li-channel networks within the rock-salt phase is important to understand their effect on the functionality and degradation of the layered electrode.

Although the transformation from the layered to the spinel phase can be realized through the extraction of lithium without loss of lattice oxygen, *in situ* variable temperature studies of a partially delithiated layered cathode[55] have shown oxygen loss concurrent with the layered-to-spinel phase transition, suggesting the formation of oxygen vacancies in the spinel phase. A further loss of oxygen is usually considered necessary to complete the phase transition to the rock-salt phase.

Similarly, the layered → rock-salt phase transformation can take place via interlayer mixing between the TM and Li without involving changes in chemical composition. This fully randomizes the two kinds of cations and is termed as “cation disordering”.[41,139,182,190,202,203] However, a complete cation disordering without changing the chemical composition is not thermodynamically favorable,[204139] indicating a lack of driving force towards the cation-disorder rock-salt phase. A more favorable way leading to the rock-salt phase transformation is the formation of TM^{2+} cations accelerated by oxygen loss following the delithiation, as discussed in subsection 2.1. The readers are referred to the review by Mohanty et al.[205] for more discussions regarding the oxygen-loss induced phase transformations within layered oxides.

3.2 Oxygen Vacancies

The release of lattice oxygen leaves behind atomic vacancies in the oxygen framework.[206–209] The process of oxygen loss is initiated in the cathode surface where the oxygen vacancies are also generated and subsequently diffuses inwards.[89,210] As the atomic oxygen vacancies accumulate in the layered phase, the oxygen vacancies tend to aggregate to form extended structural defects, such as stacking faults, cavities and microcracks.

In-situ transmission electron microscopy (TEM) has been employed to monitor the oxygen-loss induced structural evolution in NCA upon heating at 400°C.[91] Results confirms the generation of oxygen vacancies in the surface region and the subsequent diffusion towards the core of the particle, as shown in Figures 6(a, b). The vacancy containing region in Figure 6(b) is highlighted with orange dashed lines. The inset of Figure 6(b) shows a magnified view of vacancy clusters, as marked with yellow arrows. The accumulation of oxygen vacancies in the particle results in their aggregation and coalescence (Figure 6(c) and the inset).

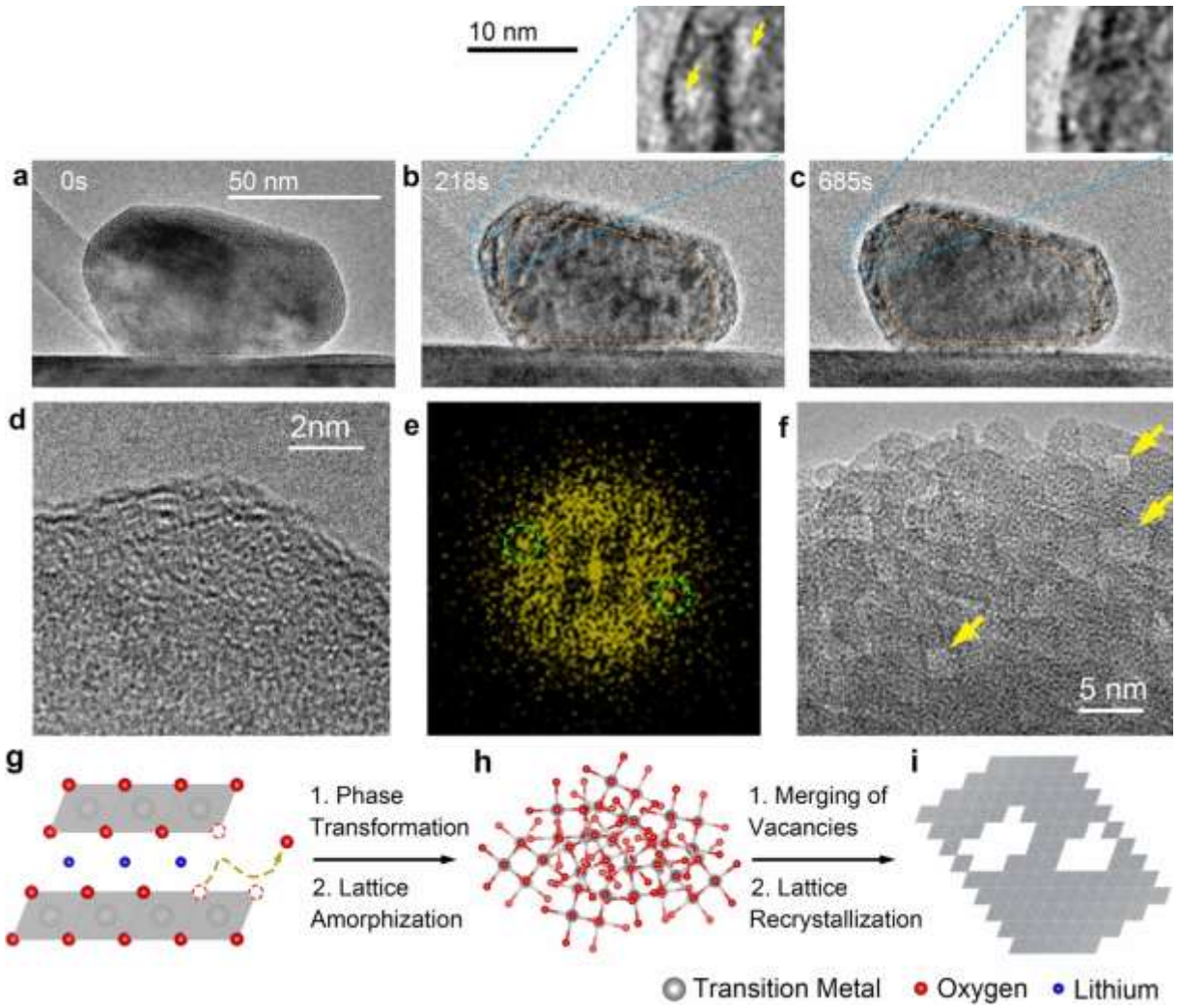

Figure 6 | Formation and evolution of oxygen vacancies. (a-c) *In-situ* observation of formation and inward diffusion of oxygen vacancies from the surface of an NCA particle kept at 400°C. The insets are magnified views from the surface area, showing the dynamic introduction and coalescence of oxygen vacancies. (d) Amorphized rock-salt phase from the accumulation of oxygen vacancies in the layered phase and (e) the corresponding diffractogram. (f) Recrystallization of the amorphized rock-salt phase and formation of cavities due to coalescence of oxygen vacancies. (g-i) Schematics showing the loss of lattice oxygen in the layered phase and formation of oxygen vacancies, formation of the amorphized rock-salt phase due to accumulation of oxygen vacancies in the layered phase, and recrystallization of the amorphized rock-salt phase and formation of cavities due to coalescence of oxygen vacancies, respectively. Adopted with permission from ref [91]. Copyright 2019 American Chemical Society.

During the oxygen loss, the population of oxygen vacancies transforms the layered phase towards the rock-salt phase.[183,211,212] In the meantime, the accumulation of oxygen vacancies also reduces the crystallinity of the crystal lattice. Their combined effects can

induce oartial amorphization in the resultant rock-salt phase, as shown in Figures 6(d, e). The amorphized rock-salt phase with a high concentration of oxygen vacancies exhibits a high formation energy,[55] thereby driving the coalesce of oxygen vacancies and the formation of cavities, as shown in Figure 6(f), marked with yellow arrows. At the same time, the amorphized rock-salt phase recrystallizes due to the reduced concentration of atomic oxygen vacancies. The kinetic pathway of the oxygen-loss-induced microstructure evolution in the layered cathode is schematically illustrated in Figures 6(g-i).

3.3 Mechanical Cracking

Two kinds of cracking are found in cycled layered electrodes: inter- and intra-granular cracking.[213,214] Cracking of cathodes has been widely recognized as a major cause in undermining the capacity, discharge voltage and service life of batteries[22,29,215–219] On the other hand, the driving forces and formation mechanisms of mechanical cracking have been only partially revealed so far. Multiple factors, including the intrinsic fragility of the layered oxides,[46] accumulation of minor structural defects[22] and the internal stress induced by electrochemical cycling,[29,103] are accused of being responsible for the mechanical cracking, while evaluating the importance and interplays of these factors is a major challenge.

Studies of electrochemically cycled cathodes[46,47] indicate that intra-granular cracking (cracking within the primary particle) of layered cathodes has three universal features: 1) cracking preferentially along the (003) atomic plane of the layered phase; 2) coexistence of the rock-salt-like phase with the layered phase, and 3) formation of cavities along the crack. Examples of these features are presented in Figures 7(a-d). Figures 7(a,

b)[220] present SEM and TEM images of cracks developed in electrochemically cycled $LiNi_{1/3}Mn_{1/3}Co_{1/3}O_2$ particles, which are parallel along the (003) plane. Figure 7(c)[103] presents the rock-salt phase along a developing crack. Figure 7(d)[221] presents an STEM-HAADF image of a developed crack, where cavities and the rock-salt phase are both observed along the crack face.

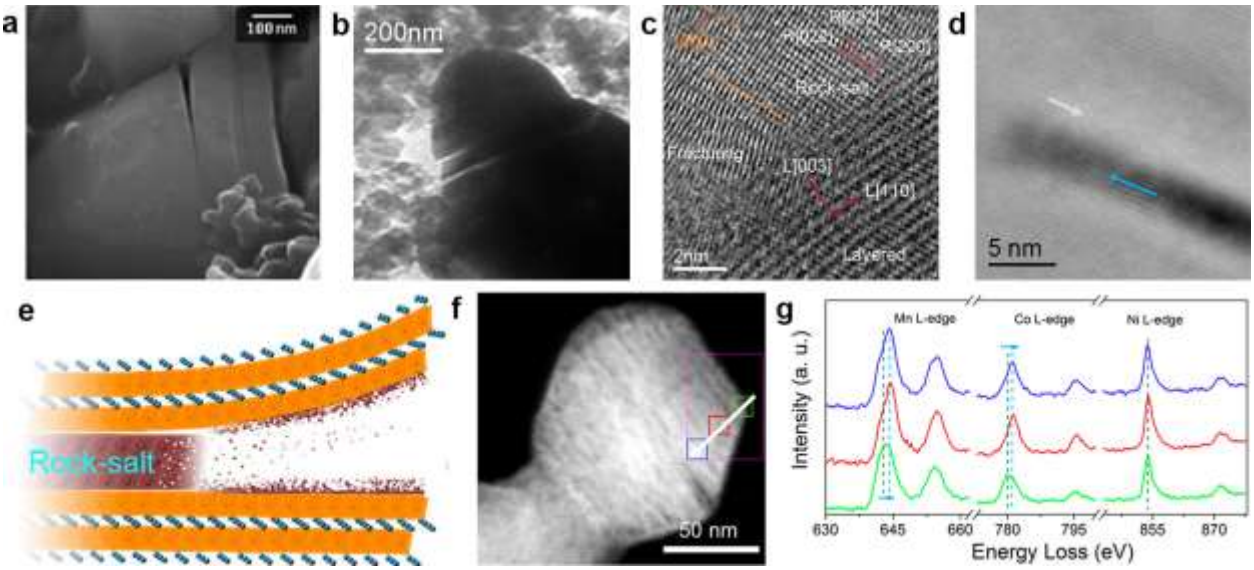

Figure 7 | Oxygen-loss-induced mechanical cracking. (a, b) SEM and TEM images showing development of intra-granular cracks along the (003) atomic plane. Reproduced with permission from ref [220]. Copyright 2013 Elsevier. (c) HRTEM observation showing presence of the rock-salt phase on a developing crack face. Reproduced with permission from ref [103]. Copyright 2017 American Chemical Society. (d) STEM-HAADF image showing the presence of microcavities and the rock-salt phase on a developed crack face, as marked out by the blue arrow. Adapted with permission from ref [221]. Copyright 2019 American Chemical Society. (e) Schematic showing the formation and fracturing of a rock-salt platelet across the particle, resulting in the (003) crack. Reproduced with permission from ref [103]. Copyright 2017 American Chemical Society. (f) STEM-HAADF image showing the formation of the (003) crack via coalescence of microcavities. (g) EELS spectra obtained from the surface towards the bulk of the particle in (f). Reproduced with permission from ref [222]. Copyright 2018 American Chemical Society.

Both the rock-salt phase and nanocavities result from the oxygen loss, as discussed in subsections 3.1 & 3.2. Therefore, the intra-granular cracking is also an oxygen-loss-induced phenomenon. The oxygen loss initiated from the particle surface progressively penetrates into the bulk, leaving behind a damaged lattice that finally turns into a crack.[222]

On the other hand, the kinetic pathway of oxygen-loss-induced cracking is still being highly debated and needs further research and validation. One hypothesis is the formation and fragmentation of a rock-salt platelet across the primary particle, as schematically shown in Figure 7(e).[103] Upon oxygen loss, a thin platelet of the rock-salt phase grows all the way through the primary particle. Due to its fragility, the rock-salt platelet is broken up by the stress shocks generated by the electrochemical cycling, leading to the formation of (003) cracks. The rock-salt platelet formation and growth by the oxygen loss is similar as the layered → rock-salt phase transformation discussed in section 3.1.

Lithiation/delithiation upon the electrochemical cycling results in the anisotropic lattice expansion and contraction of the layered phase. For instance, upon the delithiation from $LiNi_{1/3}Mn_{1/3}Co_{1/3}O_2$ to $Li_{0.5}Ni_{1/3}Mn_{1/3}Co_{1/3}O_2$, the lattice expands by 2.0% along the *c* direction and shrinks by 1.4% along the *a* direction.[223] On the other hand, the rock-salt phase generated via oxygen loss is electrochemically "dead", meaning that its lattice does not change along with the electrochemical cycling. The asynchronous expansion/contraction between the layered and rock-salt phases generates cyclic strain shocks on the brittle rock-salt phase, thereby resulting in its fracture and the associated particle cracking.[224,225] The readers are recommended to look up the works by Lim et al.[226], Ryu et al.[227], Li et al.[228] and Li et al.[229] for more details.

Another hypothetical pathway for the intra-granular cracking is the formation and coalescing of microcavities, as illustrated by the STEM-HAADF image in Figure 7(f).[222] A high concentration of cavities forms and subsequently coalesces along the (003) plane to generate a crack. EELS spectra of the particle (Figure 7(g)) indicate that the microcavities

have features of the rock-salt phase, as confirmed by the STEM-HAADF image in Figure 7(d). These cavities are surrounded by a shell of the rock-salt phase, which is further surrounded by a skin of the layered phase. It seems that the cavitation is a byproduct of the layered → rock-salt phase transformation, similar as the ones in Figures 6(f, i).

Apparently, more work needs to be performed to confirm the kinetic pathways and atomic mechanisms of cracking, which also helps understand the driving forces for oxygen loss from the surface *vs.* within the bulk. Based on the current observations, both the fracturing of rock-salt platelets and coalescing of cavities are the operating mechanisms for inducing the intra-granular cracking.

3.4 Surface Roughening

Upon the layered → rock-salt phase transformation, a shell of the rock-salt phase can be generated on the outermost surface of the particle due to the preferred oxygen loss in the surface.[230,231] The fragility of the rock-salt shell and cyclic electrochemical shocks induce surface fragmentation and roughening, similar as the fracturing of the rock-salt platelet in the bulk (Figure 7(e)). Figure 8(a)[232] shows the formation of an amorphous rock-salt layer in the surface of an electrochemically cycled $LiNi_{0.62}Co_{0.14}Mn_{0.24}O_2$ particle. The rock-salt shell has a loose, largely amorphized structure, making it vulnerable to electrochemical impulses and the associated cracking.[50] A crystallized rock-salt layer has a rigid, well-defined crystal lattice with a good structural integrity, but it still suffers from its intrinsic fragility (Figure 8(b))[69] and transforms into a hill-and-valley-like roughened surface configuration. The roughness increases the total surface area in contact with the

electrolyte, thereby accelerating the electrolyte-accelerated oxygen loss and structural degradations, such as the side reactions discussed in subsection 2.2.

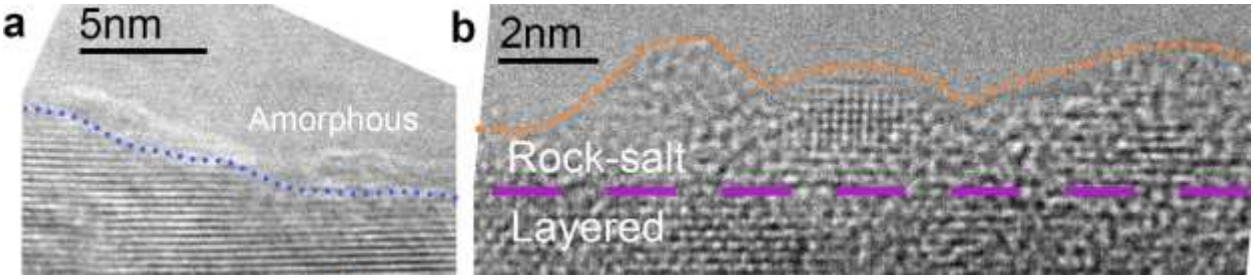

Figure 8 | Surface roughening. (a) STEM-HAADF image showing the formation and fracturing of an amorphous rock-salt shell in the surface. Adapted with permissions from ref [232]. Copyright 2021 Elsevier. (b) HRTEM image showing the formation and fracturing of the crystalline rock-salt phase in the surface, resulting in a hill-and-valley-like surface configuration. Reproduced with permission from ref [69]. Copyright 2018 American Chemical Society.

3.5 Interplays among Driving Forces and Structural Degradations

The development of the different structural defects follows the pathway from the generation of oxygen vacancies to spinel/rock-salt phase transformation and then to cracking/surface roughening (Figure 9(a)). The loss of lattice oxygen induces the reduction of TM cations and thus drives the phase transformation, and the generation of brittle rock-salt phases in the bulk and surface results in particle fracturing. The critical role of the rock-salt phase in the fracturing has been repeatedly shown in previous studies.[103,233,234] In other words, the meso- and macro-scale degradations and failures of the cathode particles are generated by the phase transformations induced by the accumulation of atomic defects. Examples of the developing pathway of structural degradations have been presented in Figures 7 and 8. It is also worth noticing that the degradation pathways shown in Figure 9(a) have been confirmed experimentally. As summarized in Table 2, the degradation pathways also depend on the cut-off voltage and number of cycles.

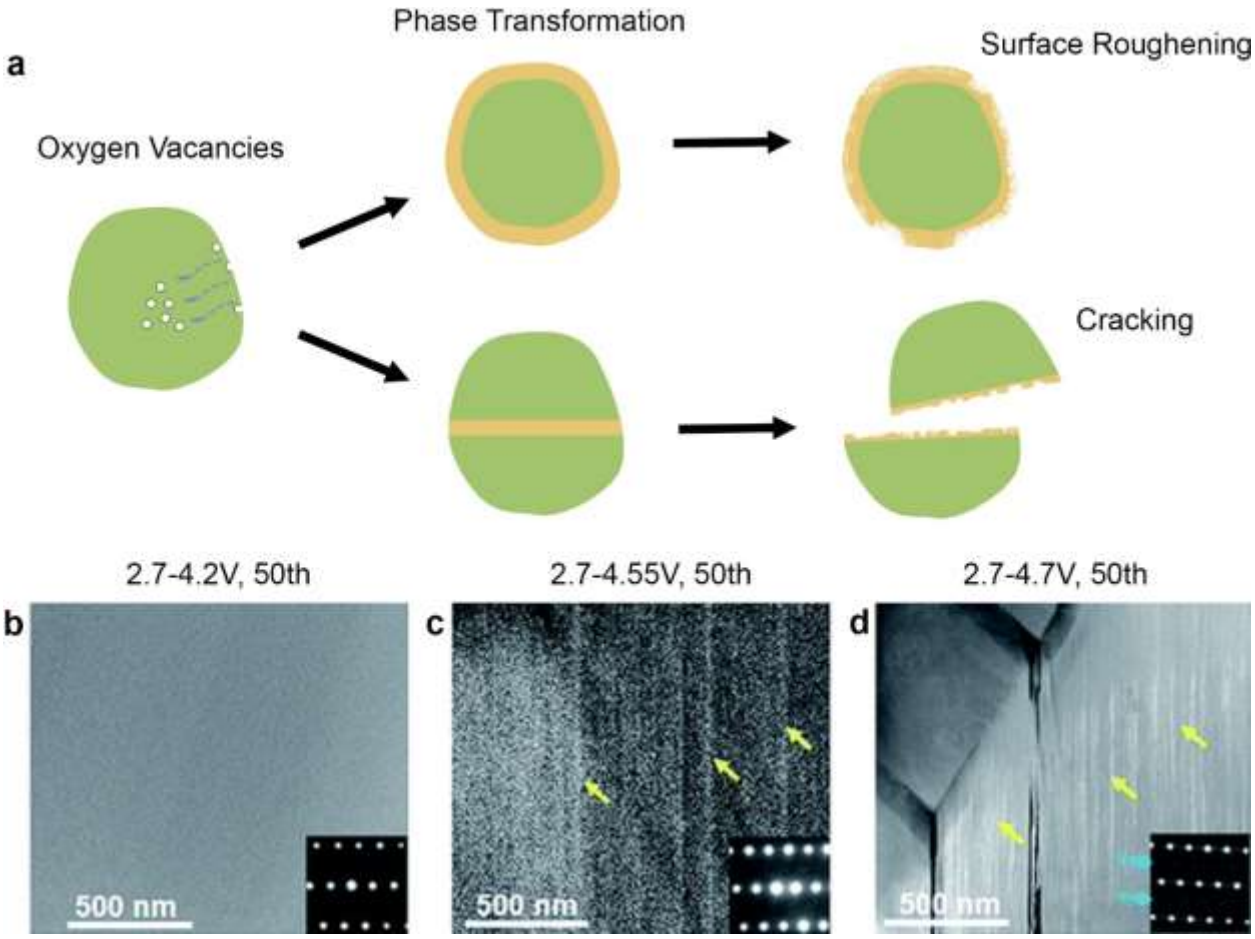

Figure 9 | Interplays among the driving forces and structural degradations. (a) Schematic showing the developing pathways of the structural degradations over multiple length scales ranging from the generation of atomic vacancies due to the loss of lattice oxygen to the spinel/rock-salt phase transformations and the resultant surface roughening and/or intragranular cracking. (b-d) Influence of the cutoff voltage on the development of intragranular cracking within $LiCoO_2$. Reproduced with permissions from ref [235]. Copyright 2019 Royal Society of Chemistry.

As discussed in Figure 3, a stronger driving force such as a higher cutoff voltage results in accelerated oxygen loss, generating more severe structural degradations and electrochemical fade.[105] This is exemplified by the $LiCoO_2$ in Figures 9(b-d),[235] which also confirms the degradation pathways shown in Figure 9(a). The cutoff voltage of 4.2 V generates no observable structural degradation (Figure 9(b)) after 50 electrochemical cycles. The 4.55 V generates plates of degraded phase (Figure 9(c)), while the 4.7 V

cutoff voltage further breaks the plates into cracks (Figure 9(d)), demonstrating the accelerating effect of the cutoff voltage on the development of cracking.

Compared with the extensive studies regarding the influence of cutoff voltage and thermal effects on the structural degradations,[236,237] there is still a great lack of understanding of the influence of the charge current rate, the type of electrolyte and the morphology of cathode particles on the microstructural evolution, although they are also known to influence the oxygen loss kinetics and the associated structural degradations.[238–241] A complete, comprehensive understanding of the various driving factors in the oxygen loss and resultant structural degradation will enhance our abilities in optimizing the electrochemical performance while maintaining desirable structural and electrochemical stability.

4. Pathways and Kinetics of Oxygen Loss

4.1 Surface- and Bulk-Related Oxygen Loss

Observing the pathways for oxygen loss is critically important for understanding the associated structural degradation mechanism and predicting the microstructural evolution in the cathode, yet little advances have been made in this field. The major challenge is the experimental difficulty in direct, *in-situ* observations of the oxygen loss process with a sufficient spatial and time resolution, which will be further elaborated in the Section 6. Instead, approaches of indirect or *ex-situ* observations have been made. Based on the observations, two pathways of oxygen loss have been proposed. The first one is the preferred loss of oxygen from the surface region, which progressively develops towards the particle core.[48,79,207,242–244] This hypothetical pathway was proposed based on the fact

that the surface is in direct contact with the electrolyte, as schematically shown in Figure 10(a)[139], which preferably drives oxygen loss from the surface other than the bulk. Side reactions, for example, majorly occur on the solid-electrolyte interface (SEI).[18,50,119,143] Oxygen and lithium atoms in the surface region travel a shorter distance to participate in the side reactions with the electrolyte. The preferable structural degradations in the surface region are widely observed, responsible for most of the structural degradations induced by oxygen loss.

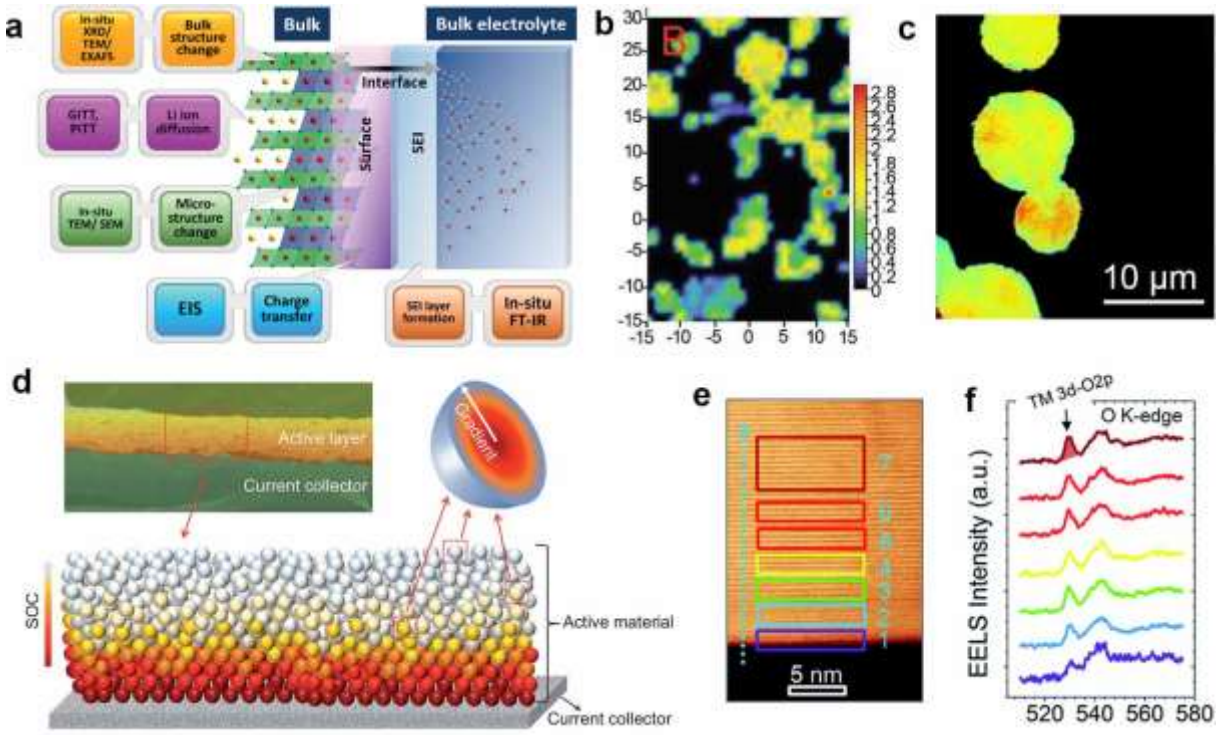

Figure 10 | Surface- and bulk-related pathways for oxygen loss. (a) Schematic illustrating the preferred oxygen loss in the surface induced by its direct contact with the electrolyte. Reproduced with permission from ref [139]. Copyright 2015 Wiley-VCH. (b) SOC map of NCA particles charged to 4.2 V, showing a uniform distribution of SOC. Reproduced with permission from ref [245]. Copyright 2011 Wiley-VCH. (c) SOC map of NMC-622 particles charged to 3.88 V, showing a uniform distribution of SOC. Reproduced with permission from ref [246]. Copyright 2018 Elsevier. (d) Schematic showing pronounced SOC in the particle surface upon charging. (e, f) EELS analysis showing a depth-dependent oxygen loss in an NMC particle charged to 4.7 V, induced by the combined effects of delithiation and electrolyte. Reproduced with permission from ref [66]. Copyright 2014 Royal Society of Chemistry.

Besides the electrolyte, delithiation is another major driving force for the oxygen loss, as we have discussed in subsection 2.1. The state of charge (SOC) of the cathode affects the valence state of the TM cations, thereby determining the oxidation of O^{2-} as well as the loss of oxygen. Figure 10(b)[245] presents an SOC map of NCA particles charged to 4.2 V, derived from the corresponding Raman map. The SOC distributes uniformly across the particle, and the surface region does not show observably higher SOC. Figure 10(c)[246] presents an SOC map of NMC-622 particles charged to 3.88 V, which is also uniform without lifted SOC in the surface. The uniform distribution of SOC indicates that delithiation drives oxygen loss from both the bulk and surface of the particles. In short, the accelerating effect of the electrolyte on oxygen loss is most pronounced in the surface, while the delithiation acts more uniformly in driving oxygen loss across the entire particle. With the combined effects of electrolyte and delithiation, the oxygen loss and the associated structural degradations are mostly pronounced in the particle surface while they are also possible in the bulk.

In contrast, the work by Lim et al. [247] shows that delithiation firstly occurs in the particle surface, as followed by delithiation in the bulk. This indicates that a higher SOC is generated in the surface, as schematically shown in Figure 10(d).[66] This argument is supported by the fact that the width of the lithium channels only allows for one Li^+ to pass. Considering a single Li^+ channel, the Li^+ cations in the surface have to leave first before the outward diffusion of deeper Li^+ cations can occur, meaning that delithiation is more feasible in the surface. This argument does not conflict with the uniform SOC maps shown in Figures 10(b, c). The SOC maps were obtained *ex situ* in charged particles where the Li concentration has reached equilibrium. The higher SOC in the surface is a kinetic effect

that occurs during the delithiation process. Once the driving force (i.e. current/voltage) for delithiation reaches a steady value (e.g., the cutoff voltage), the kinetically induced Li concentration gradient is eliminated during relaxation, resulting in a homogeneous SOC at equilibrium. Unfortunately, this kinetic process of delithiation has not been directly observed yet. The major challenge is the lack of measuring the extraction of Li cations at the nanometer and atomic levels. Direct observations will greatly enhance our understanding of the delithiation process. Another interesting question to be answered is how to differentiate the driving effects of delithiation and electrolyte on oxygen loss and the associated structural degradations. For now, we know that both the electrolyte and delithiation can lead to oxygen loss in the surface, but are unclear which one is more dominant and how these two mechanisms are coupled. Answers to these questions are critical in correlating the macroscale electrochemical performance with the cycling-induced oxygen loss at the atomic level.

A well-known example of the coupled effects of delithiation and electrolyte on driving the oxygen loss is the depth-dependent gradient of structural degradations developed from the surface towards the bulk, observed in electrochemically cycled cathodes.[48,79,177,248] Figures 10(e, f)[66] present an NMC particle charged to 4.7 V in an electrolyte composed of $LiPF_6$, EC and DMC, where depth-dependent EELS spectra were obtained. The pre-peak of the oxygen K-edge decreases from the bulk towards the surface. Since the pre-peak arises from the hybridization between the TM 3d shell and the O 2p shell, the EELS spectra in Figure 10(f) indicate that the loss of oxygen is most pronounced in the surface and is progressively attenuated towards the bulk, which results

from the influence of the electrolyte. On the other hand, the penetration of the oxygen loss to a depth of ~5 nm results from the influence of delithiation in the bulk.

Another piece of convincing evidence for the surface- and bulk-related oxygen loss pathways is that the layered → rock-salt phase transformation has been observed in both the surface and bulk of primary particles. Since the formation of the rock-salt phase is directly related to oxygen loss in the layered oxides,[38,67,178] the amount of the rock-salt phase generated in the layered oxide particle can be considered as an indicator for the oxygen loss. The surface region, which is in direct contact with the electrolyte, is preferred in oxygen loss and thus the phase transformation,[36,249–251] resulting in a so-called "core-shell" configuration in electrochemically degraded primary particles,[48,244] as shown in the high-resolution TEM (HRTEM) image in Figure 11(a)[177] and the corresponding schematic in Figure 11(b).[48] The bulk of the particle remains as the pristine layered phase.

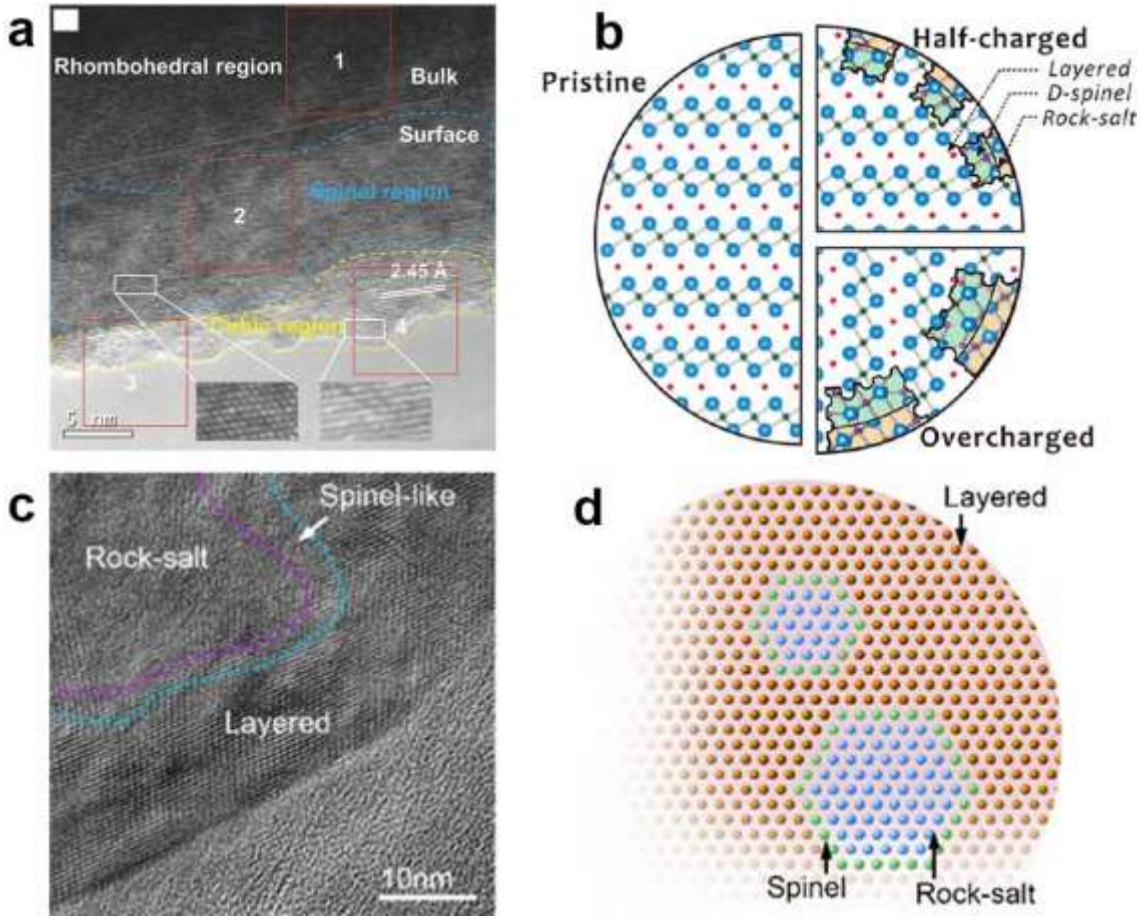

Figure 11 | Evidence of surface- and bulk-related oxygen loss pathways. (a) HRTEM image showing a "core-shell" configuration resulting from oxygen loss in the surface. Reproduced with permission from ref [177]. Copyright 2014 Wiley-VCH. (b) Schematic corresponding to (a). Reproduced with permission from ref [48]. Copyright 2014 American Chemical Society. (c, d) HRTEM image and schematic showing an "anti-core-shell" configuration formed by oxygen loss in the bulk of the particle. Reproduced with permission from ref [102]. Copyright 2017 American Chemical Society.

By contrast, oxygen loss from the bulk results in formation of the rock-salt phase in the core area. It has been observed that in $LiNi_{0.80}Co_{0.15}Al_{0.05}O_2$ (NCA) particles cycled between 3.0 - 4.3 V for 30 cycles, rock-salt domains of ~50 to ~70 nm are formed in the bulk of the particle, as demonstrated by the HRTEM image and schematic in Figures 11(c, d)[102]. This configuration is inversed compared with the core-shell configuration shown in Figures 11(a, b), so it is termed as an "anti-core-shell" configuration.

Bulk-related oxygen loss is kinetically slower compared with the surface-related loss. One reason is that the surface-related loss is driven by both electrolyte-assisted side reactions and delithiation, while the bulk related one is only driven by delithiation, as discussed in Figure 10. Also, oxygen in the bulk has to diffuse through the surrounding layered lattice to reach the surface, which is kinetically slow. For instance, the oxygen diffusivities in the lattice of $Li[Li_{1/9}Ni_{1/3}Mn_{5/9}]O_2$ at 30 and 50°C are 3×10^{-13} and 2×10^{-12} $cm^2 \cdot s^{-1}$, respectively.[252]

4.2 Oxygen Loss among Different Oxides

Due to the different chemical and structural conditions among the large family of layered oxides, different layered oxides exhibit distinctive features for the oxygen loss induced structural degradations. In Table 2 we present the structural degradation phenomena within the most common layered oxides: $LiCoO_2$, NMC, Ni-rich and LMR.

Table 2 | Structural Degradation Phenomena among Different Layered Oxides

Cathode	Degradation Pathway	Reference
$LiCoO_2$	2.5~4.35 V, 50 cycles: surface phase transformation and intragranular cracking	Wang et al.[185]
NMC 333	2.7~4.3/4.5 V, 100 cycles: surface phase transformation and internal cavities. 2.7~4.7/4.8 V, 100 cycles: cavities further develop into cracks	Yan et al.[237]
NMC 622	2.5~4.5 V, 50 cycles: surface phase transformation and microcracking	Yang et al.[253]
NMC 811	2.7~4.3 V, 100 cycles: surface phase transformation. 2.7~4.7 V, 100 cycles: surface phase transformation and intragranular cracking	Cheng et al.[254]
NCA	3.76~4.3 V, 100 cycles: surface phase transformation and microcracking	Park et al.[255]

$LiNiO_2$	3.3~4.2V, 100 cycles: surface phase transformation, nanopores and cracking	Yoon et al.[256]
$Li_{1.2}Ni_{0.2}Mn_{0.6}O_2$ (LMR)	2.0~4.7V, 45 cycles: surface phase transformation	Yan et al.[257]

Table 2 confirms the pathways of oxygen loss induced structural degradations in Figure 9(a), and cracking is considered as the most severe degradation. The Ni content and cutoff voltage are regarded as the major factors accelerating the oxygen loss, as demonstrated by the development of cracks in high-voltage or high-Ni tests.[237,258,259] The reader is recommended to read the review article by Li et al.[260] for a comprehensive comparison of the oxygen loss kinetics among different layered oxides.

As increasing the Ni content serves as a major approach for enhancing the capacity of NMC cathodes,[261,262] understanding the dependence of oxygen loss on the Ni content becomes a critical topic for maintaining the structural stability. Conventionally, Ni is considered to reduce the structurally stability, majorly because the high chemical and electrochemical activities of Ni facilitate the formation of minor structural defects such as Li-Ni anti sites and vacancies that subsequently lead to pronounced oxygen loss. The prevailing interlayer mixing between Ni^{3+} and Li^{+} also undermines the lithium intercalation and thus electrochemical kinetics.[263] Figures 12(a-c)[264] present differential capacity *vs.* voltage curves of $LiNi_{1/3}Co_{1/3}Mn_{1/3}O_2$, $LiNi_{0.6}Co_{0.2}Mn_{0.2}O_2$ and $LiNi_{0.8}Co_{0.1}Mn_{0.1}O_2$. As can be seen, higher Ni contents transform the original two-phase transition to multiphase transitions, which results in declined reversibility and cycling performance of the oxides owing to the lattice distortion and oxygen loss.

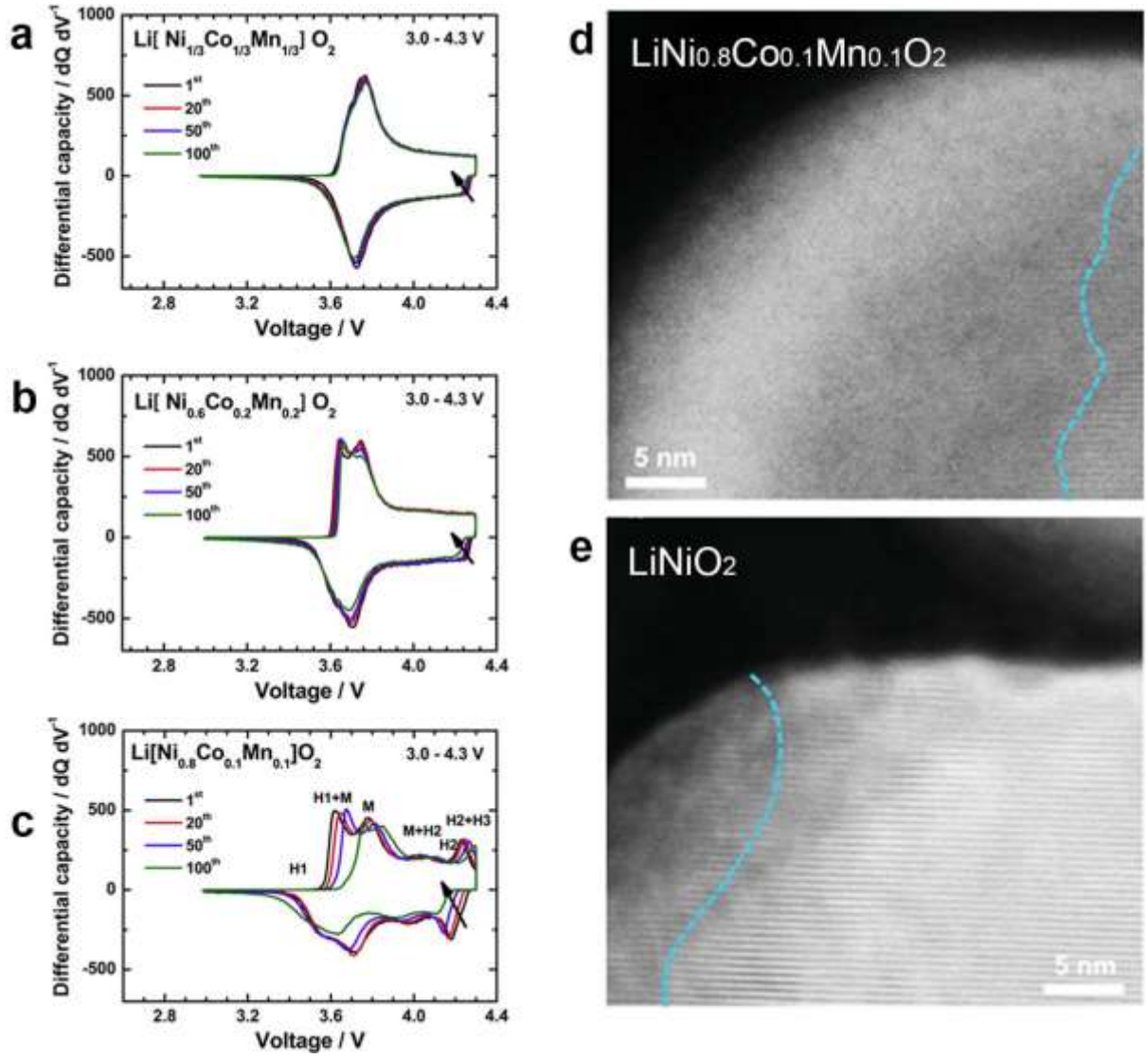

Figure 12 | Influence of Ni content on the oxygen-loss kinetics. (a-c) Differential capacity *vs.* voltage curves of $LiNi_{1/3}Co_{1/3}Mn_{1/3}O_2$, $LiNi_{0.6}Co_{0.2}Mn_{0.2}O_2$ and $LiNi_{0.8}Co_{0.1}Mn_{0.1}O_2$. The higher Ni contents result in pronounced multiphase transitions and structural degradations. Reproduced with permission from ref [264]. Copyright 2013 Elsevier. (d, e) STEM-HAADF observation of $LiNi_{0.8}Co_{0.1}Mn_{0.1}O_2$ and $LiNiO_2$ cathodes after 100 cycles, showing reduced oxygen loss with an increased Ni content. Reproduced with permission from ref [265]. Copyright 2021 Wiley-VCH.

Xie et al.[265] recently proposed that other than the Ni content, the SOC and surface reactions of high-Ni cathodes play bigger roles in the structural and electrochemical fade. In their comparison of 100-cycle $LiNi_{0.8}Co_{0.1}Mn_{0.1}O_2$ and $LiNiO_2$ cathodes, the former

shows more significant surface degradation (Figures 12 (d, e)). This work brings to attention that the cathode-electrolyte interaction and formation of SEI in the particle surface plays a critical role in promoting oxygen loss. The SEI was previously reported as a diffusion barrier that separates the cathode and the electrolyte and thus prevents further oxygen loss.[266,267] In contrast to the previous understanding, Xie et al. found that its non-self-limiting formation process requires continuous reaction with the lattice oxygen and therefore results in significant oxygen loss (see also subsection 2.2 “Side Reactions (Electrolyte)”). Acknowledging the complex role of Ni in the oxygen-loss-related structural degradation, more research effort is called on the complex multiphase transitions within high-Ni cathodes in Figures 12(a-c), which remains as a major source for the surface and bulk oxygen loss and crystal lattice deterioration.

4.3 Other Factors Affecting Oxygen Loss Kinetics

Besides the surface- and bulk-related pathways of oxygen loss, there are more kinetic factors in oxygen loss, such as the rate, the amount and the relationship between oxygen loss and cycling numbers, as discussed in the following. The rate of oxygen loss is negatively correlated to the cycling number. Research[268–270] shows that oxygen loss is most pronounced in the first tens of cycles, after which it gradually slows down and eventually becomes unobservable. In LMR materials, the first cycle has the most active oxygen loss, which is much attenuated in the following cycles, as shown in the example in Figure 13(a).[50] A $Li_{1.2}Ni_{0.2}Mn_{0.6}O_2$ cathode was cycled between 2.0-4.8 V at 10 mA/g, and differential electrochemical mass spectroscopy (DEMS) was recorded *in-situ*. The

most dominant oxygen loss during the first charge is confirmed with the detection of O_2, CO and CO_2.

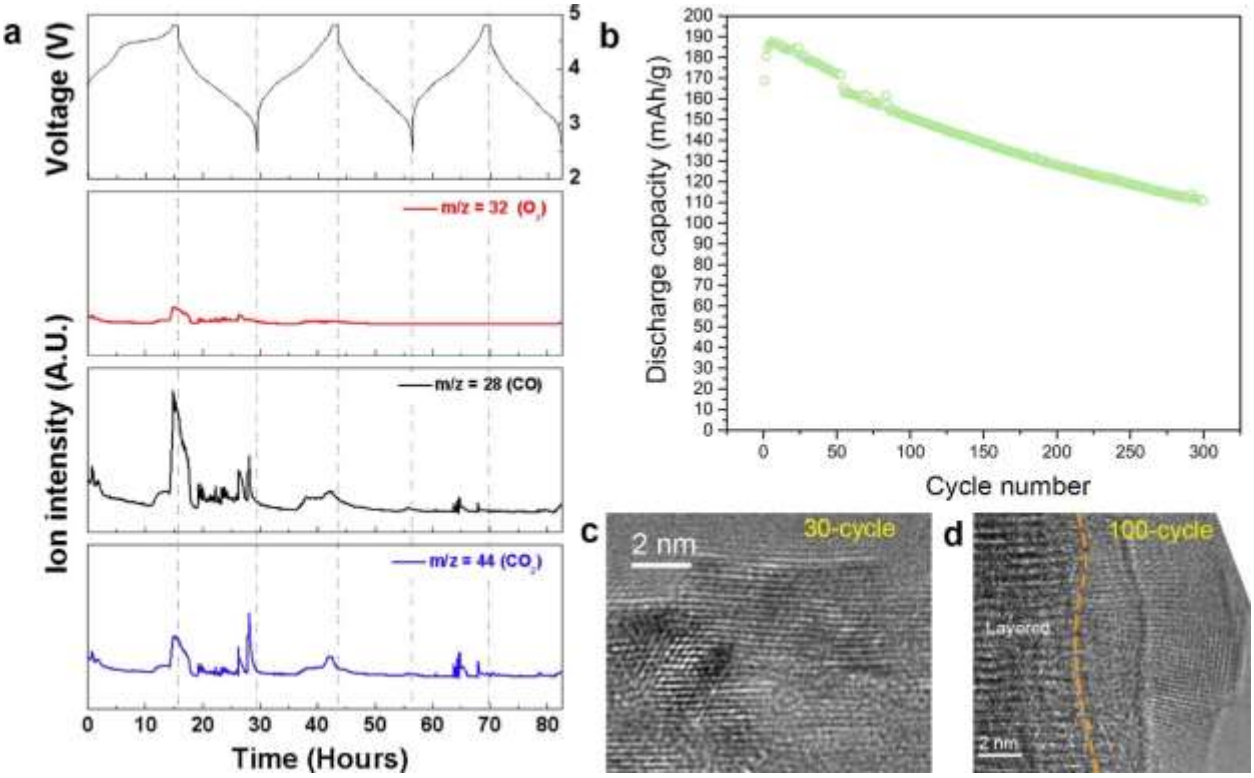

Figure 13 | Relationship between the rate of oxygen loss and cycle numbers. (a) DEMS analysis showing the loss of O_2, CO and CO_2 as a function of the electrochemical cycling of a $Li_{1.2}Ni_{0.2}Mn_{0.6}O_2$ cathode. Reproduced with permission from ref [50]. Copyright 2012 American Chemical Society. (b) Discharge capacity *vs.* cycle number curve of a TODA-NCA cathode, showing an abrupt reduction of capacity around the 50th cycle. (c) HRTEM image of a 30-cycle TODA-NCA particle, showing the formation of a partially crystallized surface rock-salt layer. (d) HRTEM image of a 100-cycle TODA-NCA particle, showing the formation of a fully crystallized surface rock-salt layer. Reproduced with permission from ref [91]. Copyright 2019 American Chemical Society.

In the stoichiometric layered cathodes, the loss of oxygen is pronounced in the first tens of cycles. Figure 13(b)[91] presents a discharge capacity *vs.* cycle number curve of a TODA-NCA cathode cycled between 3.0-4.3 V for 300 cycles, at a rate of C/10. Besides the gradual capacity loss as a function of cycling, an abrupt capacity loss shows up around the 50th cycle, which can be attributed to the formation of an amorphous surface rock-salt shell and its recrystallization (Figures 13(c, d)). Before the 50th cycle, an

amorphous rock-salt shell develops in the particle surface and undergoes gradual crystallization, as shown by the HRTEM image of a 30-cycle sample in Figure 13(c), where the rock-salt shell is partially crystallized. Around the 50th cycle, the surface rock-salt shell becomes fully crystallized, which isolates the intact layered phase in the core from the surrounding electrolyte, significantly reducing the ionic conductivity and resulting in the abrupt loss of capacity. An HRTEM view of the100-cycle particle (Figure 13(d)) confirms the presence of the fully crystallized surface rock-salt layer. In other words, the oxygen loss is most pronounced before the 50th cycle. Once the crystalline rock-salt shell forms around the 50th cycle, it slows down the outward diffusion of oxygen due to its low conductivity of oxygen.

Like all chemical reactions, oxygen loss stops when the reactant runs out. For the layered electrode, the reactant is the pristine $R\bar{3}m$ layered phase, whose amount is fixed in a battery cell. The final product after a full decomposition is the rock-salt phase, e.g., NiO, which is very stable in the battery cell and unlikely to go through further oxygen loss.[244] Therefore, oxygen loss stops once the layered phase is fully transformed to the rock-salt phase. However, in a realistic battery cell the layered phase is almost impossible to fully decompose even after a long operation time. For instance, $LiCoO_2$ and NCA cathodes cycled between 2.5 - 4.2 V at 45°C retain capacities of > 70% after 500 cycles.[233] Another example is that $LiCoO_2$/graphite cells tested between 3.0 - 4.2 V at 45°C also retain capacities of > 70% after 300 cycles.[271] Other than considering the theoretical status of a “fully damaged” battery cell, it is more realistic to consider the oxygen loss during a service time of 1000-5000 cycles or 3-5 years.

As demonstrated in Figures 13(c, d), a crystallized rock-salt shell forms in the particle surface after 50 cycles. The presence of this crystalline rock-salt layer isolates the layered phase in the bulk from the electrolyte surrounding the particle, significantly slowing down the loss of oxygen.[44,272,273] This configuration seems to be the "final product" of oxygen loss in a realistic layered oxide cathode, although cracking can break a large particle into a few smaller ones covered with the rock-salt phase. On the other hand, the capacity continues to fade after the formation of the crystalline surface rock-salt layer, and it is unknown if this fade is caused by the continued loss of oxygen, or other structural degradations such as lattice disordering and interlayer mixing between Li/TM cations. Therefore, monitoring the chemical and structural evolution in long-term-service battery cells is critically important, as demonstrated by the results of Xu,[224] Kleiner[274] and Liu,[45] while further relevant research is needed.

5. Oxygen Loss and the Correlative Electrochemical Performance

There is no doubt that all forms of the oxygen-loss-induced structural degradations have detrimental effects on the electrochemical performance of the layered cathodes. The real interesting questions are, (i) how those structural defects are generated by the electrochemical cycling, and (ii) how the structural defects in turn affect the electrochemical properties such as capacity, discharge voltage and rate capability. We have discussed the first question in the previous sections, and discuss the second one in this section. Like most materials, the structure-property relationship lies within the central interest of the research and application of layered oxides. Unfortunately, quantitative results on the structure-property relationship are still in a great lack.

5.1 Capacity

Capacity is one of the most important electrochemical properties of a cathode material. Since all the structural degradations consume the electrochemically active layered phase, the reduction in the mass and integrity of the layered phase leads to the declined capacity. As exemplified in Figures 14(a-c),[181] the capacity fade is positively correlated with the layered → rock-salt phase transformation in the cathode. After over 300 cycles, a $Li(Li_{0.19}Mn_{0.54}Ni_{0.13}Co_{0.12}Ru_{0.01})O_2$ layered cathode is observed to transform towards the rock-salt phase both structurally ($Fm\bar{3}m$ structure, Figure 14(a)) and chemically (reduction of TM cations from 3+ towards 2+, Figure 14(b)), which is accompanied by a gradual capacity fade (Figure 14(c)). In other words, the capacity loss is a function of the layered → rock-salt phase transformation.

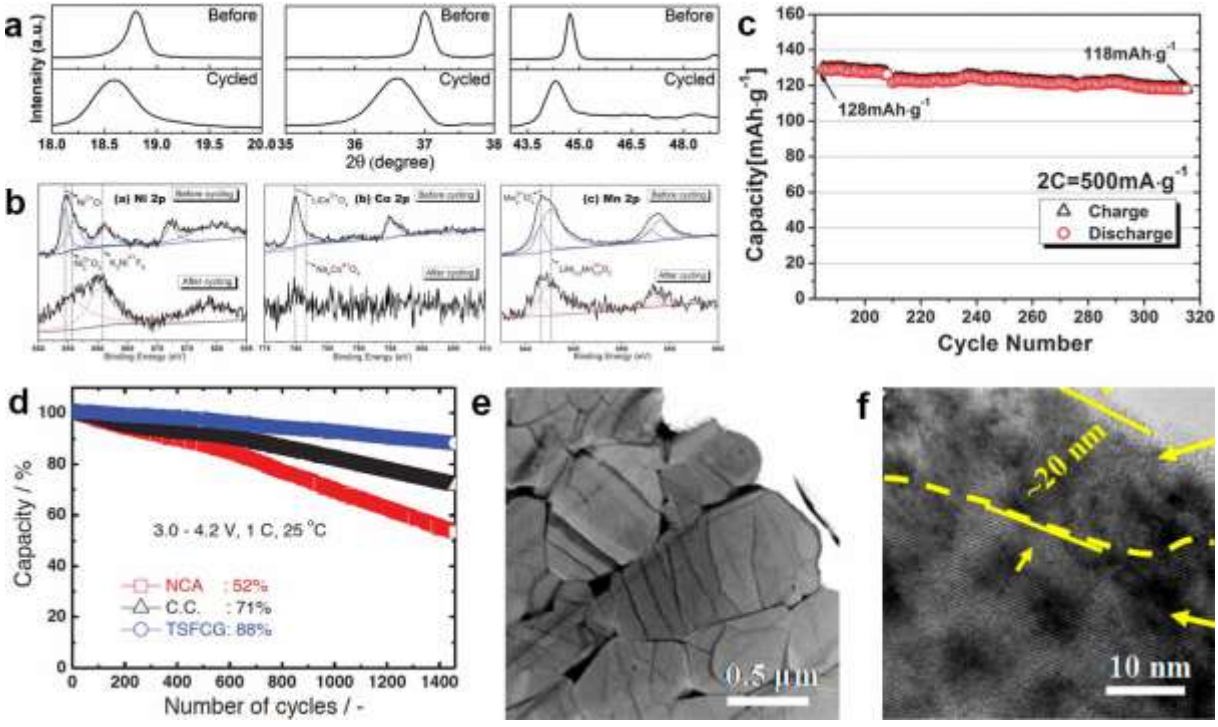

Figure 14 | Oxygen loss and capacity fade. (a) XRD analysis of structural transformation towards the rock-salt phase accompanying the oxygen loss. (b) XPS analysis showing the reduction of TM

cations accompanying the oxygen loss. (c) Capacity fade accompanying the electrochemical cycling induced oxygen loss. Reproduced with permission from ref [181]. Copyright 2012 Royal Society of Chemistry. (d) An NCA cathode showing capacity loss of 48% after 1400 cycles. Reproduced with permission from ref [275]. Copyright 2015 Wiley-VCH. (e) Full development of cracks that break down the whole secondary particle. (f) Severe phase transformation in the particle surface leading to the formation of a thick rock-salt shell. Reproduced with permission from ref [35]. Copyright 2018 American Chemical Society.

It is worth noticing that the kinetic pathways of the phase transformation, such as the growth morphology of the rock-salt phase, drastically determine the fade in the electrochemical performance. For example, formation of a surface shell of the rock-salt phase can slow down the intercalation kinetics of the layered phase underneath, thereby reducing the electrochemical performance of the whole cathode particle (Figures 11(a, b)). On the other hand, discontinuous rock-salt domains in the bulk of the layered particle do not have this blocking effect, thereby imposing much less influence on the electrochemical fade (Figures 11(c, d)). The kinetic pathways account for the loss of electrochemical performance that cannot be simply explained by the phase transformation. According to the data reported,[48,69,79,102,177] only less than 10% of the pristine layered phase is consumed after long-term electrochemical cycling (500 - 2000 cycles), while the capacity fade can be as much as ~50% due to the formation of the rock-salt shell, as illustrated by the red curve in Figure 14(d).[275] More discussion on the detrimental effects of the surface rock-salt shell is presented in Figures 13(b-d). Liu et al.[45] employed *in-situ* XRD to quantify the fraction of the crystalline layered phases of the TODA NCA electrode during the initial cycles and after a total of >90 cycles (at C/20 between 2.7 - 4.5 V). The mole fraction of the layered NCA decreases by 5% after the 1st cycle, presumably due to the surface reconstruction into the rock-salt phase, but remains almost unchanged during the subsequent >90 cycles while the discharge capacity

reduces by 20% from 203 to 163 mAh/g. This quantitative analysis suggests that the loss of the layered phase is prominent in the first-cycle electrochemical fade but contributes less to the subsequent capacity loss.

At the moment, the specific contribution from each type of the structural degradations to capacity loss remains largely elusive. This is majorly due to the coexistence and complex interplay of the various structural degradations. Different structural defects, including the surface rock-salt shell, cracks and cavities, can be generated in the same cathode particle.[276] As a consequence, it is difficult to single out the detrimental effect of an individual degradation. It seems that they can all heavily damage the cathode after a full evolution. For instance, a full development of cracking can penetrate both the primary and secondary particles and break them down, as shown in Figure 14(e).[35] Another example is that the severe phase transformation in the surface results in a thick rock-salt shell (Figure 14(f), ~20 nm),[35] which drastically reduces the electrochemical kinetics.

5.2 Other Electrochemical Fade

Discharge voltage is another critical electrochemical property of the cathode and affects the power density.[88,219,277] Once the discharge voltage of the cathode drops below the limit to drive the load, the battery cell is out of service regardless of its remaining capacity. An example of voltage fade is presented by the charge-discharge curves in Figure 15(a).[278] The voltage fade is caused by the reduced chemical potential of the cathode,[279] which is largely attributed to the reduced valence state of TM cations. As

discussed in the previous sections, the reduction of TM cations is directly related with oxygen loss, meaning that oxygen loss is a direct reason for the voltage fade.

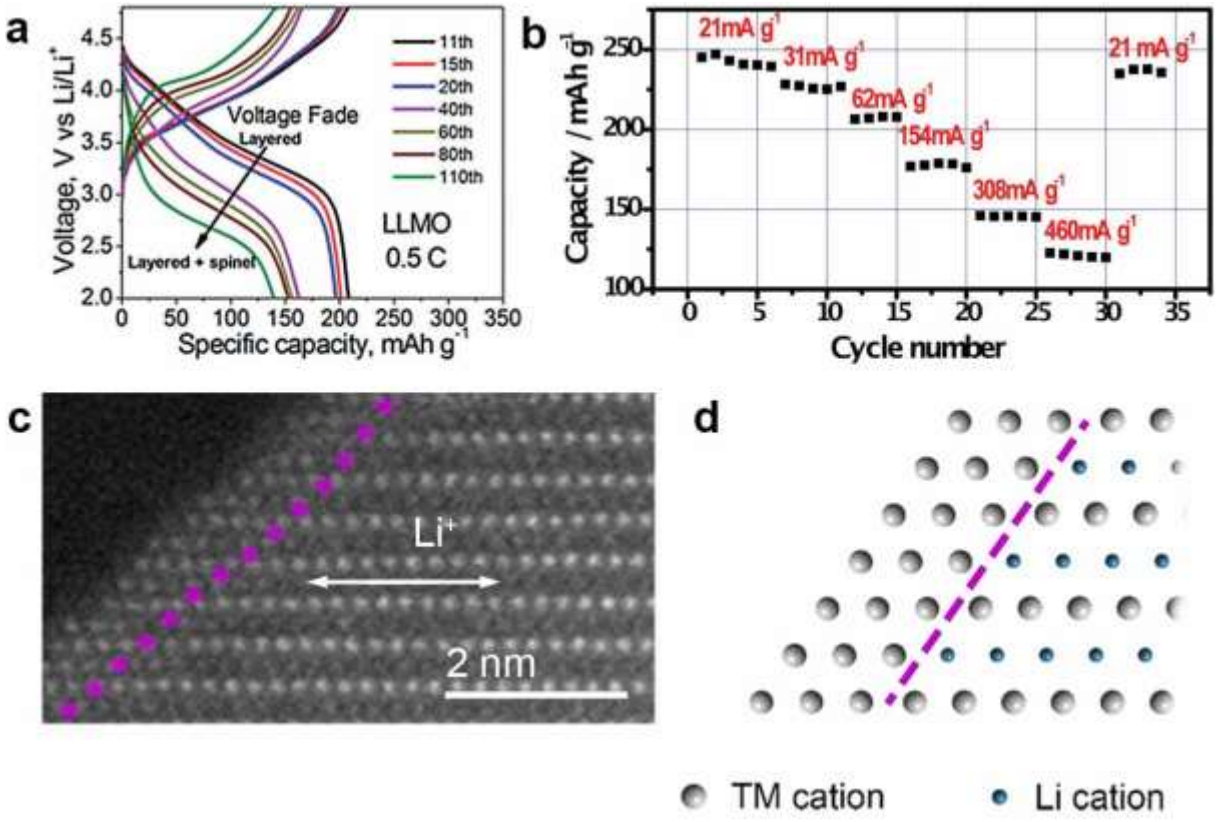

Figure 15 | Oxygen loss and voltage fade. (a) Charge-discharge curves of a $Li_{1.2}Mn_{0.54}Ni_{0.13}Co_{0.13}O_2$ cathode showing cycling-induced voltage fade. Reproduced with permission from ref [278]. Copyright 2015 Wiley-VCH. (b) Capacity *vs.* cycle number curve showing the effect of C-rate on the capacity of the cathode. Reproduced with permission from ref [126]. Copyright 2013 Wiley-VCH. (c, d) STEM-HAADF image and schematic showing formation of a surface rock-salt layer blocking the lithium channels underneath. Reproduced with permission from ref [69]. Copyright 2018 American Chemical Society.

Rate capability is another factor that affects the power/energy densities of the cathode. As demonstrated in Figure 15(b)[126], batteries working at higher C-rates exhibit reduced capacities. The rate capability of the cathode is determined by the intercalation kinetics of Li^+ cations at the atomic level. By this means, the more likely the cathode goes through oxygen loss, the more likely the layered phase transforms to a rock-salt like

structure with blocked Li channels, thereby reducing the Li^+ intercalation kinetics and the rate capability of the cathode.[280] Figures 15(c, d)[69] present the blocking of the lithium channels by TM cations via surface reconstruction, which reduces the rate capability of a NCA cathode. It has been shown[126] that Mn doping in layered oxides leads to a faster reduction in the rate capability compared with nickel and cobalt, probably because of the Jahn-Teller distortion associated with Mn cations. The Jahn-Teller distortion makes the Li channels less stable and vulnerable to the oxygen-loss-induced structural collapse,[281,282] thereby easily generating rock-salt like features that reduce the intercalation kinetics of Li^+.

6. Approaches towards Mitigating the Oxygen-Loss-Induced Structural Degradations

Due to its detrimental effects on the structural integrity and the associated electrochemical performance, a number of approaches have been made to mitigate the oxygen loss in layered cathodes, including surface coating and tuning the chemical activity of the cathode.

6.1 Surface Coating

As described above, oxygen loss and the associated structural degradations majorly occur through the particle surface. Therefore, stabilizing the surface of the particle can largely reduce the oxygen loss kinetics, thereby mitigating the associated structural and electrochemical degradations.

Figure 16(a)[283] summarizes three configurations of surface coating and their advantages and disadvantages: rough coating, core-shell coating and ultrathin film coating. These coatings differ in the configuration, preparation feasibility and functionally. The rough coating is achieved by non-uniform deposition of fine coating particles over the cathode surface. It is the easiest to prepare but cannot fully isolate the cathode particle from the electrolyte, thereby only mildly alleviating the degradation of the cathode. The core-shell coating provides a complete protection of the particle surface, but it may be too thick and reduces the ionic and electronic conductivity through the particle surface, thereby reducing the electrochemical kinetics of the cathode. To overcome this issue, a third coating configuration was thus developed, namely the ultrathin-film coating. This configuration has almost the same protecting effect as the core-shell coating, but its influence on the ionic and electronic conductivities is minimized by reducing the thickness of the coating layer. Due to its thin nature, the integrity of the ultrathin-film coating is fragile and highly sensitive to the synthesis and operating conditions. Small defects are commonly generated in the coating layer, which expose the active material underneath and undermine the protecting effect.

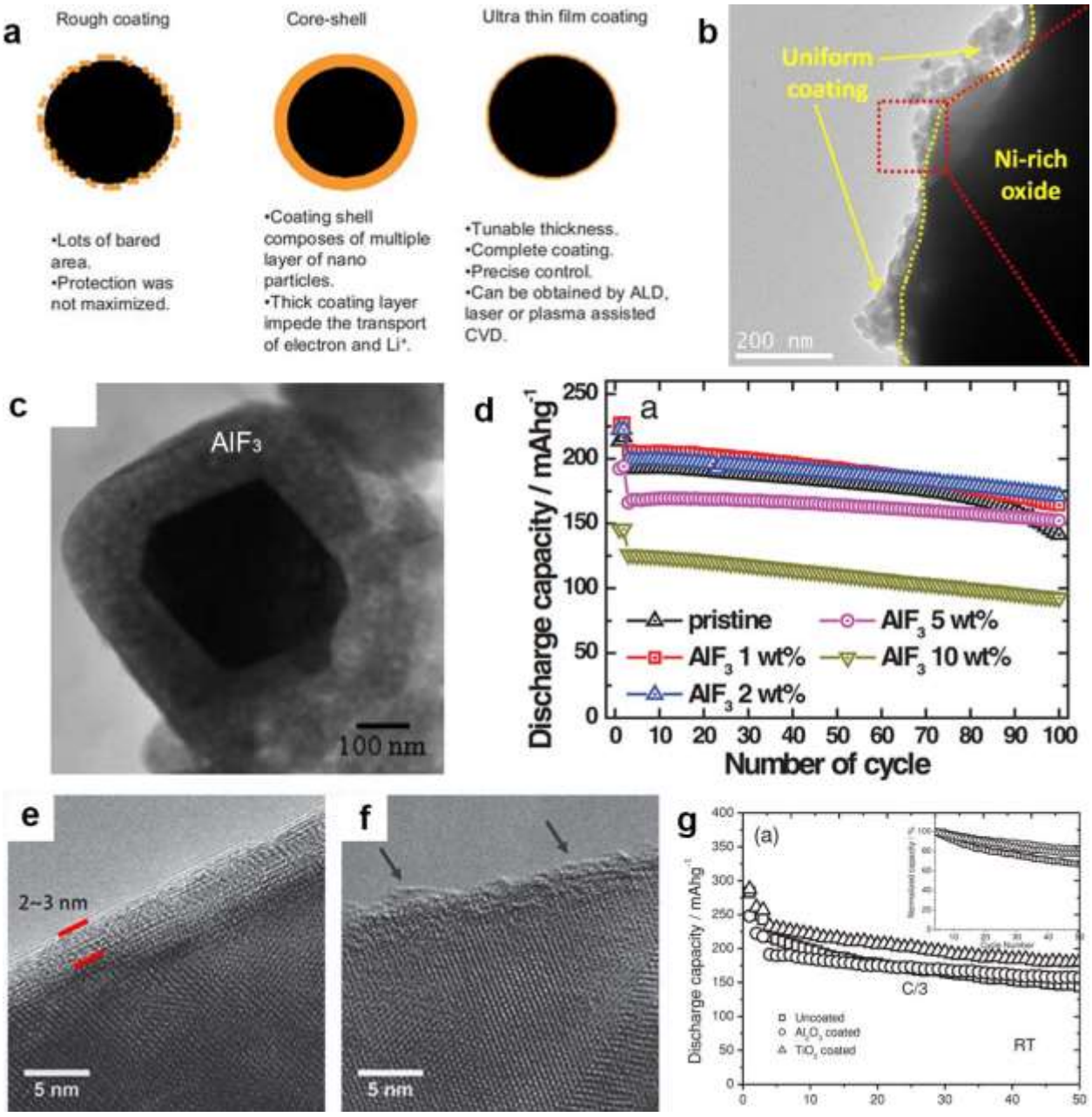

Figure 16 | Surface coating to mitigate oxygen loss. (a) Schematics showing three configurations of surface coating: rough coating, core-shell coating and ultrathin-film coating. Reproduced with permission from ref [283]. Copyright 2010 Royal Society of Chemistry. (b) TEM image of a $LiNi_{0.7}Co_{0.15}Mn_{0.15}O_2$ cathode particle coated with $LiZrO_3$ nanoparticles, an example of the rough coating. Reproduced with permission from ref [284]. Copyright 2017 American Chemical Society. (c) TEM image of a $Li[Li_{0.19}Ni_{0.16}Co_{0.08}Mn_{0.57}]O_2$ particle coated with AlF_3, an example of the thick core-shell coating. (d) Discharge capacity *vs* cycle number curves showing the influence of the AlF_3 surface coating on the capacity of the $Li[Li_{0.19}Ni_{0.16}Co_{0.08}Mn_{0.57}]O_2$ cathode. Reproduced with permission from ref [285]. Copyright 2012 Wiley-VCH. (e, f) Al_2O_3- and TiO_2-coated $Li_{1.2}Ni_{0.13}Mn_{0.54}Co_{0.1}O_2$ particles, which are examples of the ultrathin-film coating. (g) Discharge capacity *vs.* cycle number curves, showing the influence of the ultrathin-film Al_2O_3 and TiO_2 coatings on the discharge capacity. Reproduced with permission from ref [286]. Copyright 2013 Wiley-VCH.

The rough coating layer usually adopts metal oxide nanoparticles such as Al_2O_3, MgO, ZnO, SnO_2, TiO_2, RuO_2, and ZrO_2.[144,287] Figure 16(b)[284] presents a TEM view of a $LiNi_{0.7}Co_{0.15}Mn_{0.15}O_2$ particle coated with Li_2ZrO_3. As can be seen, Li_2ZrO_3 nanoparticles make up a highly porous shell, which can be permeable to the liquid electrolyte. The mobility of electrolyte thus determines the evolution of the degradation. When low-fluidity solid-state electrolytes are adopted, the rough coating sufficiently isolates the cathode from the electrolyte and improves its performance,[288] while it becomes less effective with high-fluidity electrolytes.

Compared with the rough coating, the core-shell coating has wider applications since it fully covers the electrochemically vulnerable particle surface, creating a protection against either flowable or solid-state electrolytes. Figure 16(c)[285] presents a $Li[Li_{0.19}Ni_{0.16}Co_{0.08}Mn_{0.57}]O_2$ particle coated with AlF_3. As can be seen, the particle is fully imbedded in AlF_3 without exposed surfaces. The influence of the AlF_3 coating on the electrochemical performance is presented in Figure 16(d). Compared with the pristine material, addition of 1 wt.% or 2 wt.% AlF_3 increases the capacity retention after 100 cycles without significantly changing the starting capacity. However, addition of AlF_3 to the amount of 5 wt.% or 10 wt.% does not further increase the capacity retention. On the other hand, too much AlF_3 leads to a loss of the starting capacity due to the reduced amount of the active $Li[Li_{0.19}Ni_{0.16}Co_{0.08}Mn_{0.57}]O_2$ material. Therefore, the optimized amount of coating material should be sufficient to protect the particle surface while avoiding excessive coating thickness that would sacrifice the capacity.

Based on this consideration, the coating layer should cover the entire particle surface with the minimized thickness. This leads to the development of the ultrathin film coating. An example is presented in Figures 16(e, f),[286] where $Li_{1.2}Ni_{0.13}Mn_{0.54}Co_{0.1}O_2$ particles are coated with Al_2O_3 and TiO_2 via atomic layer deposition (ALD). As shown in the discharge capacity *vs.* cycle number curves in Figure 16(g), the ultrathin surface coating notably increases the cyclic stability of the cathode without significantly affecting the capacity.

Among the three coating methods presented in Figure 16, the ultrathin film coating has the best, tunable electrochemical performance.[289] However, its fabrication requires ALD or chemical vapor deposition (CVD), which is relatively time-consuming and high cost. The core-shell coating has a balanced combination of performance and cost, which can be feasibly synthesized with chemical precipitation or hydrothermal methods and is currently widely adopted.[290–292]

Within the large family of surface coatings for layered oxides, it is repeatedly reported that some coating materials have superior performance than the others in terms of capacity retention, electrochemical kinetics, etc.[293] Figure 17(a)[294] presents capacity *vs.* cycle number curves of bare and ZnO-, Al_2O_3-, $Li_2O{\cdot}2B_2O_3$-, ZrO_2, ethanol- and MgO-coated $LiCoO_2$. The superior capacity retention of some coatings such as Al_2O_3 and ZnO demonstrates their better protecting effects against oxygen-loss related structural degradations. As shown in Figure 17(b), Cheng et al.[295] attributed this enhanced protection to the low diffusivity of oxygen in Al_2O_3 and ZnO, which prevents the oxygen loss from the cathode. Also, Al_2O_3 and ZnO can act as HF scavengers and moisture traps that reduce the surface oxygen loss.[161,296]

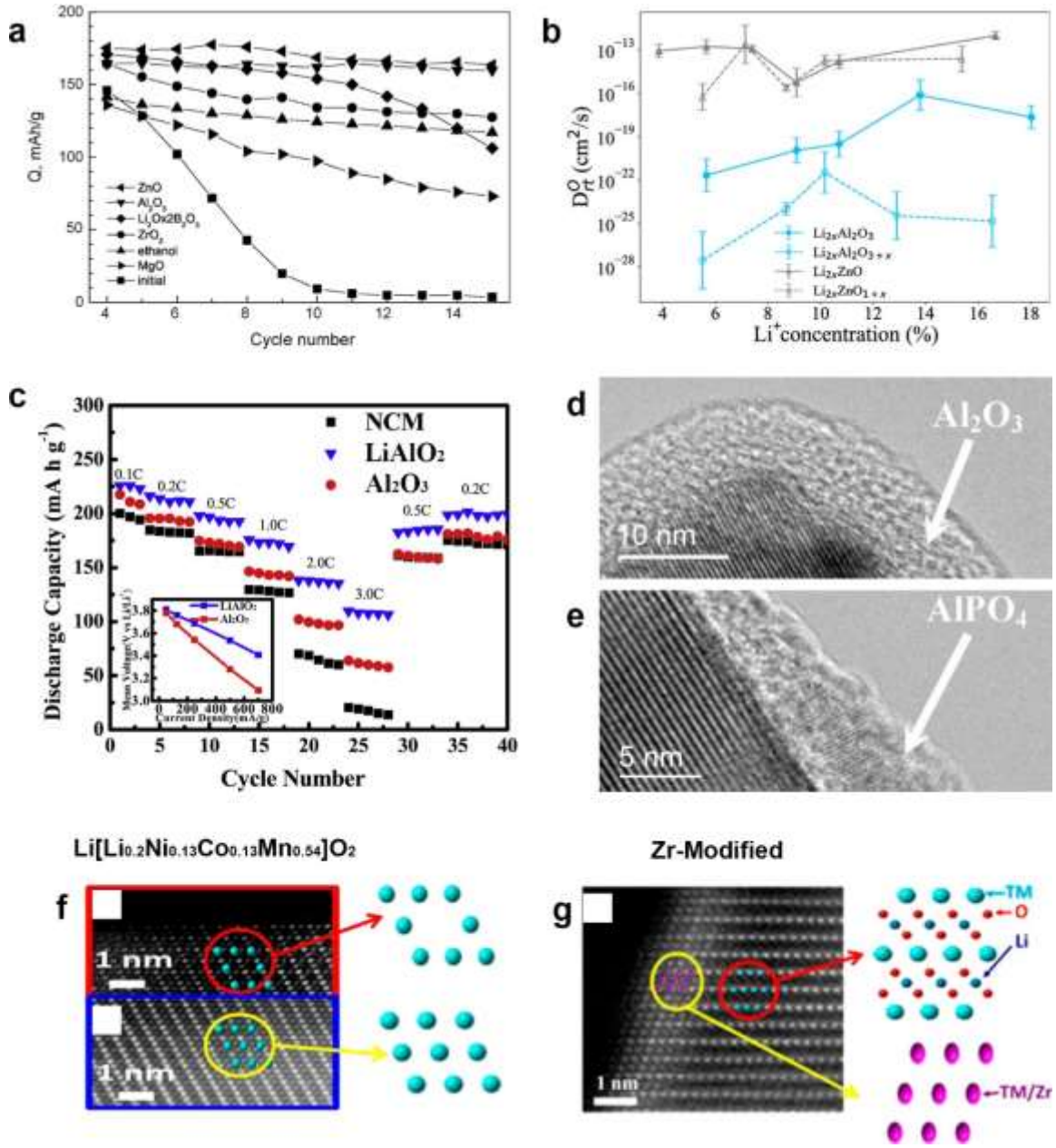

Figure 17 | Comparison of the performances of different coating materials. (a) Capacity *vs.* cycle number curves of bare and ZnO-, Al_2O_3-, $Li_2O{\cdot}2B_2O_3$-, ZrO_2, ethanol- and MgO-coated $LiCoO_2$. Reproduced with permission from ref [294]. Copyright 2007 Elsevier. (b) Calculated room-temperature self-diffusion coefficients of O^{2-} in Al_2O_3 and ZnO as a function of Li^+ concentration. Reproduced with permission from ref [295]. Copyright 2020 American Chemical Society. (c) Influence of $LiAlO_2$ and Al_2O_3 coating on the rate capability of the NMC 622 cathode. Reproduced with permission from ref [297]. Copyright 2018 Elsevier. (d, e) HRTEM images of the amorphous Al_2O_3 and crystalline $AlPO_4$. Adapted with permission from ref [298]. Copyright 2009 American Chemical Society. (f, g) STEM-HADDF images showing the protective effect of the Zr surface modification against the structural degradation of the $Li[Li_{0.2}Ni_{0.13}Co_{0.13}Mn_{0.54}]O_2$ cathode after 100 cycles. Adapted with permission from ref [299]. Copyright 2018 American Chemical Society.

Besides the capacity retention, rate capability is another important indicator for evaluating the surface coating. Figure 17(c)[297] presents the influence of $LiAlO_2$ and Al_2O_3 coating on the rate capability of the NMC 622 cathode, showing that the $LiAlO_2$ coating exhibits better rate capability compared with Al_2O_3, which is majorly attributed to its enhanced Li^+ conductivity. An ideal surface coating should have fast lithium-ion diffusion channels and fast electron-transfer channels for better electrochemical kinetics.[298] For instance, the high-conductivity, amorphous Al_2O_3 (Figure 17(d)[298]) is preferred over the low-conductivity, crystalline $AlPO_4$ (Figure 17(e)[298]).

In addition to the traditional design of surface coating that focuses on the insulation of the layered oxides from the hazardous electrolyte, Li et al.[299,300] also showed that, the intentionally induced surface degradation results in the formation of a thin layer of the $Fm\bar{3}m$ rock-salt structure, which serves as a preventive coating against the further degradation of the $R\bar{3}m$ layered phase underneath. Figure 17(f)[299] presents the atomic STEM-HAADF view of a $Li[Li_{0.2}Ni_{0.13}Co_{0.13}Mn_{0.54}]O_2$ cathode after 100 cycles, showing the generation of a degradation layer of ~10 nm, composed of the spinel and rock-salt phases. When the surface of the pristine $Li[Li_{0.2}Ni_{0.13}Co_{0.13}Mn_{0.54}]O_2$ cathode is modified with Zr, it exhibits a rock-salt surface layer of ~1 nm. This rock-salt surface coating along with the layered phase underneath remains almost unchanged after 100 cycles, as demonstrate by the STEM-HAADF view in Figure 17(g)[299].

Table 3 compares the advantages and disadvantages of different coating materials including oxides, carbon, phosphates and salts. The reader is referred to the review

articles by Chen et al.,[283] Zuo et al.,[301] Chen et al.,[289] Kalluri et al.[302] and Li et al.[293] for more discussion regarding the different coating materials, their preparation and applications.

Table 3 | Surface coating materials for layered oxides.

Type	Examples	Advantages	Disadvantages	References
Oxides	Al_2O_3, ZnO, MgO, TiO_2, SiO_2, ZrO_2	Stable against electrolytes; good capacity retention.	Reduced ionic and electronic conductivity. The oxide can exhibit varied morphologies and crystallinities, resulting in non-uniform surface coating (amenable with conformal coating by ALD).	Chen et al.;[283] Muratahan et al.[303]
Carbon	Graphene; carbon black	Best ionic and electronic conductivities.	Carbon can be easily burn out by oxygen during synthesis. Carbon also creates a more reductive environment and accelerates the oxygen loss of layered oxides.	Li et al.;[304] Cao et al.[305]
Phosphate	$AlPO_4$; $Co_3(PO_4)_2$; Li_3PO_4	Low costs; low processing temperatures; good capacity retention.	Low ionic and electronic conductivities.	Ma et al.;[306] Tan et al.[307]
Salts	AlF_3; LaF_3; $MnSiO_4$; $LiNbO_3$	Low cost; feasible to fabricate; stable against electrolytes.	Low ionic and electronic conductivities.	Lin et al.;[308] Li et al.[309]; Xin et al.[310]

Figure 18(a)[311] presents a CeF_3 coating layer on a $Li[Li_{0.2}Mn_{0.54}Ni_{0.13}Co_{0.13}]O_2$ particle, and Figures 18(b, c)[311] compares the charge-discharge kinetics of the uncoated and coated $Li[Li_{0.2}Mn_{0.54}Ni_{0.13}Co_{0.13}]O_2$ cathode (CV curves). As can be seen, the cathodic

peak of the coated cathode is much sharper and more symmetric compared with the bare electrode, indicating that the discharge kinetics of the coated cathode are well maintained during cycling without showing discharge voltage fades. Also, the CV curves of the coated cathode shows very little cycling-induced changes compared with the bare cathode, indicating the enhanced structural stability by the coating.

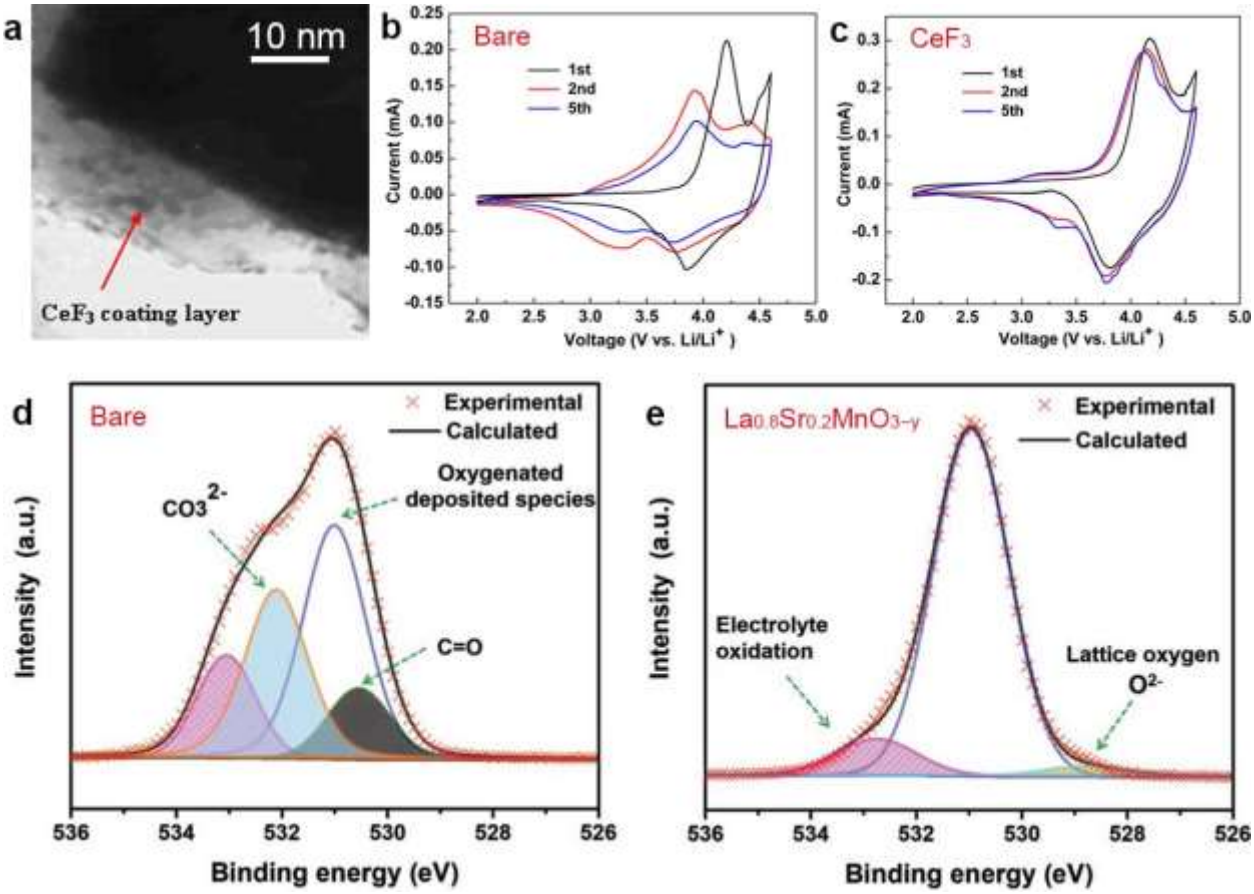

Figure 18 | The influence of surface coating on the oxygen loss kinetics. (a) TEM view of a CeF_3 coating layer on a $Li[Li_{0.2}Mn_{0.54}Ni_{0.13}Co_{0.13}]O_2$ particle. (b, c) Cyclic voltammetric (CV) profiles of bare and CeF_3-coated $Li[Li_{0.2}Mn_{0.54}Ni_{0.13}Co_{0.13}]O_2$ cathodes, respectively. Reproduced with permission from ref [311]. Copyright 2014 Elsevier. (d, e) O 1s XPS spectra of bare $Li_{1.2}Ni_{0.13}Co_{0.13}Mn_{0.54}O_2$ cathode and its counterpart coated with $La_{0.8}Sr_{0.2}MnO_{3-y}$, obtained after 200 electrochemical cycles. Reproduced with permission from ref [312]. Copyright 2019 Wiley-VCH.

Figures 18(d, e)[312] compare the O 1s XPS spectra of bare $Li_{1.2}Ni_{0.13}Co_{0.13}Mn_{0.54}O_2$ cathode and its counterpart coated with $La_{0.8}Sr_{0.2}MnO_{3-y}$. After 200 electrochemical cycles, the two cathodes exhibit distinct oxygen loss patterns. Intensive peaks of oxidized species are generated in the uncoated cathode, while the coated electrode shows only slight signs of oxidation. The intensive oxygen loss from the uncoated electrode results in the oxidation of electrolyte, thereby forming a layer of oxidized species on the particle surface.

In summary, the surface coating separates the electrochemically active cathode material from directly contacting the electrolyte, thereby mitigating oxygen loss and the associated degradation. On the other hand, the influence of delithiation remains in driving structural degradations in the cathode. As we have discussed in Figure 10, unlike the electrolyte-induced structural degradation that preferably occurs in the surface, delithiation drives degradations across the whole particle. The delithiation-associated degradations are usually mitigated by tuning the chemical activity of the cathode, as discussed below.

6.2 Tuning the Chemical Activity

Besides the surface coating of cathode particles, efforts have also been made by adding stabilizing elements into the cathode to reduce the chemical activity of oxygen and prevent its loss.[244,313–315] An example is the tuning of the chemical composition of NMC cathodes. Increasing the Ni content is beneficial for the capacity, but it is detrimental to the cycling performance,[316–319] as we have discussed in subsection 4.2. By contrast, a higher Co content is beneficial for the structural stability but yields a lower capacity, and

Co is an expensive element.[8,320,321] Mn also increases the structural stability, but it introduces the John-Teller lattice distortion that is a potential source of degradations upon the electrochemical cycling.[322,323] Accordingly, optimizing the chemical composition of Ni, Co and Mn becomes a critical task in tuning the structural and electrochemical stability of the NMC cathodes,[324,325] as well as maintaining satisfactory electrochemical properties at the same time.

Figure 19(a)[264] presents the discharge capacity *vs.* cycle number curves of NMC cathodes with varying Ni contents. As can be seen, the 85%-Ni cathode has the highest starting capacity, while only 65% of the starting capacity is retained after 100 cycles. Lowering the Ni content increases the cycling stability of the cathode at a cost of the starting capacity. For instance, the $Li[Ni_{1/3}Co_{1/3}Mn_{1/3}]O_2$ cathode with only 33.33% Ni retains ~92.4% of the starting capacity after 100 cycles, but its starting capacity is only ~150 mAh · g^{-1}, much lower than that of the $Li[Ni_{0.85}Co_{0.075}Mn_{0.075}]O_2$ cathode (~ 200 mAh · g^{-1}). Therefore, the Ni content needs to be optimized for a balanced combination of discharge capacity and cycling stability.

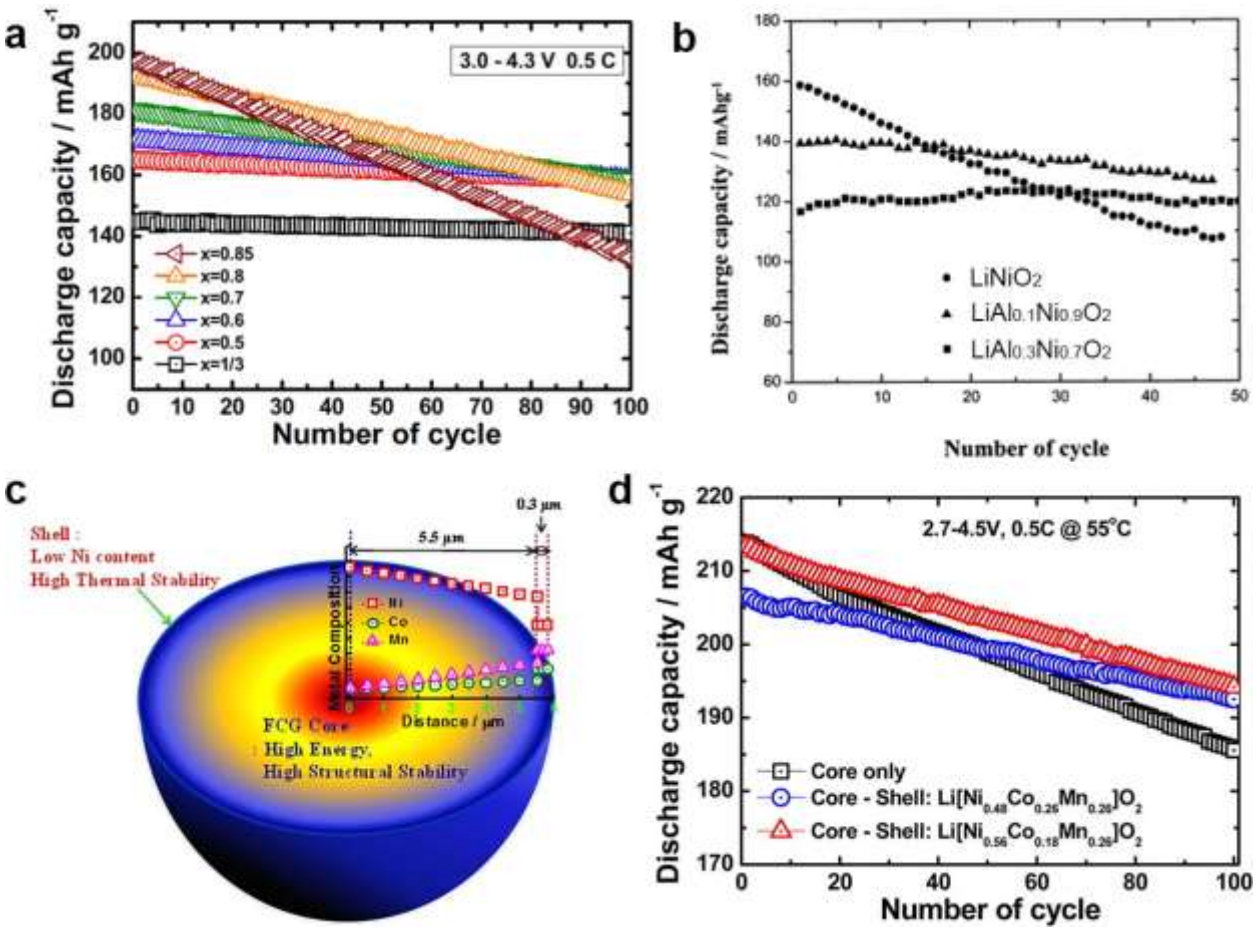

Figure 19 | Tuning the chemical activity of the cathode. (a) Discharge capacity *vs.* cycle number curves of NMC cathodes with different Ni contents. Reproduced with permission from ref [264]. Copyright 2013 Elsevier. (b) Discharge capacity *vs.* cycle number curves of Al-doped $LiNiO_2$ cathodes, indicating that Al doping increases the cycling stability while reducing the starting capacity. Reproduced with permission from ref [326]. Copyright 2001 Elsevier. (c) Schematic of a core-shell configuration resulting from the chemical gradient in a particle, where the chemical composition changes from $Li[Ni_{0.86}Co_{0.07}Mn_{0.07}]O_2$ to $Li[Ni_{0.67}Co_{0.09}Mn_{0.24}]O_2$ from the center to the surface. An extra shell of either $Li[Ni_{0.48}Co_{0.26}Mn_{0.26}]O_2$ or $Li[Ni_{0.56}Co_{0.18}Mn_{0.26}]O_2$ is added in the surface. (d) Discharge capacity *vs* cycling number curves of the core-only, core + $Li[Ni_{0.48}Co_{0.26}Mn_{0.26}]O_2$ shell, and core + $Li[Ni_{0.56}Co_{0.18}Mn_{0.26}]O_2$ shell, respectively, as shown in (c). Reproduced with permission from ref [327]. Copyright 2014 American Chemical Society.

Another example of tuning the chemical activity of oxygen is the doping of Al.[328–330] Unlike the Co and Mn stabilizers for the layered oxides, the Al^{3+} substitution only stabilizes the crystal lattice without participating in the electrochemical redox reaction.[31,331] Therefore, the content of Al^{3+} cations cannot be too high since it is

electrochemically inactive. Figure 19(b)[326] illustrates the influence of Al doping on the electrochemical performance of the $LiNiO_2$ cathode. As can be seen, doping of 10% Al ($LiAl_{0.1}Ni_{0.9}O_2$) slightly reduces the starting capacity of the $LiNiO_2$ cathode (from ~160 mAh · g^{-1} to ~140 mAh · g^{-1}), but the cycling stability is significantly increased. The $LiAl_{0.3}Ni_{0.7}O_2$ cathode has an even better cycling stability compared with $LiAl_{0.1}Ni_{0.9}O_2$, while its starting capacity is further reduced (~118 mAh · g^{-1}).

To overcome the trade-off between the capacity and the stability shown in Figures 19(a, b), approaches[332,333] have been made to build cathode particles with core-shell configurations where the stabilizing elements are enriched in the surface and a high concentration of Ni remains in the bulk, as exemplified in Figures 19(c, d).[327] The stable shell protects the high-capacity core, resulting in cathode particles with the optimized cycling stability and electrochemical performance. As shown in Figure 19(c), the primary particle exhibits a well-defined core-shell configuration with the Ni content decreasing from the bulk towards the surface. Figures 19(d) presents discharge capacity *vs.* cycle number curves of three cathodes: the core-only material where the chemical composition changes from $Li[Ni_{0.86}Co_{0.07}Mn_{0.07}]O_2$ to $Li[Ni_{0.67}Co_{0.09}Mn_{0.24}]O_2$ from the center to the surface, the core + a $Li[Ni_{0.48}Co_{0.26}Mn_{0.26}]O_2$ shell, and the core + a $Li[Ni_{0.56}Co_{0.18}Mn_{0.26}]O_2$ shell. As can be seen, the particle with a $Li[Ni_{0.56}Co_{0.18}Mn_{0.26}]O_2$ shell combines the advantages of the rest two cathodes. The starting capacity of the particle with a $Li[Ni_{0.56}Co_{0.18}Mn_{0.26}]O_2$ shell is almost the same as that of the core-only material (~215 mAh · g^{-1}), while its cycling stability is dramatically enhanced with a higher retaining capacity than the other two cathodes after 100 cycles.

6.3 Increasing Lithium Content in the SEI and Electrolyte

As discussed in subsections 2.1 and 2.2, O^{2-} from the cathode can electrochemically or chemically combine with Li^+ in the electrolyte to form Li_2O, which can be described with the following equation:

$$2Li^+ + O^{2-} = Li_2O. \quad (3)^{334}$$

The equilibrium constant K_c of reaction (3) can be calculated as following:

$$K_c = [Li_2O]/([Li^+]^2 \cdot [O^{2-}]), \quad (4)$$

where $[Li_2O]$, $[Li^+]^2$ and $[O^{2-}]$ are the equilibrium concentrations of the corresponding reactants and products. Since the Li_2O is solid, $[Li_2O]$ has the value of 1. K_c has a constant value at a fixed temperature. Therefore, the concentration of O^{2-} in the electrolyte is inversely proportional to the concentration of Li^+. Increasing the concentration of lithium salts thus reduces the concentration of O^{2-}, which in turn reduces the driving force for the migration of lattice oxygen from the cathode into the electrolyte.

Based on this consideration, addition of Li^+-containing salts into the electrolyte reduces the tendency of the loss of lattice oxygen from the cathodes to the electrolyte. Figure 20(a)[335] shows NMC cathodes cycled with electrolytes of different $LiPF_6$ contents, indicating that a higher $LiPF_6$ content significantly enhances the capacity retention.

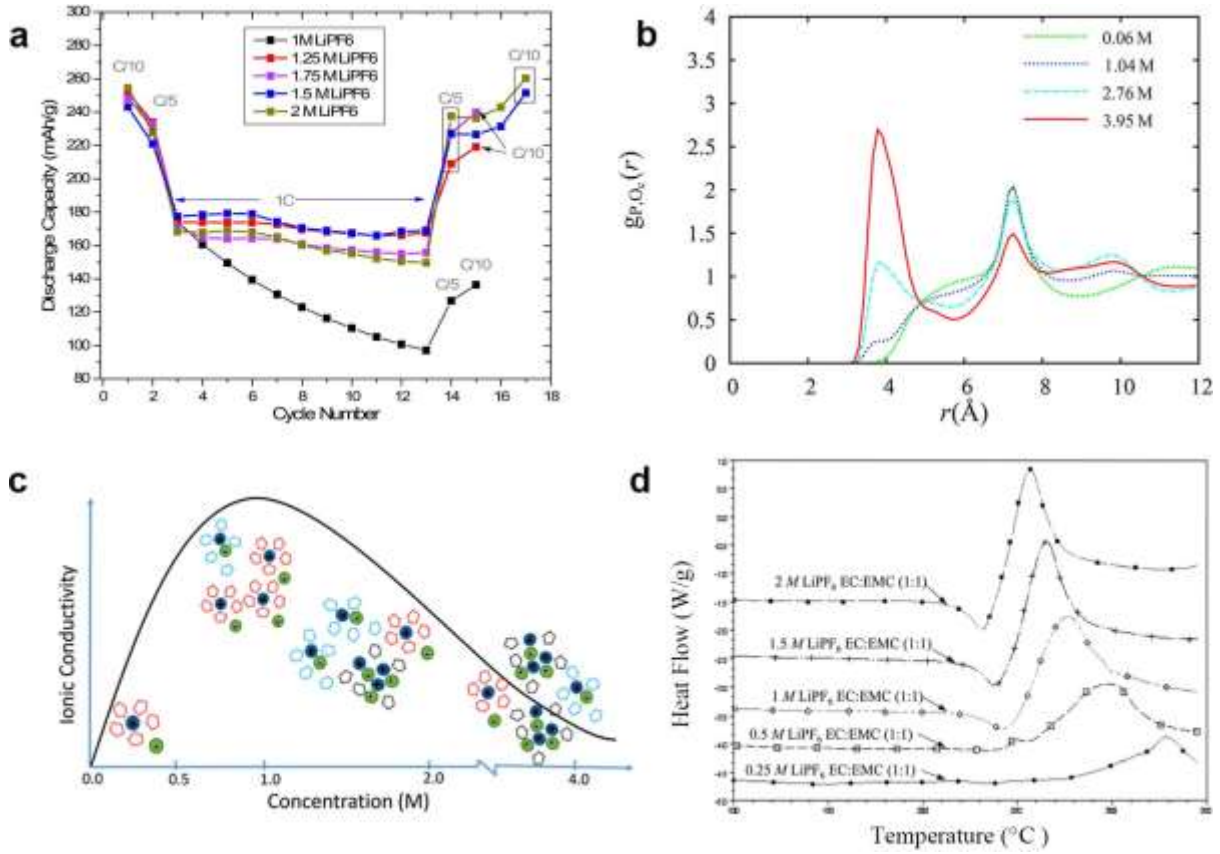

Figure 20 | Influence of Li content in the SEI and electrolyte on the electrochemical performance. (a) Discharge capacity *vs.* cycle number curves of NMC cathodes with different $LiPF_6$ contents in the electrolyte, showing that a higher $LiPF_6$ content increases the electrochemical stability. Reproduced with permission from ref [335]. Copyright 2017 Elsevier. (b) RDF values of electrolytes with different $LiPF_6$ concentrations, indicating that a higher $LiPF_6$ concentration increases the stability of PF_6 cation. (c) MD simulation of the effect of $LiPF_6$ concentration on the ionic conductivity, showing that the maximum conductivity is achieved around 1M. Reproduced with permission from ref [336]. Copyright 2018 American Chemical Society. (d) DSC analysis of EC:EMC (1:1) electrolyte with different $LiPF_6$ concentrations, indicating that the thermal stability decreases with increased $LiPF_6$ concentrations. Reproduced with permission from ref [337]. Copyright 2001 Elsevier.

Moreover, the increase of $LiPF_6$ content also stabilizes itself and thus prevents the formation of LiF as one of the main SEI components, which has been identified as the main reason for the reduced ionic conductivity through the SEI layer, as shown by molecular dynamics (MD) simulations. Figure 20(b)[336] presents the radial distribution function (RDF) values of electrolyte with different $LiPF_6$ concentrations, showing that a

higher $LiPF_6$ concentration stabilizes itself and thereby reduces its interaction with the electrode and the associated oxygen loss.

Although increasing the $LiPF_6$ content can prevent the oxygen loss, extra addition of $LiPF_6$ also decreases the diffusivity of Li^+ cations and thus the ionic conductivity of the electrolyte, as demonstrated in Figure 20(c),[336] where the highest ionic conductivity is achieved around 1M. Therefore, the concentration of the $LiPF_6$ salt in the electrolyte should be carefully optimized to sufficiently prevent the electrolyte decomposition and oxygen loss, while avoiding excessive $LiPF_6$ that would decrease the ionic conductivity.

Besides the ionic conductivity, the overly high lithium salt concentration also decreases the thermal stability of the electrolyte, generating a potential source of fire hazard. Figure 20(d)[337] presents differential scanning calorimetry (DSC) analysis of EC:EMC (1:1) electrolytes (EC: ethylene carbonate; EMC: ethyl methyl carbonate) with different $LiPF_6$ concentrations, indicating that the thermal stability decreases with the increased $LiPF_6$ concentration.

6.4 Thermodynamic and Kinetic Considerations in Mitigating the Oxygen Loss

Wang et al. [338] calculated the reaction enthalpy for the decomposition of $LiCO_2$ as a function of the Li extraction, as presented in Figure 21(a). The negative overall reaction enthalpies (square points in Figure 21(a)) indicate that the decomposition is exothermic at various SOC levels, meaning that it is energetically favorable. Hu et al.[339] calculated the influence of temperature on the formation energy of the oxygen vacancy within layered oxides (Figure21(b)), showing that the formation energies become negative

around 300~800K in fully delithiated cathodes. These temperatures are commonly reachable in battery cells.[340,341]

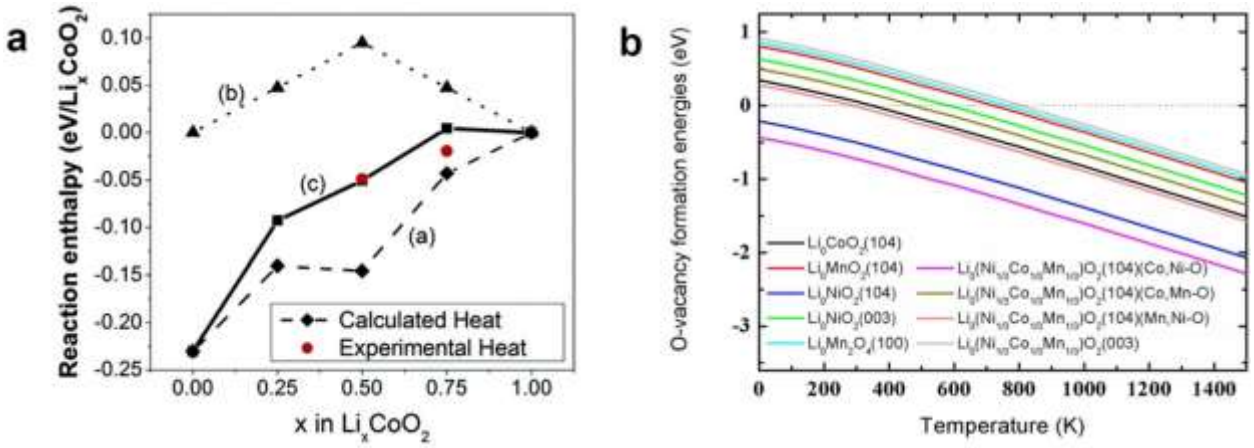

Figure 21 | Thermodynamics of oxygen loss. (a) Calculated and experimental enthalpies for the decomposition of layered Li_xCoO_2 as a function of the Li composition *x*. The diamond points are the calculated reaction heat for the layered-to-spinel composition, the triangle points represent the reaction heat for the spinel decomposition, and the square points show the overall reaction heat for the direct decomposition of layered Li_xCoO_2. Reproduced with permission from ref [338]. Copyright 2007 American Chemical Society. (b) Calculated oxygen vacancy formation energies as a function of temperature. Reproduced with permission from ref [339]. Copyright 2020 Elsevier.

Therefore, it is thermodynamically impossible to fully prevent the oxygen loss from layered oxides under the operating conditions of Li-ion batteries from the electrochemical perspective. The mitigating methods presented in this section aim at slowing down the oxygen loss kinetics by establishing semi-stable conditions. This is similar as the cathode activation during the first charge, by which the active material in the surface is reconstructed via significant oxygen loss, whereas the active materials underneath are well protected.[38,342] The subsequent oxygen loss thus becomes much attenuated. Failure in maintaining the structural or chemical foundations for the semi-stability, such as the breakage of the surface coating or loss of the elemental stabilizer, will again set off the

oxygen loss. For instance, cracking during electrochemical cycling exposes the intact active material in the particle core and induces significant oxygen loss.[343]

7. Computational Modeling of Oxygen Loss

Computational approaches such as DFT and MD are important techniques for understanding the atomistic mechanisms of oxygen loss. Due to the limitation of the characterization techniques, challenges remain in measuring the oxygen loss kinetics and the evolution of atomic and electronic configurations accompanying the oxygen loss. The computational methods can play an important role in providing fundamental insight into the atomistic mechanisms to complement the experimental measurements.

A major way for understanding the oxygen loss is to explore different kinetic pathways and compare their feasibilities via computational methods. Figures 22(a, b)[344] present DFT analysis of the influence of the configuration of oxygen vacancies on the migration energy barriers of Ni cations. The presence of oxygen vacancies reduces the repulsion to the migration of Ni cations, and the various positions of the oxygen vacancies generate different energy barriers, making it possible to distinguish and select among varying transformation pathways. According to Figure 22(b), the V_O1 + V_O2 vacancy configuration has the lowest energy barriers and thus is the most feasible pathway for structural degradation. The DFT and MD methods work well with evaluating the kinetic transformations among different crystallographic and electronic configurations. Therefore, a critical step in the modeling is to elucidate specific configurations and the pathways governing their transformations. A major achievement of the DFT method is to determine

the layered → spinel → rock-salt pathway of phase transformation.[345–347] Besides the experimental evidence supporting this pathway, DFT calculations indicate that the layered → spinel → rock-salt transformation sequence upon the oxygen loss is also a kinetically and thermodynamically favorable process.[348,349]

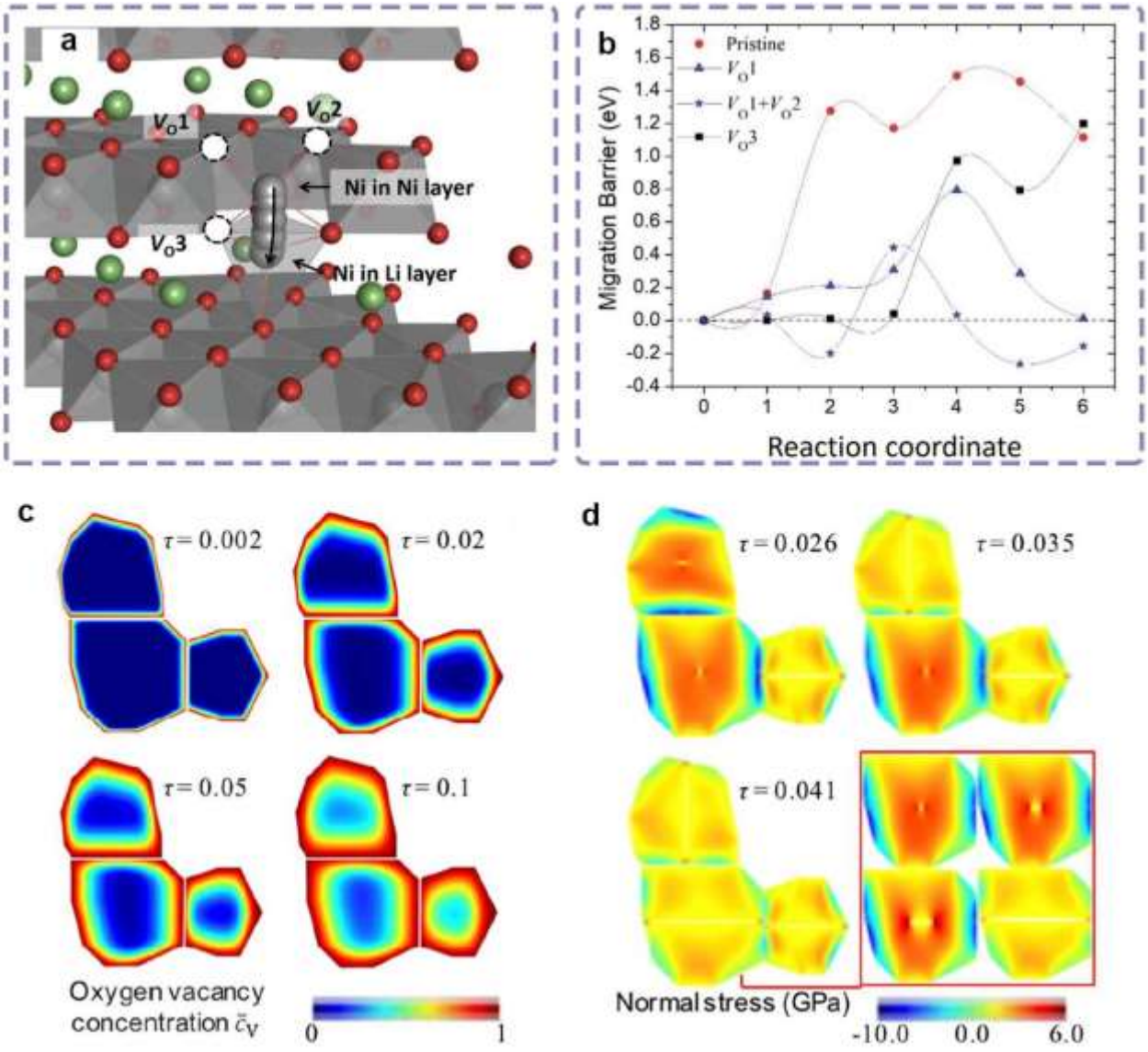

Figure 22 | Atomistic simulations of the oxygen loss kinetics. (a, b) Comparing the oxygen-loss feasibilities among various positions of oxygen vacancies. Reproduced with the permission from ref [344]. Copyright 2019 Wiley-VCH. (c, d) Finite element modeling of the preferable evolution of oxygen vacancies and cracking along the grain boundaries of NMC cathodes. Reproduced with the permission from ref [222]. Copyright 2018, American Chemical Society.

Figures 22(c, d)[222] present a kinetic pathway for cracking determined with finite element modeling. Figure 2(c) presents time-dependent evolution of oxygen vacancies in a NMC cathode, indicating preferable formation of oxygen vacancies along the grain boundaries. Figure 22(d) shows the formation kinetics of cracking, which also preferably evolves along the grain boundaries. The matched kinetics between oxygen vacancy formation and inter-granular cracking confirms the driving effect of oxygen loss on the cracking.

8. Summary and Outlook

Oxygen loss has been identified as a major cause for the structural and electrochemical degradations in layered oxide cathodes, and extensive work has been performed to understand the chemical, crystallographic and electronic features of this process. The driving forces for oxygen loss have been attributed to delithiation, side reactions and intrinsic thermodynamic instability of the layered oxides. Structural degradations induced by oxygen loss include reduction of TM cations, phase transformation, formation of atomic vacancies of oxygen, cavitation and cracking. The electrochemical cycling drives oxygen loss and the associated structural degradations, which in turn degrades the electrochemical performance. Approaches have been taken to understand and mitigate oxygen loss from layered oxides, while characterization methods revealing a full structural-electronic picture or real-time kinetics of oxygen loss

are still in a great lack. Table 4 summarizes the major experimental approaches towards probing the oxygen loss.

Table 4 | Experimental methods for probing the oxygen evolution.

Name	Description	References
C-V Curve	Analyzing the influence of oxygen loss on the electrochemistry. The LMR oxides exhibit an evident irreversible first-cycle voltage plateau, while the classical layered cathodes show no significant features.	Sun et al.[350]; Xu et al.[67]; Mesnier et al.[351]
DEMS, IRS and other Gas Analyzers	Correlating the oxygen content in the surrounding atmosphere with the electrochemical conditions. Measuring the release of oxygen from both the lattice and the side reactions with the electrolyte. Isotopic labeling allows for tracking the origin of the released oxygen.	Guéguen et al.[352]; Berkes et al.[353]; Armstrong et al.[38]; Renfrew et al.[354]
XPS/HAXPES	Probing the electronic configuration and evolution during oxygen loss. Providing depth-profile information regarding the extent of metal reduction due to oxygen loss.	Koga et al.[122]; Qiu et al.[93]; Lebens-Higgins et al.[355]
TEM/STEM	Imaging: morphological/crystallographic analysis of phase transformations and defect formation induced by oxygen loss. Diffraction: crystallography and phase transformations. EELS/EDS: chemical shift and composition changes. STEM-ABF: imaging O and Li with the atomic resolution.	Fell et al.[208]; Zhang et al.[91]; Xu et al.[62]; Gu et al.[356]
Soft XAS/RIXS	Like EELS, soft L-edge XAS can provide information regarding the oxygen loss. Depth-dependent information can be determined from employing electron and fluorescent yield modes. O K-edge RIXS has proven a valuable tool for examining oxygen participation at high voltages.	Kleiner et al.[357]; Wang et al.[358]; Yabuuchi et al.[359]; Wu et al.[360]; Lebens-Higgins et al.[361]
NMR	^{17}O NMR allows for direct probing of the oxygen environment. Precisely measuring the chemical transitions of lithium within layered oxides and the electrolyte, revealing the associated oxygen loss.	Jiang et al.[362]; Liu et al.[363]; Jin et al.[364]; Seymour et al.[365]

As we have illustrated across this review, combining the different analytical techniques is a viable solution for revealing a full picture of the morphology, chemistry, electrochemistry and kinetics of the oxygen loss. However, asynchronous experiments are hard to be precisely correlated with sufficient spatial (atomic-level) and time resolutions (seconds or hundreds of microseconds), even if they are performed under the same electrochemical condition. A one-stop *operando* approach yielding comprehensive information is thus urgently called. Because of its capability to probe the fast dynamics of local structure and chemistry at the atomic scale, *in situ* TEM equipped with advanced EDXS/EELS detectors and mass spectroscopy may be an icebreaker for resolving the data asynchrony. High-resolution EDXS/EELS mapping can potentially reveal the trajectories of oxygen within cathode lattice and the electrolyte, as well as within the solid-electrolyte interface (SEI).[366–368] Additionally, mass spectroscopy installed within the TEM can measures the oxygen released in the gaseous form.[369,370] Besides the promising future of the TEM-based approach, it has a major challenge: a full battery cell setup containing both electrodes and electrolyte has to be established within the TEM. Considering the challenges in constructing such a cell, a viable *operando* protocol is yet to be developed for the electron-beam-based microscopic studies. The complexities in assembling such a cell are also potential sources of artifacts, including the sample preparation as well as electron beam irradiation effects. For instance, the thickness of the TEM sample must be reduced to tens of nanometers, which becomes more vulnerable to degradations due to the significantly increased surface-area to bulk ratio[103,371]. The membrane windows in the liquid-cell stage together with the electrolyte reduce the visibility of the microstructure[372,373]. Also, the ion-beam utilized for the sample

preparation[374,375] and the e-beam utilized for observation[183,376] can potentially induce the degradation & decomposition of the layered oxide and electrolyte. Besides the TEM-based method, there are also some initial successes in *operando* photoemission spectroscopy studies of full batteries by employing the higher probing depth of hard X-ray photoelectron spectroscopy (HAXPES),[377] using set-ups akin to those for soft XAS.[378]

A promising approach for capturing the oxygen loss process as well as preventing the potential artifacts by the electron/ion irradiation is the application of cryo-FIB (focused ion beam) and cryo-TEM by freezing the sample to a tunable temperature as low as -170°C, thereby drastically reducing the beam-damage kinetics.[379–381] Since the work by Cui et al.[380] demonstrating that the cryo-TEM has the capability to yield atomic resolution TEM images from beam-sensitive Li dendrites (Figures 23(a-c)), the cryo-based methods have been increasingly applied in the observation of battery materials. Figure 23(d)[382] presents the HRTEM observation of an SEI on electrochemically deposited Li metal, enabled by cryo-TEM. The SEI layer, which is extremely unstable under the regular TEM imaging conditions,[183,383,384] are well maintained by the low temperature. As the SEI is a major degraded microstructure resulting from oxygen loss, elucidating its atomic structure and composition serves as a meaningful complement for understanding the oxygen loss kinetics. Cryo-TEM is also demonstrated to enable high-resolution EDS and EELS spectroscopy and mapping with the beam-sensitive SEI,[385–387] as exemplified in Figure 23(e)[388], which greatly expands its potential application.

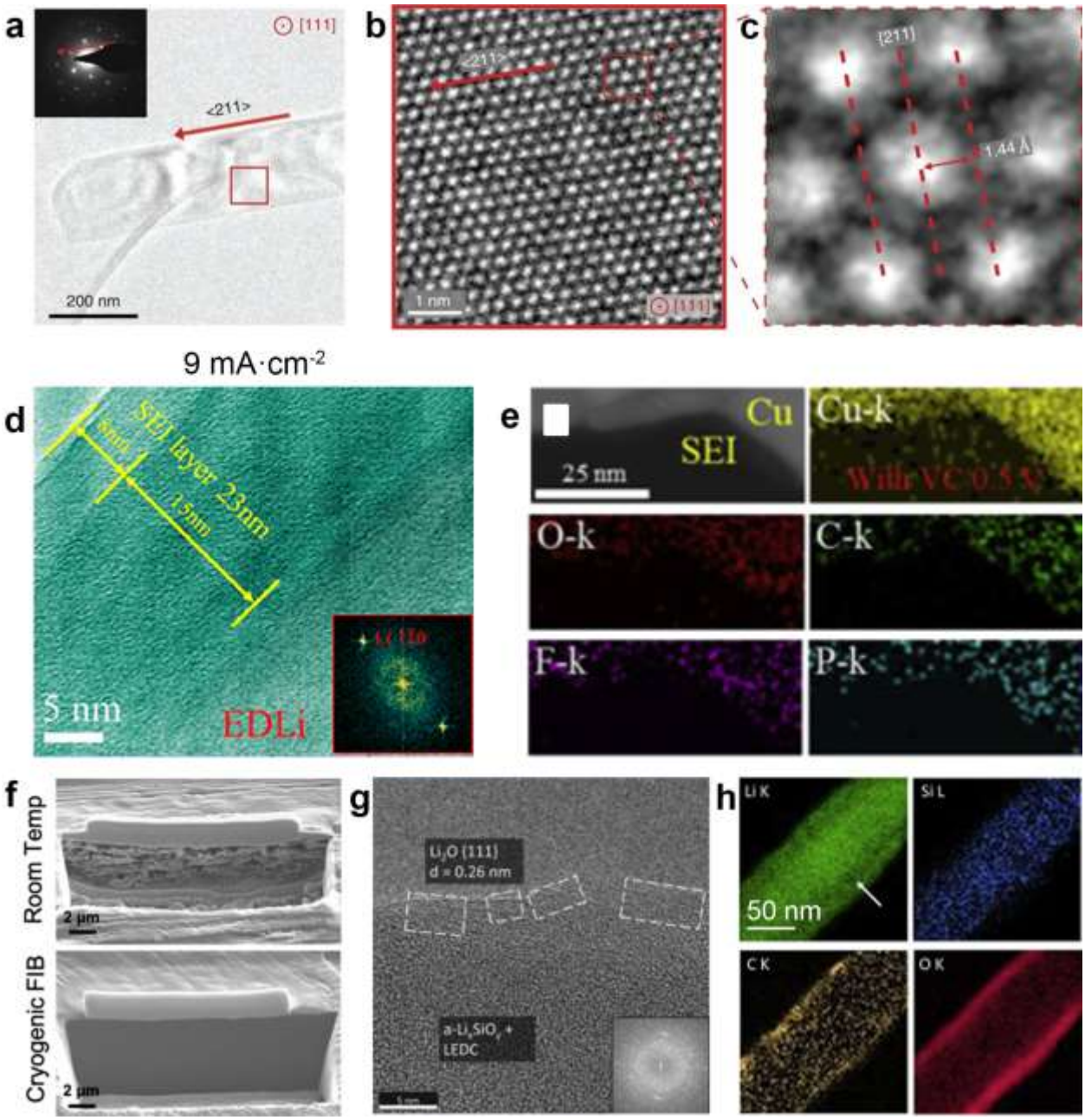

Figure 23 | The applications of cryo-FIB, cryo-TEM and liquid TEM techniques in analyzing LIBs. (a-c) Cryo-TEM enables atomic-resolution observations of Li dendrites. Reproduced with permission from ref [380]. Copyright 2017 American Association for the Advancement of Science. (d) Cryogenic HRTEM imaging of an SEI layer on the surface of electrochemically deposited Li metal. Reproduced with permission from ref [382]. Copyright 2020 American Chemical Society. (e) Cryo-TEM-assisted EDS mapping of the SEI layer, showing the presence of light elements as O, F, C and P. Adapted with permission from ref [388]. Copyright 2020 Elsevier. (f) Comparison of Li foils prepared by the room-temperature and cryogenic FIB, highlighting the protection effect of cryo-FIB against beam damage. Reproduced with permission from ref [389]. Copyright 2019 American Chemical Society. (g) HRTEM view of the Li_2O SEI on a Si nanowire, enabled by liquid TEM. (h) EELS mapping of the SEI formed on a Si nanowire with liquid TEM. Reproduced with permission from ref [383]. Copyright 2019 Elsevier.

Cryo-FIB has been shown to be a powerful approach for preparing cryo-TEM samples, which further expands the capabilities of cryo-TEM.[368,390] Figure 23(f)[389] compares the ion beam damage by room-temperature and cryogenic FIB, confirming the significant improvement of cryo-FIB against the beam damage. Lee et al.[389] reported that the protection is so good that the ion-intensive and time-consuming 3D tomography reconstruction can be performed on a Li foil within the cryo-FIB without introducing observable damages. Therefore, the combination of cryo-FIB and cryo-TEM serves as a promising tool for probing the microstructural evolution induced by oxygen loss and thus the oxygen loss kinetics. Also, cryo-ultramicrotome can prepare TEM samples with a diameter of millimeters,[391,392] which yields a good efficiency of sample preparation and can be a powerful supplement for cryo-FIB by providing samples of a few micrometers in diameter. The capabilities of the cryo-based methods can be even further expanded if combined with STEM annular bright filed (STEM-ABF) imaging, which has the capability to directly image light elements such as O and Li at the atomic resolution.[356,393]

Another promising approach for preventing the electron beam irradiation effect within the TEM is the liquid-cell technique, which has also been shown to maintain the structural integrity of beam sensitive SEI, as demonstrated in Figure 23(g)[383]. With liquid TEM, EELS maps of light elements such as Li, C and O can be also obtained from the SEI with the nanometer-resolution (Figure 23(h)[383]), confirming its capability in probing the oxygen loss. Different from the cryo-TEM, the e-beam can generate H^+ in the solution of liquid TEM and reduce the pH value,[394,395] which needs to be closely evaluated when applied in probing the oxygen loss, as H^+ can easily react with the layered oxide cathodes.

Additionally, monitoring the gaseous emissions from the cathode such as O_2, CO and CO_2 is necessary for probing the oxygen loss kinetics. DEMS and infrared techniques yield good correlation between the electrochemical process and gas emission, thereby making it feasible to plot the oxygen loss as a function of electrochemistry.[353,396] Examples of gas analysis can be found in Figures 3(a), 4(b) and 13(a). On the other hand, fundamental understanding of the gassing analysis results is not straightforward. For instance, no spatial information regarding the oxygen loss kinetics can be revealed. It is also hard to trace the origin of the emitted gases, which may come from either the electrolyte or the oxide cathode, although isotope labeling is being employed to track the origin of oxygen[354]. A potentially satisfying solution for this problem is to couple the gas analysis with other characterization techniques. For instance, DENSsolutions BC[397] and Protochips Incorporated.[398] have developed TEM holders with gas analyzers working synchronously with *in-situ* TEM characterization, which greatly expands the data accuracy and interpretability.

Although the degrading effect of oxygen loss on the electrochemical performance is widely known, quantitively correlating the structural degradation with the fade of electrochemical performance remains as a major challenge. A major reason is that many forms of degradations are generated and convoluted upon the electrochemical cycling. Among the leading challenges is the ability to disentangle these entangled degradations via *in-situ* approaches to trace the complex processes of oxygen evolution under *operando* conditions. For instance, since that O^{2-} anions make up an FCC lattice that is the fundamental framework for the layered phase,[135,399,400] tracking the evolution of the oxygen framework with *in-situ* methods will provide key information for understanding the

driving forces for the crystal structural degradations. For explaining the whole degrading process, it is insufficient to just correlate a single degrading phenomenon with the fading electrochemistry, such as the amount of the oxygen released upon cycling. Comprehensive simulations of the degrading process in Li-ion batteries using physics-based modeling software may be one of the solutions,[401–404] provided that the results from *ex-situ* and *operando* experiments can be properly formulated and adopted by the simulation.

Another question is what leaves behind when the O^{2-} anions leave the cathode. For now, we know that oxygen vacancies are generated in the O^{2-} framework. However, it is largely unclear how the vacancies evolve in the cathode. This question can be further related to the thermal stability of the vacancy-containing cathode and the dynamic evolution behavior of anion vacancies. For the thermal stability, it has been demonstrated [93,207] that a high concentration of oxygen vacancies in the $R\bar{3}m$ lattice reduces the energy barrier for the phase transformation towards the $Fm\bar{3}m$ rock-salt configuration by increasing the mobility of TM cations. This means that the layered phase becomes more unstable and the accumulation of a large amount of oxygen vacancies accelerates the structural degradations in the cathode. For the kinetic evolution of anion vacancies, research has shown that a high concentration of oxygen vacancies can merge into cavities of namometers.[90,91,221] Also, a high concentration of oxygen vacancies in local regions can lead to local transformation towards the rock-salt phase[208,250,405]. It remains unknown whether other structural defects, such as cracks, are also related to the evolution of vacancies. It has been shown that oxygen vacancies are generated to accompany the cracking process,[237] but it is undetermined whether the cracks are formed

via the activity of vacancies. The answer to this question is critical in untwisting the complex structural degradations in layered cathode.

Acknowledgement

This work was supported as part of the NorthEast Center for Chemical Energy Storage (NECCES), an Energy Frontier Research Center funded by the U.S. Department of Energy, Office of Science, Basic Energy Sciences under Award # DE-SC0012583.

Glossary

ABF	Annular Bright Field
ALD	Atomic Layer Deposition
CVD	Chemical Layer Deposition
DEMS	Differential Electrochemical Mass Spectroscopy
DFT	Density Functional Theory
DMC	Dimethyl Carbonate
DSC	Differential scanning calorimetry
EC	Ethylene Carbonate
EDS	Energy Dispersive Spectroscopy
EELS	Electron Energy Loss Spectroscopy
EMC	Ethyl Methyl Carbonate
EPMA	Electron Probe Microanalysis
FIB	Focused Ion Beam
HAADF	High Angle Annular Dark Field

IRS	Infrared Spectroscopy
LMR	Lithium-Manganese Rich (Layered Transition Metal Oxides)
MD	Molecular Dynamics
MS	Mass Spectroscopy
NCA	$LiNi_{0.80}Co_{0.15}Al_{0.05}O_2$
NMC	$LiNi_{1-x-y}Mn_xCo_yO_2$
RDF	Radial Distribution Function
RIXS	Resonant Inelastic X-Ray Scattering
RT	Room Temperature
SEI	Solid Electrolyte Interface
SEM	Scanning Electron Microscopy
SOC	State of Charge
STEM	Scanning Transmission Electron Microscopy
TEM	Transmission Electron Microscopy
TM	Transition Metal
XAS	X-ray Absorption Spectroscopy
XPS	X-ray Photoelectron Spectroscopy

References:

(1) Ritchie, A.; Howard, W. Recent Developments and Likely Advances in Lithium-Ion Batteries. *J. Power Sources* **2006**, *162*, 809–812.

(2) Scrosati, B. Power Sources for Portable Electronics and Hybrid Cars: Lithium Batteries and Fuel Cells. *Chem. Rec.* **2005**, *5*, 286–297.

(3) Sato, N. Thermal Behavior Analysis of Lithium-Ion Batteries for Electric and Hybrid Vehicles. *J. Power Sources* **2001**, *99*, 70–77.

(4) Lu, L.; Han, X.; Li, J.; Hua, J.; Ouyang, M. A Review on the Key Issues for Lithium-Ion Battery Management in Electric Vehicles. *J. Power Sources* **2013**, *226*, 272–288.

(5) Zeng, X.; Li, M.; Abd El-Hady, D.; Alshitari, W.; Al-Bogami, A. S.; Lu, J.; Amine, K.

Commercialization of Lithium Battery Technologies for Electric Vehicles. *Adv. Energy Mater.* **2019**, *9*, 1900161.

(6) Myung, S.-T.; Maglia, F.; Park, K.-J.; Yoon, C. S.; Lamp, P.; Kim, S.-J.; Sun, Y.-K. Nickel-Rich Layered Cathode Materials for Automotive Lithium-Ion Batteries: Achievements and Perspectives. *ACS Energy Lett.* **2017**, *2*, 196–223.

(7) Whittingham, M. S. Lithium Batteries and Cathode Materials. *Chem. Rev.* **2004**, *104*, 4271–4302.

(8) Whittingham, M. S. Ultimate Limits to Intercalation Reactions for Lithium Batteries. *Chem. Rev.* **2014**, *114*, 11414–11443.

(9) Peterson, S. B.; Apt, J.; Whitacre, J. F. Lithium-Ion Battery Cell Degradation Resulting from Realistic Vehicle and Vehicle-to-Grid Utilization. *J. Power Sources* **2010**, *195*, 2385–2392.

(10) Sun, F.; Hu, X.; Zou, Y.; Li, S. Adaptive Unscented Kalman Filtering for State of Charge Estimation of a Lithium-Ion Battery for Electric Vehicles. *Energy* **2011**, *36*, 3531–3540.

(11) Armand, M.; Tarascon, J.-M. Building Better Batteries. *Nature* **2008**, *451*, 652.

(12) Richa, K.; Babbitt, C. W.; Gaustad, G.; Wang, X. A Future Perspective on Lithium-Ion Battery Waste Flows from Electric Vehicles. *Resour. Conserv. Recycl.* **2014**, *83*, 63–76.

(13) Zubi, G.; Dufo-López, R.; Carvalho, M.; Pasaoglu, G. The Lithium-Ion Battery: State of the Art and Future Perspectives. *Renew. Sustain. Energy Rev.* **2018**, *89*, 292–308.

(14) Stephan, A. K. The Age of Li-Ion Batteries. *Joule* **2019**, *3*, 2583–2584.

(15) Mohanty, D.; Huq, A.; Payzant, E. A.; Sefat, A. S.; Li, J.; Abraham, D. P.; Wood III, D. L.; Daniel, C. Neutron Diffraction and Magnetic Susceptibility Studies on a High-Voltage Li1. 2Mn0. 55Ni0. 15Co0. 10O2 Lithium Ion Battery Cathode: Insight into the Crystal Structure. *Chem. Mater.* **2013**, *25*, 4064–4070.

(16) Manthiram, A.; Chemelewski, K.; Lee, E.-S. A Perspective on the High-Voltage LiMn 1.5 Ni 0.5 O 4 Spinel Cathode for Lithium-Ion Batteries. *Energy Environ. Sci.* **2014**, *7*, 1339–1350.

(17) Amine, K.; Chen, Z.; Zhang, Z.; Liu, J.; Lu, W.; Qin, Y.; Lu, J.; Curtis, L.; Sun, Y.-K. Mechanism of Capacity Fade of MCMB/Li 1.1 [Ni 1/3 Mn 1/3 Co 1/3] 0.9 O 2 Cell at Elevated Temperature and Additives to Improve Its Cycle Life. *J. Mater. Chem.* **2011**, *21*, 17754–17759.

(18) Genevois, C.; Koga, H.; Croguennec, L.; Ménétrier, M.; Delmas, C.; Weill, F. Insight into the Atomic Structure of Cycled Lithium-Rich Layered Oxide Li1. 20Mn0. 54Co0. 13Ni0. 13O2 Using HAADF STEM and Electron Nanodiffraction. *J. Phys. Chem. C* **2014**, *119*, 75–83.

(19) Liu, Z.; Cronin, J. S.; Yu-chen, K.; Wilson, J. R.; Yakal-Kremski, K. J.; Wang, J.; Faber, K. T.; Barnett, S. A. Three-Dimensional Morphological Measurements of LiCoO2 and LiCoO2/Li (Ni1/3Mn1/3Co1/3) O2 Lithium-Ion Battery Cathodes. *J. Power Sources* **2013**,

227, 267–274.

(20) Manthiram, A.; Kim, J. Low Temperature Synthesis of Insertion Oxides for Lithium Batteries. *Chem. Mater.* **1998**, *10*, 2895–2909.

(21) Grey, C. P.; Tarascon, J. M. Sustainability and in Situ Monitoring in Battery Development. *Nat. Mater.* **2017**, *16*, 45.

(22) Hausbrand, R.; Cherkashinin, G.; Ehrenberg, H.; Gröting, M.; Albe, K.; Hess, C.; Jaegermann, W. Fundamental Degradation Mechanisms of Layered Oxide Li-Ion Battery Cathode Materials: Methodology, Insights and Novel Approaches. *Mater. Sci. Eng. B* **2015**, *192*, 3–25.

(23) Ma, M.; Chernova, N. A.; Toby, B. H.; Zavalij, P. Y.; Whittingham, M. S. Structural and Electrochemical Behavior of LiMn0. 4Ni0. 4Co0. 2O2. *J. Power Sources* **2007**, *165*, 517–534.

(24) Sathiya, M.; Abakumov, A. M.; Foix, D.; Rousse, G.; Ramesha, K.; Saubanère, M.; Doublet, M. L.; Vezin, H.; Laisa, C. P.; Prakash, A. S. Origin of Voltage Decay in High-Capacity Layered Oxide Electrodes. *Nat. Mater.* **2015**, *14*, 230.

(25) Lim, B.-B.; Myung, S.-T.; Yoon, C. S.; Sun, Y.-K. Comparative Study of Ni-Rich Layered Cathodes for Rechargeable Lithium Batteries: Li [Ni0. 85Co0. 11Al0. 04] O2 and Li [Ni0. 84Co0. 06Mn0. 09Al0. 01] O2 with Two-Step Full Concentration Gradients. *ACS energy Lett.* **2016**, *1*, 283–289.

(26) Taracson, J. M.; Armand, M. Issues and Challenges Facing Lithium Ion Batteries. *Nature* **2001**, *414*, 359–367.

(27) Itou, Y.; Ukyo, Y. Performance of LiNiCoO2 Materials for Advanced Lithium-Ion Batteries. *J. Power Sources* **2005**, *146*, 39–44.

(28) Boulineau, A.; Simonin, L.; Colin, J.-F.; Bourbon, C.; Patoux, S. First Evidence of Manganese–Nickel Segregation and Densification upon Cycling in Li-Rich Layered Oxides for Lithium Batteries. *Nano Lett.* **2013**, *13*, 3857–3863.

(29) Vetter, J.; Novák, P.; Wagner, M. R.; Veit, C.; Möller, K.-C.; Besenhard, J. O.; Winter, M.; Wohlfahrt-Mehrens, M.; Vogler, C.; Hammouche, A. Ageing Mechanisms in Lithium-Ion Batteries. *J. Power Sources* **2005**, *147*, 269–281.

(30) Aurbach, D. Review of Selected Electrode–Solution Interactions Which Determine the Performance of Li and Li Ion Batteries. *J. Power Sources* **2000**, *89*, 206–218.

(31) Li, W.; Liu, X.; Celio, H.; Smith, P.; Dolocan, A.; Chi, M.; Manthiram, A. Mn versus Al in Layered Oxide Cathodes in Lithium-Ion Batteries: A Comprehensive Evaluation on Long-Term Cyclability. *Adv. Energy Mater.* **2018**, *8*, 1703154.

(32) Jarvis, K. A.; Deng, Z.; Allard, L. F.; Manthiram, A.; Ferreira, P. J. Understanding Structural Defects in Lithium-Rich Layered Oxide Cathodes. *J. Mater. Chem.* **2012**, *22*, 11550–11555.

(33) Hoang, K. Defect Physics, Delithiation Mechanism, and Electronic and Ionic Conduction in

Layered Lithium Manganese Oxide Cathode Materials. *Phys. Rev. Appl.* **2015**, *3*, 24013.

(34) Fu, C.; Li, G.; Luo, D.; Li, Q.; Fan, J.; Li, L. Nickel-Rich Layered Microspheres Cathodes: Lithium/Nickel Disordering and Electrochemical Performance. *ACS Appl. Mater. Interfaces* **2014**, *6*, 15822–15831.

(35) Ryu, H.-H.; Park, K.-J.; Yoon, C. S.; Sun, Y.-K. Capacity Fading of Ni-Rich Li [Ni x Co y Mn1–x–y] O2 (0.6≤ X≤ 0.95) Cathodes for High-Energy-Density Lithium-Ion Batteries: Bulk or Surface Degradation? *Chem. Mater.* **2018**, *30*, 1155–1163.

(36) Zheng, J. M.; Wu, X. B.; Yang, Y. A Comparison of Preparation Method on the Electrochemical Performance of Cathode Material Li [Li0. 2Mn0. 54Ni0. 13Co0. 13] O2 for Lithium Ion Battery. *Electrochim. Acta* **2011**, *56*, 3071–3078.

(37) Nayak, P. K.; Erickson, E. M.; Schipper, F.; Penki, T. R.; Munichandraiah, N.; Adelhelm, P.; Sclar, H.; Amalraj, F.; Markovsky, B.; Aurbach, D. Review on Challenges and Recent Advances in the Electrochemical Performance of High Capacity Li-and Mn-rich Cathode Materials for Li-ion Batteries. *Adv. Energy Mater.* **2018**, *8*, 1702397.

(38) Armstrong, A. R.; Holzapfel, M.; Novák, P.; Johnson, C. S.; Kang, S.-H.; Thackeray, M. M.; Bruce, P. G. Demonstrating Oxygen Loss and Associated Structural Reorganization in the Lithium Battery Cathode Li [Ni0. 2Li0. 2Mn0. 6] O2. *J. Am. Chem. Soc.* **2006**, *128*, 8694–8698.

(39) McCalla, E.; Abakumov, A. M.; Saubanère, M.; Foix, D.; Berg, E. J.; Rousse, G.; Doublet, M.-L.; Gonbeau, D.; Novák, P.; Van Tendeloo, G. Visualization of OO Peroxo-like Dimers in High-Capacity Layered Oxides for Li-Ion Batteries. *Science (80-.).* **2015**, *350*, 1516–1521.

(40) Manthiram, A.; Choi, W. Suppression of Mn Dissolution in Spinel Cathodes by Trapping the Protons within Layered Oxide Cathodes. *Electrochem. solid-state Lett.* **2007**, *10*, A228–A231.

(41) Alcantara, R.; Lavela, P.; Tirado, J. L.; Zhecheva, E.; Stoyanova, R. Recent Advances in the Study of Layered Lithium Transition Metal Oxides and Their Application as Intercalation Electrodes. *J. Solid State Electrochem.* **1999**, *3*, 121–134.

(42) Ménétrier, M.; Saadoune, I.; Levasseur, S.; Delmas, C. The Insulator-Metal Transition upon Lithium Deintercalation from LiCoO2: Electronic Properties and 7Li NMR Study. *J. Mater. Chem.* **1999**, *9*, 1135–1140.

(43) Gallagher, K. G.; Croy, J. R.; Balasubramanian, M.; Bettge, M.; Abraham, D. P.; Burrell, A. K.; Thackeray, M. M. Correlating Hysteresis and Voltage Fade in Lithium-and Manganese-Rich Layered Transition-Metal Oxide Electrodes. *Electrochem. commun.* **2013**, *33*, 96–98.

(44) Mohanty, D.; Sefat, A. S.; Kalnaus, S.; Li, J.; Meisner, R. A.; Payzant, E. A.; Abraham, D. P.; Wood, D. L.; Daniel, C. Investigating Phase Transformation in the Li 1.2 Co 0.1 Mn 0.55 Ni 0.15 O 2 Lithium-Ion Battery Cathode during High-Voltage Hold (4.5 V) via Magnetic, X-Ray Diffraction and Electron Microscopy Studies. *J. Mater. Chem. A* **2013**, *1*, 6249–6261.

(45) Liu, H.; Wolf, M.; Karki, K.; Yu, Y.-S.; Stach, E. A.; Cabana, J.; Chapman, K. W.; Chupas, P. J. Intergranular Cracking as a Major Cause of Long-Term Capacity Fading of Layered Cathodes. *Nano Lett.* **2017**, *17*, 3452–3457.

(46) Min, K.; Cho, E. Intrinsic Origin of Intra-Granular Cracking in Ni-Rich Layered Oxide Cathode Materials. *Phys. Chem. Chem. Phys.* **2018**, *20*, 9045–9052.

(47) Liu, G.; Li, M.; Wu, N.; Cui, L.; Huang, X.; Liu, X.; Zhao, Y.; Chen, H.; Yuan, W.; Bai, Y. Single-Crystalline Particles: An Effective Way to Ameliorate the Intragranular Cracking, Thermal Stability, and Capacity Fading of the LiNi0. 6Co0. 2Mn0. 2O2 Electrodes. *J. Electrochem. Soc.* **2018**, *165*, A3040–A3047.

(48) Hwang, S.; Chang, W.; Kim, S. M.; Su, D.; Kim, D. H.; Lee, J. Y.; Chung, K. Y.; Stach, E. A. Investigation of Changes in the Surface Structure of Li x Ni0. 8Co0. 15Al0. 05O2 Cathode Materials Induced by the Initial Charge. *Chem. Mater.* **2014**, *26*, 1084–1092.

(49) Hu, E.; Yu, X.; Lin, R.; Bi, X.; Lu, J.; Bak, S.; Nam, K.-W.; Xin, H. L.; Jaye, C.; Fischer, D. A. Evolution of Redox Couples in Li-and Mn-Rich Cathode Materials and Mitigation of Voltage Fade by Reducing Oxygen Release. *Nat. Energy* **2018**, *3*, 690.

(50) Hong, J.; Lim, H.-D.; Lee, M.; Kim, S.-W.; Kim, H.; Oh, S.-T.; Chung, G.-C.; Kang, K. Critical Role of Oxygen Evolved from Layered Li–Excess Metal Oxides in Lithium Rechargeable Batteries. *Chem. Mater.* **2012**, *24*, 2692–2697.

(51) Chen, R.; Ren, S.; Knapp, M.; Wang, D.; Witter, R.; Fichtner, M.; Hahn, H. Disordered Lithium-Rich Oxyfluoride as a Stable Host for Enhanced Li+ Intercalation Storage. *Adv. Energy Mater.* **2015**, *5*, 1401814.

(52) Dou, S. Review and Prospect of Layered Lithium Nickel Manganese Oxide as Cathode Materials for Li-Ion Batteries. *J. Solid State Electrochem.* **2013**, *17*, 911–926.

(53) Pang, S.; Zhu, M.; Xu, K.; Shen, X.; Wen, H.; Su, Y.; Yang, G.; Wu, X.; Li, S.; Wang, W. Enhanced Electrochemical Performance of Li1. 2Mn0. 54Ni0. 13Co0. 13O2 via L-Ascorbic Acid-Based Treatment as Cathode Material for Li-Ion Batteries. *J. Electrochem. Soc.* **2018**, *165*, A1897–A1902.

(54) Faenza, N. V; Lebens-Higgins, Z. W.; Mukherjee, P.; Sallis, S.; Pereira, N.; Badway, F.; Halajko, A.; Ceder, G.; Cosandey, F.; Piper, L. F. J. Electrolyte Induced Surface Transformation and Transition Metal Dissolution of Fully Delithiated.

(55) Nam, K.; Bak, S.; Hu, E.; Yu, X.; Zhou, Y.; Wang, X.; Wu, L.; Zhu, Y.; Chung, K.; Yang, X. Combining in Situ Synchrotron X-ray Diffraction and Absorption Techniques with Transmission Electron Microscopy to Study the Origin of Thermal Instability in Overcharged Cathode Materials for Lithium-ion Batteries. *Adv. Funct. Mater.* **2013**, *23*, 1047–1063.

(56) Fell, C. R.; Carroll, K. J.; Chi, M.; Meng, Y. S. Synthesis–Structure–Property Relations in Layered,"Li-Excess" Oxides Electrode Materials Li [Li1/3− 2x/3NixMn2/3− x/3] O2 (X= 1/3, 1/4, and 1/5). *J. Electrochem. Soc.* **2010**, *157*, A1202–A1211.

(57) Sathiya, M.; Rousse, G.; Ramesha, K.; Laisa, C. P.; Vezin, H.; Sougrati, M. T.; Doublet,

M.-L.; Foix, D.; Gonbeau, D.; Walker, W. Reversible Anionic Redox Chemistry in High-Capacity Layered-Oxide Electrodes. *Nat. Mater.* **2013**, *12*, 827.

(58) Sharifi-Asl, S.; Lu, J.; Amine, K.; Shahbazian-Yassar, R. Oxygen Release Degradation in Li-Ion Battery Cathode Materials: Mechanisms and Mitigating Approaches. *Adv. Energy Mater.* **2019**, *9*, 1900551.

(59) Ong, S. P.; Chevrier, V. L.; Hautier, G.; Jain, A.; Moore, C.; Kim, S.; Ma, X.; Ceder, G. Voltage, Stability and Diffusion Barrier Differences between Sodium-Ion and Lithium-Ion Intercalation Materials. *Energy Environ. Sci.* **2011**, *4*, 3680–3688.

(60) Hong, J.; Seo, D.-H.; Kim, S.-W.; Gwon, H.; Oh, S.-T.; Kang, K. Structural Evolution of Layered Li 1.2 Ni 0.2 Mn 0.6 O 2 upon Electrochemical Cycling in a Li Rechargeable Battery. *J. Mater. Chem.* **2010**, *20*, 10179–10186.

(61) Manthiram, A.; Song, B.; Li, W. A Perspective on Nickel-Rich Layered Oxide Cathodes for Lithium-Ion Batteries. *Energy Storage Mater.* **2017**, *6*, 125–139.

(62) Xu, J.; Sun, M.; Qiao, R.; Renfrew, S. E.; Ma, L.; Wu, T.; Hwang, S.; Nordlund, D.; Su, D.; Amine, K. Elucidating Anionic Oxygen Activity in Lithium-Rich Layered Oxides. *Nat. Commun.* **2018**, *9*, 1–10.

(63) Xiang, X.; Knight, J. C.; Li, W.; Manthiram, A. Understanding the Effect of Co3+ Substitution on the Electrochemical Properties of Lithium-Rich Layered Oxide Cathodes for Lithium-Ion Batteries. *J. Phys. Chem. C* **2014**, *118*, 21826–21833.

(64) Gu, L.; Xiao, D.; Hu, Y.-S.; Li, H.; Ikuhara, Y. Atomic-Scale Structure Evolution in a Quasi-Equilibrated Electrochemical Process of Electrode Materials for Rechargeable Batteries. *Adv. Mater.* **2015**, *27*, 2134–2149.

(65) Liu, X.; Gu, L. Advanced Transmission Electron Microscopy for Electrode and Solid-Electrolyte Materials in Lithium-Ion Batteries. *Small Methods* **2018**, *2*, 1800006.

(66) Lin, F.; Nordlund, D.; Markus, I. M.; Weng, T.-C.; Xin, H. L.; Doeff, M. M. Profiling the Nanoscale Gradient in Stoichiometric Layered Cathode Particles for Lithium-Ion Batteries. *Energy Environ. Sci.* **2014**, *7*, 3077–3085.

(67) Xu, B.; Fell, C. R.; Chi, M.; Meng, Y. S. Identifying Surface Structural Changes in Layered Li-Excess Nickel Manganese Oxides in High Voltage Lithium Ion Batteries: A Joint Experimental and Theoretical Study. *Energy Environ. Sci.* **2011**, *4*, 2223–2233.

(68) Kikkawa, J.; Akita, T.; Hosono, E.; Zhou, H.; Kohyama, M. Atomic and Electronic Structures of Li0. 44MnO2 Nanowires and Li2MnO3 Byproducts in the Formation Process of LiMn2O4 Nanowires. *J. Phys. Chem. C* **2010**, *114*, 18358–18365.

(69) Zhang, H.; May, B.; Serrano-Sevillano, J.; Casas-Cabanas, M.; Cabana, J.; Wang, C.; Zhou, G. Facet-Dependent Rock-Salt Reconstruction on the Surface of Layered Oxide Cathodes. *Chem. Mater. 30*, 692–699.

(70) Watanabe, S.; Kinoshita, M.; Hosokawa, T.; Morigaki, K.; Nakura, K. Capacity Fade of LiAlyNi1− X− YCoxO2 Cathode for Lithium-Ion Batteries during Accelerated Calendar and Cycle Life Tests (Surface Analysis of LiAlyNi1− X− YCoxO2 Cathode after Cycle Tests in

Restricted Depth of Discharge Ranges). *J. Power Sources* **2014**, *258*, 210–217.

(71) Sallis, S.; Pereira, N.; Mukherjee, P.; Quackenbush, N. F.; Faenza, N.; Schlueter, C.; Lee, T.-L.; Yang, W. L.; Cosandey, F.; Amatucci, G. G. Surface Degradation of Li1–x Ni0. 80Co0. 15Al0. 05O2 Cathodes: Correlating Charge Transfer Impedance with Surface Phase Transformations. *Appl. Phys. Lett.* **2016**, *108*, 263902.

(72) Li, J.; Wang, L.; Zhang, Q.; He, X. Synthesis and Characterization of LiNi0. 6Mn0. 4− XCoxO2 as Cathode Materials for Li-Ion Batteries. *J. Power Sources* **2009**, *189*, 28–33.

(73) Yang, F.; Liu, Y.; Martha, S. K.; Wu, Z.; Andrews, J. C.; Ice, G. E.; Pianetta, P.; Nanda, J. Nanoscale Morphological and Chemical Changes of High Voltage Lithium–Manganese Rich NMC Composite Cathodes with Cycling. *Nano Lett.* **2014**, *14*, 4334–4341.

(74) Lin, F.; Nordlund, D.; Li, Y.; Quan, M. K.; Cheng, L.; Weng, T.-C.; Liu, Y.; Xin, H. L.; Doeff, M. M. Metal Segregation in Hierarchically Structured Cathode Materials for High-Energy Lithium Batteries. *Nat. Energy* **2016**, *1*, 15004.

(75) Thibault, P.; Dierolf, M.; Menzel, A.; Bunk, O.; David, C.; Pfeiffer, F. High-Resolution Scanning x-Ray Diffraction Microscopy. *Science (80-.).* **2008**, *321*, 379–382.

(76) Chao, W.; Harteneck, B. D.; Liddle, J. A.; Anderson, E. H.; Attwood, D. T. Soft X-Ray Microscopy at a Spatial Resolution Better than 15 Nm. *Nature* **2005**, *435*, 1210.

(77) Ade, H.; Zhang, X.; Cameron, S.; Costello, C.; Kirz, J.; Williams, S. Chemical Contrast in X-Ray Microscopy and Spatially Resolved XANES Spectroscopy of Organic Specimens. *Science (80-.).* **1992**, *258*, 972–975.

(78) Jacobsen, C.; Williams, S.; Anderson, E.; Browne, M. T.; Buckley, C. J.; Kern, D.; Kirz, J.; Rivers, M.; Zhang, X. Diffraction-Limited Imaging in a Scanning Transmission x-Ray Microscope. *Opt. Commun.* **1991**, *86*, 351–364.

(79) Lin, F.; Markus, I. M.; Nordlund, D.; Weng, T.-C.; Asta, M. D.; Xin, H. L.; Doeff, M. M. Surface Reconstruction and Chemical Evolution of Stoichiometric Layered Cathode Materials for Lithium-Ion Batteries. *Nat. Commun.* **2014**, *5*, 3529.

(80) Arunkumar, T. A.; Wu, Y.; Manthiram, A. Factors Influencing the Irreversible Oxygen Loss and Reversible Capacity in Layered Li [Li1/3Mn2/3] O2− Li [M] O2 (M= Mn0. 5-y Ni0. 5-y Co2 y and Ni1-y Co y) Solid Solutions. *Chem. Mater.* **2007**, *19*, 3067–3073.

(81) Abraham, D. P.; Twesten, R. D.; Balasubramanian, M.; Petrov, I.; McBreen, J.; Amine, K. Surface Changes on LiNi0. 8Co0. 2O2 Particles during Testing of High-Power Lithium-Ion Cells. *Electrochem. commun.* **2002**, *4*, 620–625.

(82) Materlik, G.; Rayment, T.; Stuart, D. I. Diamond Light Source: Status and Perspectives. *Philos. Trans. R. Soc. A Math. Phys. Eng. Sci.* **2015**, *373*, 20130161.

(83) Findlay, S. D.; Shibata, N.; Ikuhara, Y.; Huang, R.; Okunishi, E.; Sawada, H.; Kohno, Y.; Kondo, Y. Annular Bright-Field Scanning Transmission Electron Microscopy: Direct and Robust Atomic-Resolution Imaging of Light Elements in Crystalline Materials. *Micros. Today* **2017**, *25*, 36–41.

(84) Sun, M.; Yu, H.; Dong, X.; Xia, L.; Yang, Y. Sedum Lineare Flower-like Ordered Mesoporous In2O3/ZnO Gas Sensing Materials with High Sensitive Response to H2S at Room Temperature Prepared by Self-Assembled of 2D Nanosheets. *J. Alloys Compd.* **2020**, 156170.

(85) Li, Y.; Zakharov, D.; Zhao, S.; Tappero, R.; Jung, U.; Elsen, A.; Baumann, P.; Nuzzo, R. G.; Stach, E. A.; Frenkel, A. I. Complex Structural Dynamics of Nanocatalysts Revealed in Operando Conditions by Correlated Imaging and Spectroscopy Probes. *Nat. Commun.* **2015**, *6*, 7583.

(86) Strehle, B.; Kleiner, K.; Jung, R.; Chesneau, F.; Mendez, M.; Gasteiger, H. A.; Piana, M. The Role of Oxygen Release from Li- and Mn-Rich Layered Oxides during the First Cycles Investigated by On-Line Electrochemical Mass Spectrometry. *J. Electrochem. Soc.* **2017**, *164*, A400–A406.

(87) Shen, S.; Hong, Y.; Zhu, F.; Cao, Z.; Li, Y.; Ke, F.; Fan, J.; Zhou, L.; Wu, L.; Dai, P.; Cai, M.; Huang, L.; Zhou, Z.; Li, J.; Wu, Q.; Sun, S. Tuning Electrochemical Properties of Li-Rich Layered Oxide Cathodes by Adjusting Co/Ni Ratios and Mechanism Investigation Using in Situ X-Ray Diffraction and Online Continuous Flow Differential Electrochemical Mass Spectrometry. *ACS Appl. Mater. Interfaces* **2018**, *10*, 12666–12677.

(88) Bettge, M.; Li, Y.; Gallagher, K.; Zhu, Y.; Wu, Q.; Lu, W.; Bloom, I.; Abraham, D. P. Voltage Fade of Layered Oxides: Its Measurement and Impact on Energy Density. *J. Electrochem. Soc.* **2013**, *160*, A2046–A2055.

(89) Sun, Y.; Cong, H.; Zan, L.; Zhang, Y. Oxygen Vacancies and Stacking Faults Introduced by Low-Temperature Reduction Improve the Electrochemical Properties of Li2MnO3 Nanobelts as Lithium-Ion Battery Cathodes. *ACS Appl. Mater. Interfaces* **2017**, *9*, 38545–38555.

(90) Yan, P.; Zheng, J.; Tang, Z.-K.; Devaraj, A.; Chen, G.; Amine, K.; Zhang, J.-G.; Liu, L.-M.; Wang, C. Injection of Oxygen Vacancies in the Bulk Lattice of Layered Cathodes. *Nat. Nanotechnol.* **2019**, *14*, 602–608.

(91) Zhang, H.; May, B. M.; Omenya, F.; Whittingham, M. S.; Cabana, J.; Zhou, G. Layered Oxide Cathodes for Li-Ion Batteries: Oxygen Loss and Vacancy Evolution. *Chem. Mater.* **2019**, *31*, 7790–7798.

(92) Lin, F.; Liu, Y.; Yu, X.; Cheng, L.; Singer, A.; Shpyrko, O. G.; Xin, H. L.; Tamura, N.; Tian, C.; Weng, T.-C.; Yang, X.-Q.; Meng, Y. S.; Nordlund, D.; Yang, W.; Doeff, M. M. Synchrotron X-Ray Analytical Techniques for Studying Materials Electrochemistry in Rechargeable Batteries. *Chem. Rev.* **2017**, *117*, 13123–13186.

(93) Qiu, B.; Zhang, M.; Wu, L.; Wang, J.; Xia, Y.; Qian, D.; Liu, H.; Hy, S.; Chen, Y.; An, K. Gas–Solid Interfacial Modification of Oxygen Activity in Layered Oxide Cathodes for Lithium-Ion Batteries. *Nat. Commun.* **2016**, *7*, 1–10.

(94) Hekmatfar, M.; Kazzazi, A.; Eshetu, G. G.; Hasa, I.; Passerini, S. Understanding the Electrode/Electrolyte Interface Layer on the Li-Rich Nickel Manganese Cobalt Layered Oxide Cathode by XPS. *ACS Appl. Mater. Interfaces* **2019**, *11*, 43166–43179.

(95) Liu, H.; Kazemiabnavi, S.; Grenier, A.; Vaughan, G.; Di Michiel, M.; Polzin, B. J.; Thornton, K.; Chapman, K. W.; Chupas, P. J. Quantifying Reaction and Rate Heterogeneity in Battery Electrodes in 3D through Operando X-Ray Diffraction Computed Tomography. *ACS Appl. Mater. Interfaces* **2019**, *11*, 18386–18394.

(96) Liu, H.; Li, Z.; Grenier, A.; Kamm, G. E.; Yin, L.; Mattei, G. S.; Cosby, M. R.; Khalifah, P. G.; Chupas, P. J.; Chapman, K. W. Best Practices for Operando Depth-Resolving Battery Experiments. *J. Appl. Crystallogr.* **2020**, *53*, 133–139.

(97) Goodenough, J. B.; Kim, Y.; B. Goodenough, J.; Kim, Y. Challenges for Rechargeable Li Batteries. *Chem. Mater.* **2010**, *22*, 587–603.

(98) Xu, J.; Lin, F.; Doeff, M. M.; Tong, W. A Review of Ni-Based Layered Oxides for Rechargeable Li-Ion Batteries. *J. Mater. Chem. A* **2017**, *5*, 874–901.

(99) Hy, S.; Liu, H.; Zhang, M.; Qian, D.; Hwang, B.-J.; Meng, Y. S. Performance and Design Considerations for Lithium Excess Layered Oxide Positive Electrode Materials for Lithium Ion Batteries. *Energy Environ. Sci.* **2016**, *9*, 1931–1954.

(100) Chakraborty, A.; Kunnikuruvan, S.; Kumar, S.; Markovsky, B.; Aurbach, D.; Dixit, M.; Major, D. T. Layered Cathode Materials for Lithium-Ion Batteries: Review of Computational Studies on LiNi1–x–YCoxMnyO2 and LiNi1–x–YCoxAlyO2. *Chem. Mater.* **2020**, *32*, 915–952.

(101) Manthiram, A.; Murugan, A. V.; Sarkar, A.; Muraliganth, T. Nanostructured Electrode Materials for Electrochemical Energy Storage and Conversion. *Energy Environ. Sci.* **2008**, *1*, 621–638.

(102) Zhang, H.; Omenya, F.; Whittingham, M. S.; Wang, C.; Zhou, G. Formation of an Anti-Core–Shell Structure in Layered Oxide Cathodes for Li-Ion Batteries. *ACS Energy Lett.* **2017**, *2*, 2598–2606.

(103) Zhang, H.; Omenya, F.; Yan, P.; Luo, L.; Whittingham, M. S.; Wang, C.; Zhou, G. Rock-Salt Growth-Induced (003) Cracking in a Layered Positive Electrode for Li-Ion Batteries. *ACS Energy Lett. 2*, 2607–2615.

(104) Luo, J.-Y.; Cui, W.-J.; He, P.; Xia, Y.-Y. Raising the Cycling Stability of Aqueous Lithium-Ion Batteries by Eliminating Oxygen in the Electrolyte. *Nat. Chem.* **2010**, *2*, 760–765.

(105) Klein, S.; Bärmann, P.; Beuse, T.; Borzutzki, K.; Frerichs, J. E.; Kasnatscheew, J.; Winter, M.; Placke, T. Exploiting the Degradation Mechanism of NCM523 ‖ Graphite Lithium-Ion Full Cells Operated at High Voltage. *ChemSusChem* **2021**, *14*, 595–613.

(106) Wang, Q.; Ping, P.; Zhao, X.; Chu, G.; Sun, J.; Chen, C. Thermal Runaway Caused Fire and Explosion of Lithium Ion Battery. *J. Power Sources* **2012**, *208*, 210–224.

(107) Fu, Y.; Lu, S.; Li, K.; Liu, C.; Cheng, X.; Zhang, H. An Experimental Study on Burning Behaviors of 18650 Lithium Ion Batteries Using a Cone Calorimeter. *J. Power Sources* **2015**, *273*, 216–222.

(108) Wang, Q.; Sun, J.; Chu, G. Lithium Ion Battery Fire and Explosion. *Fire Saf. Sci.* **2005**, *8*, 375–382.

(109) Larsson, F.; Bertilsson, S.; Furlani, M.; Albinsson, I.; Mellander, B.-E. Gas Explosions and Thermal Runaways during External Heating Abuse of Commercial Lithium-Ion Graphite-LiCoO2 Cells at Different Levels of Ageing. *J. Power Sources* **2018**, *373*, 220–231.

(110) Doh, C.-H.; Kim, D.-H.; Kim, H.-S.; Shin, H.-M.; Jeong, Y.-D.; Moon, S.-I.; Jin, B.-S.; Eom, S. W.; Kim, H.-S.; Kim, K.-W. Thermal and Electrochemical Behaviour of C/LixCoO2 Cell during Safety Test. *J. Power Sources* **2008**, *175*, 881–885.

(111) Guerfi, A.; Kaneko, M.; Petitclerc, M.; Mori, M.; Zaghib, K. LiFePO4 Water-Soluble Binder Electrode for Li-Ion Batteries. *J. Power Sources* **2007**, *163*, 1047–1052.

(112) Wei, Z.; Xue, L.; Nie, F.; Sheng, J.; Shi, Q.; Zhao, X. Study of Sulfonated Polyether Ether Ketone with Pendant Lithiated Fluorinated Sulfonic Groups as Ion Conductive Binder in Lithium-Ion Batteries. *J. Power Sources* **2014**, *256*, 28–31.

(113) Fransson, L.; Eriksson, T.; Edström, K.; Gustafsson, T.; Thomas, J. O. Influence of Carbon Black and Binder on Li-Ion Batteries. *J. Power Sources* **2001**, *101*, 1–9.

(114) Lee, B.-S.; Wu, Z.; Petrova, V.; Xing, X.; Lim, H.-D.; Liu, H.; Liu, P. Analysis of Rate-Limiting Factors in Thick Electrodes for Electric Vehicle Applications. *J. Electrochem. Soc.* **2018**, *165*, A525–A533.

(115) Li, J.; Zhuang, N.; Xie, J.; Zhu, Y.; Lai, H.; Qin, W.; Javed, M. S.; Xie, W.; Mai, W. Carboxymethyl Cellulose Binder Greatly Stabilizes Porous Hollow Carbon Submicrospheres in Capacitive K-Ion Storage. *ACS Appl. Mater. Interfaces* **2019**, *11*, 15581–15590.

(116) Xu, B.; Qian, D.; Wang, Z.; Meng, Y. S. Recent Progress in Cathode Materials Research for Advanced Lithium Ion Batteries. *Mater. Sci. Eng. R Reports* **2012**, *73*, 51–65.

(117) Lu, Z.; Dahn, J. R. Understanding the Anomalous Capacity of Li/Li [Ni x Li (1/3− 2x/3) Mn (2/3− x/3)] O 2 Cells Using in Situ X-Ray Diffraction and Electrochemical Studies. *J. Electrochem. Soc.* **2002**, *149*, A815–A822.

(118) Chebiam, R. V; Kannan, A. M.; Prado, F.; Manthiram, A. Comparison of the Chemical Stability of the High Energy Density Cathodes of Lithium-Ion Batteries. *Electrochem. commun.* **2001**, *3*, 624–627.

(119) Arora, P.; White, R. E.; Doyle, M. Capacity Fade Mechanisms and Side Reactions in Lithium-ion Batteries. *J. Electrochem. Soc.* **1998**, *145*, 3647–3667.

(120) Baba, Y.; Okada, S.; Yamaki, J. Thermal Stability of LixCoO2 Cathode for Lithium Ion Battery. *Solid State Ionics* **2002**, *148*, 311–316.

(121) Kasnatscheew, J.; Evertz, M.; Streipert, B.; Wagner, R.; Nowak, S.; Cekic Laskovic, I.; Winter, M. Improving Cycle Life of Layered Lithium Transition Metal Oxide (LiMO2) Based Positive Electrodes for Li Ion Batteries by Smart Selection of the Electrochemical Charge Conditions. *J. Power Sources* **2017**, *359*, 458–467.

(122) Koga, H.; Croguennec, L.; Ménétrier, M.; Mannessiez, P.; Weill, F.; Delmas, C.; Belin, S. Operando X-Ray Absorption Study of the Redox Processes Involved upon Cycling of the Li-Rich Layered Oxide Li1.20Mn0.54Co0.13Ni0.13O2 in Li Ion Batteries. *J. Phys. Chem. C* **2014**, *118*, 5700–5709.

(123) Liu, X.; Liu, J.; Huang, T.; Yu, A. CaF2-Coated Li1. 2Mn0. 54Ni0. 13Co0. 13O2 as Cathode Materials for Li-Ion Batteries. *Electrochim. Acta* **2013**, *109*, 52–58.

(124) Saubanère, M.; McCalla, E.; Tarascon, J.-M.; Doublet, M.-L. The Intriguing Question of Anionic Redox in High-Energy Density Cathodes for Li-Ion Batteries. *Energy Environ. Sci.* **2016**, *9*, 984–991.

(125) Thackeray, M. M.; Kang, S.-H.; Johnson, C. S.; Vaughey, J. T.; Benedek, R.; Hackney, S. A. Li2MnO3-Stabilized LiMO2 (M = Mn, Ni, Co) Electrodes for Lithium-Ion Batteries. *J. Mater. Chem.* **2007**, *17*, 3112–3125.

(126) Yu, X.; Lyu, Y.; Gu, L.; Wu, H.; Bak, S.; Zhou, Y.; Amine, K.; Ehrlich, S. N.; Li, H.; Nam, K. Understanding the Rate Capability of High-Energy-Density Li-Rich Layered Li1. 2Ni0. 15Co0. 1Mn0. 55O2 Cathode Materials. *Adv. Energy Mater.* **2014**, *4*, 1300950.

(127) Hy, S.; Felix, F.; Rick, J.; Su, W.-N.; Hwang, B. J. Direct In Situ Observation of Li2O Evolution on Li-Rich High-Capacity Cathode Material, Li[NixLi(1–2x)/3Mn(2–x)/3]O2 (0 ≤ x ≤0.5). *J. Am. Chem. Soc.* **2014**, *136*, 999–1007.

(128) Martha, S. K.; Nanda, J.; Veith, G. M.; Dudney, N. J. Electrochemical and Rate Performance Study of High-Voltage Lithium-Rich Composition: Li1. 2Mn0. 525Ni0. 175Co0. 1O2. *J. Power Sources* **2012**, *199*, 220–226.

(129) Kraytsberg, A.; Ein-Eli, Y. Higher, Stronger, Better… A Review of 5 Volt Cathode Materials for Advanced Lithium-Ion Batteries. *Adv. Energy Mater.* **2012**, *2*, 922–939.

(130) Choi, J.; Manthiram, A. Comparison of the Electrochemical Behaviors of Stoichiometric LiNi1/3Co1/3Mn1/3 O 2 and Lithium Excess Li1. 03 (Ni1/3Co1/3Mn1/3) 0.97 O 2. *Electrochem. solid-state Lett.* **2004**, *7*, A365–A368.

(131) Manthiram, A. A Reflection on Lithium-Ion Battery Cathode Chemistry. *Nat. Commun.* **2020**, *11*, 1550.

(132) Zhang, Y.; Wang, C.-Y. Cycle-Life Characterization of Automotive Lithium-Ion Batteries with LiNiO2 Cathode. *J. Electrochem. Soc.* **2009**, *156*, A527.

(133) Xiang, X.; Li, X.; Li, W. Preparation and Characterization of Size-Uniform Li[Li0.131Ni0.304Mn0.565]O2 Particles as Cathode Materials for High Energy Lithium Ion Battery. *J. Power Sources* **2013**, *230*, 89–95.

(134) Julien, C. M.; Mauger, A.; Zaghib, K.; Groult, H. Comparative Issues of Cathode Materials for Li-Ion Batteries. *Inorganics* **2014**, *2*, 132–154.

(135) Wandt, J.; Freiberg, A. T. S.; Ogrodnik, A.; Gasteiger, H. A. Singlet Oxygen Evolution from Layered Transition Metal Oxide Cathode Materials and Its Implications for Lithium-Ion Batteries. *Mater. Today* **2018**, *21*, 825–833.

(136) Zhang, S. S. Problems and Their Origins of Ni-Rich Layered Oxide Cathode Materials. *Energy Storage Mater.* **2020**, *24*, 247–254.

(137) Zheng, J.; Gu, M.; Genc, A.; Xiao, J.; Xu, P.; Chen, X.; Zhu, Z.; Zhao, W.; Pullan, L.; Wang, C.; Zhang, J.-G. Mitigating Voltage Fade in Cathode Materials by Improving the

Atomic Level Uniformity of Elemental Distribution. *Nano Lett.* **2014**, *14*, 2628–2635.

(138) Holzapfel, M.; Würsig, A.; Scheifele, W.; Vetter, J.; Novák, P. Oxygen, Hydrogen, Ethylene and CO2 Development in Lithium-Ion Batteries. *J. Power Sources* **2007**, *174*, 1156–1160.

(139) Liu, W.; Oh, P.; Liu, X.; Lee, M.; Cho, W.; Chae, S.; Kim, Y.; Cho, J. Nickel-rich Layered Lithium Transition-metal Oxide for High-energy Lithium-ion Batteries. *Angew. Chemie Int. Ed.* **2015**, *54*, 4440–4457.

(140) Zhang, H. Z.; Qiao, Q. Q.; Li, G. R.; Ye, S. H.; Gao, X. P. Surface Nitridation of Li-Rich Layered Li (Li 0.17 Ni 0.25 Mn 0.58) O 2 Oxide as Cathode Material for Lithium-Ion Battery. *J. Mater. Chem.* **2012**, *22*, 13104–13109.

(141) Choi, J. W.; Aurbach, D. Promise and Reality of Post-Lithium-Ion Batteries with High Energy Densities. *Nat. Rev. Mater.* **2016**, *1*, 16013.

(142) Ye, D.; Zeng, G.; Nogita, K.; Ozawa, K.; Hankel, M.; Searles, D. J.; Wang, L. Understanding the Origin of Li2MnO3 Activation in Li-Rich Cathode Materials for Lithium-Ion Batteries. *Adv. Funct. Mater.* **2015**, *25*, 7488–7496.

(143) Li, L.; Chen, Z.; Zhang, Q.; Xu, M.; Zhou, X.; Zhu, H.; Zhang, K. A Hydrolysis-Hydrothermal Route for the Synthesis of Ultrathin LiAlO2-Inlaid LiNi0.5Co0.2Mn0.3O2 as a High-Performance Cathode Material for Lithium Ion Batteries. *J. Mater. Chem. A* **2015**, *3*, 894–904.

(144) Liu, J.; Manthiram, A. Functional Surface Modifications of a High Capacity Layered Li [Li 0.2 Mn 0.54 Ni 0.13 Co 0.13] O 2 Cathode. *J. Mater. Chem.* **2010**, *20*, 3961–3967.

(145) Carroll, K. J.; Qian, D.; Fell, C.; Calvin, S.; Veith, G. M.; Chi, M.; Baggetto, L.; Meng, Y. S. Probing the Electrode/Electrolyte Interface in the Lithium Excess Layered Oxide Li 1.2 Ni 0.2 Mn 0.6 O 2. *Phys. Chem. Chem. Phys.* **2013**, *15*, 11128–11138.

(146) Oh, P.; Song, B.; Li, W.; Manthiram, A. Overcoming the Chemical Instability on Exposure to Air of Ni-Rich Layered Oxide Cathodes by Coating with Spinel LiMn 1.9 Al 0.1 O 4. *J. Mater. Chem. A* **2016**, *4*, 5839–5841.

(147) Kumai, K.; Miyashiro, H.; Kobayashi, Y.; Takei, K.; Ishikawa, R. Gas Generation Mechanism Due to Electrolyte Decomposition in Commercial Lithium-Ion Cell. *J. Power Sources* **1999**, *81*, 715–719.

(148) Thomas, M.; Bruce, P. G.; Goodenough, J. B. Lithium Mobility in the Layered Oxide Li1−XCoO2. *Solid State Ionics* **1985**, *17*, 13–19.

(149) Broussely, M.; Biensan, P.; Bonhomme, F.; Blanchard, P.; Herreyre, S.; Nechev, K.; Staniewicz, R. J. Main Aging Mechanisms in Li Ion Batteries. *J. Power Sources* **2005**, *146*, 90–96.

(150) Aurbach, D.; Markovsky, B.; Shechter, A.; Ein-Eli, Y.; Cohen, H. A Comparative Study of Synthetic Graphite and Li Electrodes in Electrolyte Solutions Based on Ethylene Carbonate-dimethyl Carbonate Mixtures. *J. Electrochem. Soc.* **1996**, *143*, 3809–3820.

(151) Wang, Y.; Yi, J.; Xia, Y. Recent Progress in Aqueous Lithium-Ion Batteries. *Adv. Energy Mater.* **2012**, *2*, 830–840.

(152) Haregewoin, A. M.; Wotango, A. S.; Hwang, B.-J. Electrolyte Additives for Lithium Ion Battery Electrodes: Progress and Perspectives. *Energy Environ. Sci.* **2016**, *9*, 1955–1988.

(153) Leung, K.; Budzien, J. L. Ab Initio Molecular Dynamics Simulations of the Initial Stages of Solid–Electrolyte Interphase Formation on Lithium Ion Battery Graphitic Anodes. *Phys. Chem. Chem. Phys.* **2010**, *12*, 6583–6586.

(154) Poozhikunnath, A.; Favata, J.; Ahmadi, B.; Xiong, J.; Bonville, L.; Shahbazmohamadi, S.; Jankovic, J.; Maric, R. Correlative Microscopy-Based Approach for Analyzing Microscopic Impurities in Carbon Black for Lithium-Ion Battery Applications. *J. Electrochem. Soc.* **2019**, *166*, A3335–A3341.

(155) Imhof, R.; Novák, P. Oxidative Electrolyte Solvent Degradation in Lithium-Ion Batteries: An In Situ Differential Electrochemical Mass Spectrometry Investigation. *J. Electrochem. Soc.* **1999**, *146*, 1702–1706.

(156) Vetter, J.; Holzapfel, M.; Wuersig, A.; Scheifele, W.; Ufheil, J.; Novák, P. In Situ Study on CO2 Evolution at Lithium-Ion Battery Cathodes. *J. Power Sources* **2006**, *159*, 277–281.

(157) Li, Y.; Tan, B.; Wu, Y. Mesoporous Co3O4 Nanowire Arrays for Lithium Ion Batteries with High Capacity and Rate Capability. *Nano Lett.* **2008**, *8*, 265–270.

(158) Abouimrane, A.; Cui, Y.; Chen, Z.; Belharouak, I.; Yahia, H. B.; Wu, H.; Assary, R.; Curtiss, L. A.; Amine, K. Enabling High Energy Density Li-Ion Batteries through Li2O Activation. *Nano Energy* **2016**, *27*, 196–201.

(159) Almeida, E. C.; Abbate, M.; Rosolen, J. M. Formation of Li2O in a Chemically Li-Intercalated V2O5 Xerogel. *Solid State Ionics* **2001**, *140*, 241–248.

(160) Li, H.; Richter, G.; Maier, J. Reversible Formation and Decomposition of LiF Clusters Using Transition Metal Fluorides as Precursors and Their Application in Rechargeable Li Batteries. *Adv. Mater.* **2003**, *15*, 736–739.

(161) Tebbe, J. L.; Holder, A. M.; Musgrave, C. B. Mechanisms of LiCoO2 Cathode Degradation by Reaction with HF and Protection by Thin Oxide Coatings. *ACS Appl. Mater. Interfaces* **2015**, *7*, 24265–24278.

(162) McEnaney, J. M.; Rohr, B. A.; Nielander, A. C.; Singh, A. R.; King, L. A.; Nørskov, J. K.; Jaramillo, T. F. A Cyclic Electrochemical Strategy to Produce Acetylene from CO 2, CH 4, or Alternative Carbon Sources. *Sustain. Energy Fuels* **2020**, *4*, 2752–2759.

(163) Yang, L.; Cheng, X.; Ma, Y.; Lou, S.; Cui, Y.; Guan, T.; Yin, G. Changing of SEI Film and Electrochemical Properties about MCMB Electrodes during Long-Term Charge/Discharge Cycles. *J. Electrochem. Soc.* **2013**, *160*, A2093–A2099.

(164) Chen, A.; Wang, K.; Li, J.; Mao, Q.; Xiao, Z.; Zhu, D.; Wang, G.; Liao, P.; He, J.; You, Y. The Formation, Detriment and Solution of Residual Lithium Compounds on Ni-Rich Layered Oxides in Lithium-Ion Batteries. *Front. Energy Res.* **2020**, *8*, 285.

(165) Cherkashinin, G.; Nikolowski, K.; Ehrenberg, H.; Jacke, S.; Dimesso, L.; Jaegermann, W. The Stability of the SEI Layer, Surface Composition and the Oxidation State of Transition Metals at the Electrolyte–Cathode Interface Impacted by the Electrochemical Cycling: X-Ray Photoelectron Spectroscopy Investigation. *Phys. Chem. Chem. Phys.* **2012**, *14*, 12321–12331.

(166) Cho, D.-H.; Jo, C.-H.; Cho, W.; Kim, Y.-J.; Yashiro, H.; Sun, Y.-K.; Myung, S.-T. Effect of Residual Lithium Compounds on Layer Ni-Rich Li[Ni0.7Mn0.3]O2. *J. Electrochem. Soc.* **2014**, *161*, A920–A926.

(167) Yabuuchi, N.; Yoshii, K.; Myung, S.-T.; Nakai, I.; Komaba, S. Detailed Studies of a High-Capacity Electrode Material for Rechargeable Batteries, Li2MnO3−LiCo1/3Ni1/3Mn1/3O2. *J. Am. Chem. Soc.* **2011**, *133*, 4404–4419.

(168) Droubay, C.; Wang, C.; Sushko, P. V; Du, Y. Direct Visualization of Li Dendrites Effect on LiCoO2 Cathodes by in Situ TEM 2.

(169) Wang, M.; Navrotsky, A. Enthalpy of Formation of LiNiO2, LiCoO2 and Their Solid Solution, LiNi1− XCoxO2. *Solid State Ionics* **2004**, *166*, 167–173.

(170) Yano, A.; Shikano, M.; Ueda, A.; Sakaebe, H.; Ogumi, Z. LiCoO2 Degradation Behavior in the High-Voltage Phase Transition Region and Improved Reversibility with Surface Coating. *J. Electrochem. Soc.* **2017**, *164*, A6116–A6122.

(171) Tian, C.; Lin, F.; Doeff, M. M. Electrochemical Characteristics of Layered Transition Metal Oxide Cathode Materials for Lithium Ion Batteries: Surface, Bulk Behavior, and Thermal Properties. *Acc. Chem. Res.* **2018**, *51*, 89–96.

(172) Kim, N. Y.; Yim, T.; Song, J. H.; Yu, J.-S.; Lee, Z. Microstructural Study on Degradation Mechanism of Layered LiNi0. 6Co0. 2Mn0. 2O2 Cathode Materials by Analytical Transmission Electron Microscopy. *J. Power Sources* **2016**, *307*, 641–648.

(173) Liao, P. Y.; Duh, J. G.; Sheen, S. R. Microstructure and Electrochemical Performance of LiNi0. 6Co0. 4− XMnxO2 Cathode Materials. *J. Power Sources* **2005**, *143*, 212–218.

(174) Ryu, H.; Park, G.; Yoon, C. S.; Sun, Y. Microstructural Degradation of Ni-Rich Li [NixCoyMn1− X− y] O2 Cathodes During Accelerated Calendar Aging. *Small* **2018**, *14*, 1803179.

(175) Van der Ven, A.; Bhattacharya, J.; Belak, A. A. Understanding Li Diffusion in Li-Intercalation Compounds. *Acc. Chem. Res.* **2012**, *46*, 1216–1225.

(176) Ito, A.; Li, D.; Sato, Y.; Arao, M.; Watanabe, M.; Hatano, M.; Horie, H.; Ohsawa, Y. Cyclic Deterioration and Its Improvement for Li-Rich Layered Cathode Material Li [Ni0. 17Li0. 2Co0. 07Mn0. 56] O2. *J. Power Sources* **2010**, *195*, 567–573.

(177) Jung, S.; Gwon, H.; Hong, J.; Park, K.; Seo, D.; Kim, H.; Hyun, J.; Yang, W.; Kang, K. Understanding the Degradation Mechanisms of LiNi0. 5Co0. 2Mn0. 3O2 Cathode Material in Lithium Ion Batteries. *Adv. Energy Mater.* **2014**, *4*, 1300787.

(178) Wei, G.; Lu, X.; Ke, F.; Huang, L.; Li, J.; Wang, Z.; Zhou, Z.; Sun, S. Crystal Habit-tuned Nanoplate Material of Li [Li1/3–2x/3NixMn2/3–x/3] O2 for High-rate Performance

Lithium-ion Batteries. *Adv. Mater.* **2010**, *22*, 4364–4367.

(179) Ryoo, H.; Bae, H. Bin; Kim, Y.; Kim, J.; Lee, S.; Chung, S. Frenkel-Defect-Mediated Chemical Ordering Transition in a Li–Mn–Ni Spinel Oxide. *Angew. Chemie Int. Ed.* **2015**, *54*, 7963–7967.

(180) Mohanty, D.; Sefat, A. S.; Li, J.; Meisner, R. A.; Rondinone, A. J.; Payzant, E. A.; Abraham, D. P.; Wood III, D. L.; Daniel, C. Correlating Cation Ordering and Voltage Fade in a Lithium–Manganese-Rich Lithium-Ion Battery Cathode Oxide: A Joint Magnetic Susceptibility and TEM Study. *Phys. Chem. Chem. Phys.* **2013**, *15*, 19496–19509.

(181) Song, B.; Liu, Z.; Lai, M. O.; Lu, L. Structural Evolution and the Capacity Fade Mechanism upon Long-Term Cycling in Li-Rich Cathode Material. *Phys. Chem. Chem. Phys.* **2012**, *14*, 12875–12883.

(182) Lee, J.; Urban, A.; Li, X.; Su, D.; Hautier, G.; Ceder, G. Unlocking the Potential of Cation-Disordered Oxides for Rechargeable Lithium Batteries. *Science (80-.).* **2014**, *343*, 519–522.

(183) Lin, F.; Markus, I. M.; Doeff, M. M.; Xin, H. L. Chemical and Structural Stability of Lithium-Ion Battery Electrode Materials under Electron Beam. *Sci. Rep.* **2014**, *4*, 5694.

(184) Mori, D.; Kobayashi, H.; Shikano, M.; Nitani, H.; Kageyama, H.; Koike, S.; Sakaebe, H.; Tatsumi, K. Bulk and Surface Structure Investigation for the Positive Electrodes of Degraded Lithium-Ion Cell after Storage Test Using X-Ray Absorption near-Edge Structure Measurement. *J. Power Sources* **2009**, *189*, 676–680.

(185) Wang, H.; Jang, Y.; Huang, B.; Sadoway, D. R.; Chiang, Y. TEM Study of Electrochemical Cycling-induced Damage and Disorder in LiCoO2 Cathodes for Rechargeable Lithium Batteries. *J. Electrochem. Soc.* **1999**, *146*, 473–480.

(186) Ryoo, H.; Lee, S.; Kim, J.; Chung, S. Effect of Chemical Bonding Characteristics on Ordering Structure in Li Spinel Oxides. *Adv. Funct. Mater.* **2018**, 1805972.

(187) Thomas, M.; David, W. I. F.; Goodenough, J. B.; Groves, P. Synthesis and Structural Characterization of the Normal Spinel Li [Ni2] O4. *Mater. Res. Bull.* **1985**, *20*, 1137–1146.

(188) Kan, W. H.; Huq, A.; Manthiram, A. Exploration of a Metastable Normal Spinel Phase Diagram for the Quaternary Li–Ni–Mn–Co–O System. *Chem. Mater.* **2016**, *28*, 1832–1837.

(189) Yamada, A.; Tanaka, M.; Tanaka, K.; Sekai, K. Jahn–Teller Instability in Spinel Li–Mn–O. *J. Power Sources* **1999**, *81*, 73–78.

(190) Chiang, Y.-M.; Wang, H.; Jang, Y.-I. Electrochemically Induced Cation Disorder and Phase Transformations in Lithium Intercalation Oxides. *Chem. Mater.* **2001**, *13*, 53–63.

(191) Momma, K.; Izumi, F. VESTA 3 for Three-Dimensional Visualization of Crystal, Volumetric and Morphology Data. *J. Appl. Crystallogr.* **2011**, *44*, 1272–1276.

(192) Sigala, C.; Guyomard, D.; Verbaere, A.; Piffard, Y.; Tournoux, M. Positive Electrode

Materials with High Operating Voltage for Lithium Batteries: LiCryMn2− YO4 (0≤ Y≤ 1). *Solid State Ionics* **1995**, *81*, 167–170.

(193) Ammundsen, B.; Paulsen, J. Novel Lithium-ion Cathode Materials Based on Layered Manganese Oxides. *Adv. Mater.* **2001**, *13*, 943–956.

(194) Tarascon, J. M.; Wang, E.; Shokoohi, F. K.; McKinnon, W. R.; Colson, S. The Spinel Phase of LiMn2 O 4 as a Cathode in Secondary Lithium Cells. *J. Electrochem. Soc.* **1991**, *138*, 2859.

(195) Lyu, Y.; Ben, L.; Sun, Y.; Tang, D.; Xu, K.; Gu, L.; Xiao, R.; Li, H.; Chen, L.; Huang, X. Atomic Insight into Electrochemical Inactivity of Lithium Chromate (LiCrO2): Irreversible Migration of Chromium into Lithium Layers in Surface Regions. *J. Power Sources* **2015**, *273*, 1218–1225.

(196) Oishi, M.; Yogi, C.; Watanabe, I.; Ohta, T.; Orikasa, Y.; Uchimoto, Y.; Ogumi, Z. Direct Observation of Reversible Charge Compensation by Oxygen Ion in Li-Rich Manganese Layered Oxide Positive Electrode Material, Li1. 16Ni0. 15Co0. 19Mn0. 50O2. *J. Power Sources* **2015**, *276*, 89–94.

(197) Radin, M. D.; Hy, S.; Sina, M.; Fang, C.; Liu, H.; Vinckeviciute, J.; Zhang, M.; Whittingham, M. S.; Meng, Y. S.; Van der Ven, A. Narrowing the Gap between Theoretical and Practical Capacities in Li-Ion Layered Oxide Cathode Materials. *Adv. Energy Mater.* **2017**, *7*, 1602888.

(198) Goodenough, J. B.; Wickham, D. G.; Croft, W. J. Some Magnetic and Crystallographic Properties of the System Li+ XNi++ 1− 2xNi+++ XO. *J. Phys. Chem. Solids* **1958**, *5*, 107–116.

(199) SASAKI, S.; FUJINO, K.; TAKÉUCHI, Y. X-Ray Determination of Electron-Density Distributions in Oxides, MgO, MnO, CoO, and NiO, and Atomic Scattering Factors of Their Constituent Atoms. *Proc. Japan Acad. Ser. B* **1979**, *55*, 43–48.

(200) Urban, A.; Lee, J.; Ceder, G. The Configurational Space of Rocksalt-Type Oxides for High-Capacity Lithium Battery Electrodes. *Adv. Energy Mater.* **2014**, *4*, 1400478.

(201) Wang, R.; Li, X.; Liu, L.; Lee, J.; Seo, D.-H.; Bo, S.-H.; Urban, A.; Ceder, G. A Disordered Rock-Salt Li-Excess Cathode Material with High Capacity and Substantial Oxygen Redox Activity: Li1. 25Nb0. 25Mn0. 5O2. *Electrochem. commun.* **2015**, *60*, 70–73.

(202) Kang, K.; Meng, Y. S.; Bréger, J.; Grey, C. P.; Ceder, G. Electrodes with High Power and High Capacity for Rechargeable Lithium Batteries. *Science (80-.).* **2006**, *311*, 977–980.

(203) Spahr, M. E.; Novák, P.; Schnyder, B.; Haas, O.; Nesper, R. Characterization of Layered Lithium Nickel Manganese Oxides Synthesized by a Novel Oxidative Coprecipitation Method and Their Electrochemical Performance as Lithium Insertion Electrode Materials. *J. Electrochem. Soc.* **1998**, *145*, 1113–1121.

(204) He, P.; Yu, H.; Zhou, H. Layered Lithium Transition Metal Oxide Cathodes towards High Energy Lithium-Ion Batteries. *J. Mater. Chem.* **2012**, *22*, 3680–3695.

(205) Mohanty, D.; Li, J.; Nagpure, S. C.; Wood, D. L.; Daniel, C. Understanding the Structure

and Structural Degradation Mechanisms in High-Voltage, Lithium-Manganese–Rich Lithium-Ion Battery Cathode Oxides: A Review of Materials Diagnostics. *MRS Energy Sustain.* **2015**, *2*, E15.

(206) Chen, B.; Zhao, B.; Zhou, J.; Fang, Z.; Huang, Y.; Zhu, X.; Sun, Y. Surface Modification with Oxygen Vacancy in Li-Rich Layered Oxide Li1. 2Mn0. 54Ni0. 13Co0. 13O2 for Lithium-Ion Batteries. *J. Mater. Sci. Technol.* **2019**, *35*, 994–1002.

(207) Qian, D.; Xu, B.; Chi, M.; Meng, Y. S. Uncovering the Roles of Oxygen Vacancies in Cation Migration in Lithium Excess Layered Oxides. *Phys. Chem. Chem. Phys.* **2014**, *16*, 14665–14668.

(208) Fell, C. R.; Qian, D.; Carroll, K. J.; Chi, M.; Jones, J. L.; Meng, Y. S. Correlation between Oxygen Vacancy, Microstrain, and Cation Distribution in Lithium-Excess Layered Oxides during the First Electrochemical Cycle. *Chem. Mater.* **2013**, *25*, 1621–1629.

(209) Wynn, T. A.; Fang, C.; Zhang, M.; Liu, H.; Davies, D. M.; Wang, X.; Lau, D.; Lee, J. Z.; Huang, B.-Y.; Fung, K. Z. Mitigating Oxygen Release in Anionic-Redox-Active Cathode Materials by Cationic Substitution through Rational Design. *J. Mater. Chem. A* **2018**.

(210) Wang, Z.; Liu, E.; He, C.; Shi, C.; Li, J.; Zhao, N. Effect of Amorphous FePO4 Coating on Structure and Electrochemical Performance of Li1. 2Ni0. 13Co0. 13Mn0. 54O2 as Cathode Material for Li-Ion Batteries. *J. Power Sources* **2013**, *236*, 25–32.

(211) Zhao, J.; Zhang, W.; Huq, A.; Misture, S. T.; Zhang, B.; Guo, S.; Wu, L.; Zhu, Y.; Chen, Z.; Amine, K. In Situ Probing and Synthetic Control of Cationic Ordering in Ni-Rich Layered Oxide Cathodes. *Adv. Energy Mater.* **2017**, *7*, 1601266.

(212) Freire, M.; Lebedev, O. I.; Maignan, A.; Jordy, C.; Pralong, V. Nanostructured Li 2 MnO 3: A Disordered Rock Salt Type Structure for High Energy Density Li Ion Batteries. *J. Mater. Chem. A* **2017**, *5*, 21898–21902.

(213) Lin, Q.; Guan, W.; Zhou, J.; Meng, J.; Huang, W.; Chen, T.; Gao, Q.; Wei, X.; Zeng, Y.; Li, J.; Zhang, Z. Ni–Li Anti-Site Defect Induced Intragranular Cracking in Ni-Rich Layer-Structured Cathode. *Nano Energy* **2020**, *76*, 105021.

(214) Chen, X.; Li, D.; Mo, Y.; Jia, X.; Jia, J.; Yao, C.; Chen, D.; Chen, Y. Cathode Materials with Cross-Stack Structures for Suppressing Intergranular Cracking and High-Performance Lithium-Ion Batteries. *Electrochim. Acta* **2018**, *261*, 513–520.

(215) Wang, B.; Bates, J. B.; Hart, F. X.; Sales, B. C.; Zuhr, R. A.; Robertson, J. D. Characterization of Thin-film Rechargeable Lithium Batteries with Lithium Cobalt Oxide Cathodes. *J. Electrochem. Soc.* **1996**, *143*, 3203–3213.

(216) Winter, M.; Besenhard, J. O.; Spahr, M. E.; Novak, P. Insertion Electrode Materials for Rechargeable Lithium Batteries. *Adv. Mater.* **1998**, *10*, 725–763.

(217) Kim, U.-H.; Myung, S.-T.; Yoon, C. S.; Sun, Y.-K. Extending the Battery Life Using an Al-Doped Li [Ni0. 76Co0. 09Mn0. 15] O2 Cathode with Concentration Gradients for Lithium Ion Batteries. *ACS Energy Lett.* **2017**, *2*, 1848–1854.

(218) Kondrakov, A. O.; Schmidt, A.; Xu, J.; Geßwein, H.; Mönig, R.; Hartmann, P.; Sommer,

H.; Brezesinski, T.; Janek, J. Anisotropic Lattice Strain and Mechanical Degradation of High-and Low-Nickel NCM Cathode Materials for Li-Ion Batteries. *J. Phys. Chem. C* **2017**, *121*, 3286–3294.

(219) Zheng, J.; Gu, M.; Xiao, J.; Zuo, P.; Wang, C.; Zhang, J.-G. Corrosion/Fragmentation of Layered Composite Cathode and Related Capacity/Voltage Fading during Cycling Process. *Nano Lett.* **2013**, *13*, 3824–3830.

(220) Kızıltaş-Yavuz, N.; Herklotz, M.; Hashem, A. M.; Abuzeid, H. M.; Schwarz, B.; Ehrenberg, H.; Mauger, A.; Julien, C. M. Synthesis, Structural, Magnetic and Electrochemical Properties of LiNi1/3Mn1/3Co1/3O2 Prepared by a Sol–Gel Method Using Table Sugar as Chelating Agent. *Electrochim. Acta* **2013**, *113*, 313–321.

(221) Ahmed, S.; Pokle, A.; Schweidler, S.; Beyer, A.; Bianchini, M.; Walther, F.; Mazilkin, A.; Hartmann, P.; Brezesinski, T.; Janek, J.; Volz, K. The Role of Intragranular Nanopores in Capacity Fade of Nickel-Rich Layered Li(Ni1–x–YCoxMny)O2 Cathode Materials. *ACS Nano* **2019**, *13*, 10694–10704.

(222) Mu, L.; Lin, R.; Xu, R.; Han, L.; Xia, S.; Sokaras, D.; Steiner, J. D.; Weng, T.-C.; Nordlund, D.; Doeff, M. M. Oxygen Release Induced Chemomechanical Breakdown of Layered Cathode Materials. *Nano Lett.* **2018**, *18*, 3241–3249.

(223) Yoon, W.-S.; Chung, K. Y.; McBreen, J.; Yang, X.-Q. A Comparative Study on Structural Changes of LiCo1/3Ni1/3Mn1/3O2 and LiNi0.8Co0.15Al0.05O2 during First Charge Using in Situ XRD. *Electrochem. commun.* **2006**, *8*, 1257–1262.

(224) Xu, C.; Märker, K.; Lee, J.; Mahadevegowda, A.; Reeves, P. J.; Day, S. J.; Groh, M. F.; Emge, S. P.; Ducati, C.; Layla Mehdi, B.; Tang, C. C.; Grey, C. P. Bulk Fatigue Induced by Surface Reconstruction in Layered Ni-Rich Cathodes for Li-Ion Batteries. *Nat. Mater.* **2021**, *20*, 84–92.

(225) Lebens-Higgins, Z. W.; Sallis, S.; Faenza, N. V; Badway, F.; Pereira, N.; Halat, D. M.; Wahila, M.; Schlueter, C.; Lee, T.-L.; Yang, W.; Grey, C. P.; Amatucci, G. G.; Piper, L. F. J. Evolution of the Electrode–Electrolyte Interface of LiNi0.8Co0.15Al0.05O2 Electrodes Due to Electrochemical and Thermal Stress. *Chem. Mater.* **2018**, *30*, 958–969.

(226) Lim, J.-M.; Hwang, T.; Kim, D.; Park, M.-S.; Cho, K.; Cho, M. Intrinsic Origins of Crack Generation in Ni-Rich LiNi0.8Co0.1Mn0.1O2 Layered Oxide Cathode Material. *Sci. Rep.* **2017**, *7*, 39669.

(227) Ryu, H.-H.; Park, N.-Y.; Yoon, D. R.; Kim, U.-H.; Yoon, C. S.; Sun, Y.-K. New Class of Ni-Rich Cathode Materials Li[NixCoyB1−x−y]O2 for Next Lithium Batteries. *Adv. Energy Mater.* **2020**, *10*, 2000495.

(228) Li, W.; Asl, H. Y.; Xie, Q.; Manthiram, A. Collapse of LiNi1–x–YCoxMnyO2 Lattice at Deep Charge Irrespective of Nickel Content in Lithium-Ion Batteries. *J. Am. Chem. Soc.* **2019**, *141*, 5097–5101.

(229) Li, W.; Xia, Y.; Zhu, J.; Luo, H. State-of-Charge Dependence of Mechanical Response of Lithium-Ion Batteries: A Result of Internal Stress. *J. Electrochem. Soc.* **2018**, *165*, A1537–A1546.

(230) Su, Y.; Yang, Y.; Chen, L.; Lu, Y.; Bao, L.; Chen, G.; Yang, Z.; Zhang, Q.; Wang, J.; Chen, R. Improving the Cycling Stability of Ni-Rich Cathode Materials by Fabricating Surface Rock Salt Phase. *Electrochim. Acta* **2018**, *292*, 217–226.

(231) Wang, M.; Navrotsky, A. LiMO2 (M= Mn, Fe, and Co): Energetics, Polymorphism and Phase Transformation. *J. Solid State Chem.* **2005**, *178*, 1230–1240.

(232) Yang, C.; Shao, R.; Wang, Q.; Zhou, T.; Lu, J.; Jiang, N.; Gao, P.; Liu, W.; Yu, Y.; Zhou, H. Bulk and Surface Degradation in Layered Ni-Rich Cathode for Li Ions Batteries: Defect Proliferation via Chain Reaction Mechanism. *Energy Storage Mater.* **2021**, *35*, 62–69.

(233) Watanabe, S.; Kinoshita, M.; Nakura, K. Capacity Fade of LiNi (1− X− y) CoxAlyO2 Cathode for Lithium-Ion Batteries during Accelerated Calendar and Cycle Life Test. I. Comparison Analysis between LiNi (1− X− y) CoxAlyO2 and LiCoO2 Cathodes in Cylindrical Lithium-Ion Cells during Long Term Storag. *J. Power Sources* **2014**, *247*, 412–422.

(234) Liang, L.; Zhang, W.; Zhao, F.; Denis, D. K.; Zaman, F. uz; Hou, L.; Yuan, C. Surface/Interface Structure Degradation of Ni-Rich Layered Oxide Cathodes toward Lithium-Ion Batteries: Fundamental Mechanisms and Remedying Strategies. *Adv. Mater. Interfaces* **2020**, *7*, 1901749.

(235) Jiang, Y.; Qin, C.; Yan, P.; Sui, M. Origins of Capacity and Voltage Fading of LiCoO2 upon High Voltage Cycling. *J. Mater. Chem. A* **2019**, *7*, 20824–20831.

(236) Hu, E.; Wang, X.; Yu, X.; Yang, X.-Q. Probing the Complexities of Structural Changes in Layered Oxide Cathode Materials for Li-Ion Batteries during Fast Charge–Discharge Cycling and Heating. *Acc. Chem. Res.* **2018**, *51*, 290–298.

(237) Yan, P.; Zheng, J.; Gu, M.; Xiao, J.; Zhang, J.-G.; Wang, C.-M. Intragranular Cracking as a Critical Barrier for High-Voltage Usage of Layer-Structured Cathode for Lithium-Ion Batteries. *Nat. Commun.* **2017**, *8*, 14101.

(238) Li, Y.; Qian, K.; He, Y.-B.; Kaneti, Y. V.; Liu, D.; Luo, D.; Li, H.; Li, B.; Kang, F. Study on the Reversible Capacity Loss of Layered Oxide Cathode during Low-Temperature Operation. *J. Power Sources* **2017**, *342*, 24–30.

(239) Zhou, Y.-N.; Yue, J.-L.; Hu, E.; Li, H.; Gu, L.; Nam, K.-W.; Bak, S.-M.; Yu, X.; Liu, J.; Bai, J.; Dooryhee, E.; Fu, Z.-W.; Yang, X.-Q. High-Rate Charging Induced Intermediate Phases and Structural Changes of Layer-Structured Cathode for Lithium-Ion Batteries. *Adv. Energy Mater.* **2016**, *6*, 1600597.

(240) Wu, F.; Fang, S.; Kuenzel, M.; Mullaliu, A.; Kim, J.-K.; Gao, X.; Diemant, T.; Kim, G.-T.; Passerini, S. Dual-Anion Ionic Liquid Electrolyte Enables Stable Ni-Rich Cathodes in Lithium-Metal Batteries. *Joule* **2021**, *5*, 2177–2194.

(241) Harlow, J. E.; Ma, X.; Li, J.; Logan, E.; Liu, Y.; Zhang, N.; Ma, L.; Glazier, S. L.; Cormier, M. M. E.; Genovese, M.; Buteau, S.; Cameron, A.; Stark, J. E.; Dahn, J. R. A Wide Range of Testing Results on an Excellent Lithium-Ion Cell Chemistry to Be Used as Benchmarks for New Battery Technologies. *J. Electrochem. Soc.* **2019**, *166*, A3031–A3044.

(242) Poizot, P.; Laruelle, S.; Grugeon, S.; Dupont, L.; Tarascon, J. M. Nano-Sized Transition-Metal Oxides as Negative-Electrode Materials for Lithium-Ion Batteries. *Nature* **2000**, *407*, 496.

(243) Li, X.; Xie, Z.; Liu, W.; Ge, W.; Wang, H.; Qu, M. Effects of Fluorine Doping on Structure, Surface Chemistry, and Electrochemical Performance of LiNi0. 8Co0. 15Al0. 05O2. *Electrochim. Acta* **2015**, *174*, 1122–1130.

(244) Karki, K.; Huang, Y.; Hwang, S.; Gamalski, A. D.; Whittingham, M. S.; Zhou, G.; Stach, E. A. Tuning the Activity of Oxygen in LiNi0. 8Co0. 15Al0. 05O2 Battery Electrodes. *ACS Appl. Mater. Interfaces* **2016**, *8*, 27762–27771.

(245) Nanda, J.; Remillard, J.; O'Neill, A.; Bernardi, D.; Ro, T.; Nietering, K. E.; Go, J.; Miller, T. J. Local State-of-Charge Mapping of Lithium-Ion Battery Electrodes. *Adv. Funct. Mater.* **2011**, *21*, 3282–3290.

(246) Tian, C.; Xu, Y.; Nordlund, D.; Lin, F.; Liu, J.; Sun, Z.; Liu, Y.; Doeff, M. Charge Heterogeneity and Surface Chemistry in Polycrystalline Cathode Materials. *Joule* **2018**, *2*, 464–477.

(247) Zhu, X.; Revilla, R. I.; Hubin, A. Direct Correlation between Local Surface Potential Measured by Kelvin Probe Force Microscope and Electrochemical Potential of LiNi0.80Co0.15Al0.05O2 Cathode at Different State of Charge. *J. Phys. Chem. C* **2018**, *122*, 28556–28563.

(248) Sun, Y.-K.; Myung, S.-T.; Park, B.-C.; Prakash, J.; Belharouak, I.; Amine, K. High-Energy Cathode Material for Long-Life and Safe Lithium Batteries. *Nat. Mater.* **2009**, *8*, 320.

(249) Lin, M.; Ben, L.; Sun, Y.; Wang, H.; Yang, Z.; Gu, L.; Yu, X.; Yang, X.-Q.; Zhao, H.; Yu, R. Insight into the Atomic Structure of High-Voltage Spinel LiNi0. 5Mn1. 5O4 Cathode Material in the First Cycle. *Chem. Mater.* **2014**, *27*, 292–303.

(250) Huang, R.; Ikuhara, Y. STEM Characterization for Lithium-Ion Battery Cathode Materials. *Curr. Opin. Solid State Mater. Sci.* **2012**, *16*, 31–38.

(251) Li, H.; Liu, D.; Zhang, L.; Qian, K.; Shi, R.; Kang, F.; Li, B. Combination Effect of Bulk Structure Change and Surface Rearrangement on the Electrochemical Kinetics of LiNi0.80Co0.15Al0.05O2 During Initial Charging Processes. *ACS Appl. Mater. Interfaces* **2018**.

(252) van Bommel, A.; Dahn, J. R. Kinetics Study of the High Potential Range of Lithium-Rich Transition-Metal Oxides for Lithium-Ion Batteries by Electrochemical Methods. *Electrochem. Solid-State Lett.* **2010**, *13*, A62–A64.

(253) Yang, Y.; Xu, R.; Zhang, K.; Lee, S.; Mu, L.; Liu, P.; Waters, C. K.; Spence, S.; Xu, Z.; Wei, C. Quantification of Heterogeneous Degradation in Li-ion Batteries. *Adv. Energy Mater.* **2019**, *9*, 1900674.

(254) Cheng, X.; Zheng, J.; Lu, J.; Li, Y.; Yan, P.; Zhang, Y. Realizing Superior Cycling Stability of Ni-Rich Layered Cathode by Combination of Grain Boundary Engineering and Surface Coating. *Nano Energy* **2019**, *62*, 30–37.

(255) Park, K.-J.; Hwang, J.-Y.; Ryu, H.-H.; Maglia, F.; Kim, S.-J.; Lamp, P.; Yoon, C. S.; Sun, Y.-K. Degradation Mechanism of Ni-Enriched NCA Cathode for Lithium Batteries: Are Microcracks Really Critical? *ACS Energy Lett.* **2019**, *4*, 1394–1400.

(256) Yoon, C. S.; Jun, D.-W.; Myung, S.-T.; Sun, Y.-K. Structural Stability of LiNiO2 Cycled above 4.2 V. *ACS Energy Lett.* **2017**, *2*, 1150–1155.

(257) Yan, P.; Nie, A.; Zheng, J.; Zhou, Y.; Lu, D.; Zhang, X.; Xu, R.; Belharouak, I.; Zu, X.; Xiao, J.; Amine, K.; Liu, J.; Gao, F.; Shahbazian-Yassar, R.; Zhang, J.-G.; Wang, C.-M. Evolution of Lattice Structure and Chemical Composition of the Surface Reconstruction Layer in Li1.2Ni0.2Mn0.6O2 Cathode Material for Lithium Ion Batteries. *Nano Lett.* **2015**, *15*, 514–522.

(258) Heenan, T. M. M.; Wade, A.; Tan, C.; Parker, J. E.; Matras, D.; Leach, A. S.; Robinson, J. B.; Llewellyn, A.; Dimitrijevic, A.; Jervis, R.; Quinn, P. D.; Brett, D. J. L.; Shearing, P. R. Identifying the Origins of Microstructural Defects Such as Cracking within Ni-Rich NMC811 Cathode Particles for Lithium-Ion Batteries. *Adv. Energy Mater.* **2020**, *10*, 2002655.

(259) Ruess, R.; Schweidler, S.; Hemmelmann, H.; Conforto, G.; Bielefeld, A.; Weber, D. A.; Sann, J.; Elm, M. T.; Janek, J. Influence of NCM Particle Cracking on Kinetics of Lithium-Ion Batteries with Liquid or Solid Electrolyte. *J. Electrochem. Soc.* **2020**, *167*, 100532.

(260) Li, T.; Yuan, X.-Z.; Zhang, L.; Song, D.; Shi, K.; Bock, C. Degradation Mechanisms and Mitigation Strategies of Nickel-Rich NMC-Based Lithium-Ion Batteries. *Electrochem. Energy Rev.* **2020**, *3*, 43–80.

(261) Li, J.; Li, Y.; Guo, Y.; Lv, J.; Yi, W.; Ma, P. A Facile Method to Enhance Electrochemical Performance of High-Nickel Cathode Material Li(Ni0.8Co0.1Mn0.1)O2 via Ti Doping. *J. Mater. Sci. Mater. Electron.* **2018**, *29*, 10702–10708.

(262) Shan, W.; Huang, S.; Zhang, H.; Hou, X. Surface Coating for High-Nickel Cathode Materials to Achieve Excellent Cycle Performance at Elevated Temperatures. *J. Alloys Compd.* **2021**, *862*, 158022.

(263) Kim, Y.; Seong, W. M.; Manthiram, A. Cobalt-Free, High-Nickel Layered Oxide Cathodes for Lithium-Ion Batteries: Progress, Challenges, and Perspectives. *Energy Storage Mater.* **2021**, *34*, 250–259.

(264) Noh, H.-J.; Youn, S.; Yoon, C. S.; Sun, Y.-K. Comparison of the Structural and Electrochemical Properties of Layered Li [NixCoyMnz] O2 (X= 1/3, 0.5, 0.6, 0.7, 0.8 and 0.85) Cathode Material for Lithium-Ion Batteries. *J. Power Sources* **2013**, *233*, 121–130.

(265) Xie, Q.; Cui, Z.; Manthiram, A. Unveiling the Stabilities of Nickel-Based Layered Oxide Cathodes at an Identical Degree of Delithiation in Lithium-Based Batteries. *Adv. Mater.* **2021**, *n/a*, 2100804.

(266) Zhu, Y.; Casselman, M. D.; Li, Y.; Wei, A.; Abraham, D. P. Perfluoroalkyl-Substituted Ethylene Carbonates: Novel Electrolyte Additives for High-Voltage Lithium-Ion Batteries. *J. Power Sources* **2014**, *246*, 184–191.

(267) Wagner, R.; Brox, S.; Kasnatscheew, J.; Gallus, D. R.; Amereller, M.; Cekic-Laskovic, I.; Winter, M. Vinyl Sulfones as SEI-Forming Additives in Propylene Carbonate Based Electrolytes for Lithium-Ion Batteries. *Electrochem. commun.* **2014**, *40*, 80–83.

(268) Zheng, F.; Ou, X.; Pan, Q.; Xiong, X.; Yang, C.; Fu, Z.; Liu, M. Nanoscale Gadolinium Doped Ceria (GDC) Surface Modification of Li-Rich Layered Oxide as a High Performance Cathode Material for Lithium Ion Batteries. *Chem. Eng. J.* **2018**, *334*, 497–507.

(269) Wang, C.-C.; Lin, Y.-C.; Chou, P.-H. Mitigation of Layer to Spinel Conversion of a Lithium-Rich Layered Oxide Cathode by Substitution of Al in a Lithium Ion Battery. *RSC Adv.* **2015**, *5*, 68919–68928.

(270) Fell, C. R.; Chi, M.; Meng, Y. S.; Jones, J. L. In Situ X-Ray Diffraction Study of the Lithium Excess Layered Oxide Compound Li [Li0. 2Ni0. 2Mn0. 6] O2 during Electrochemical Cycling. *Solid State Ionics* **2012**, *207*, 44–49.

(271) Smith, A. J.; Dahn, H. M.; Burns, J. C.; Dahn, J. R. Long-Term Low-Rate Cycling of LiCoO2/Graphite Li-Ion Cells at 55 C. *J. Electrochem. Soc.* **2012**, *159*, A705–A710.

(272) Song, B.; Liu, H.; Liu, Z.; Xiao, P.; Lai, M. O.; Lu, L. High Rate Capability Caused by Surface Cubic Spinels in Li-Rich Layer-Structured Cathodes for Li-Ion Batteries. *Sci. Rep.* **2013**, *3*, 3094.

(273) Liu, X.; Huang, T.; Yu, A. Surface Phase Transformation and CaF2 Coating for Enhanced Electrochemical Performance of Li-Rich Mn-Based Cathodes. *Electrochim. Acta* **2015**, *163*, 82–92.

(274) Kleiner, K.; Dixon, D.; Jakes, P.; Melke, J.; Yavuz, M.; Roth, C.; Nikolowski, K.; Liebau, V.; Ehrenberg, H. Fatigue of LiNi0.8Co0.15Al0.05O2 in Commercial Li Ion Batteries. *J. Power Sources* **2015**, *273*, 70–82.

(275) Lim, B.; Yoon, S.; Park, K.; Yoon, C. S.; Kim, S.; Lee, J. J.; Sun, Y. Advanced Concentration Gradient Cathode Material with Two-Slope for High-Energy and Safe Lithium Batteries. *Adv. Funct. Mater.* **2015**, *25*, 4673–4680.

(276) Yan, P.; Zheng, J.; Liu, J.; Wang, B.; Cheng, X.; Zhang, Y.; Sun, X.; Wang, C.; Zhang, J.-G. Tailoring Grain Boundary Structures and Chemistry of Ni-Rich Layered Cathodes for Enhanced Cycle Stability of Lithium-Ion Batteries. *Nat. Energy* **2018**, 1.

(277) Liu, H.; Xu, J.; Ma, C.; Meng, Y. S. A New O3-Type Layered Oxide Cathode with High Energy/Power Density for Rechargeable Na Batteries. *Chem. Commun.* **2015**, *51*, 4693–4696.

(278) Zheng, F.; Yang, C.; Xiong, X.; Xiong, J.; Hu, R.; Chen, Y.; Liu, M. Nanoscale Surface Modification of Lithium-Rich Layered-Oxide Composite Cathodes for Suppressing Voltage Fade. *Angew. Chemie Int. Ed.* **2015**, *54*, 13058–13062.

(279) Greiner, M. T.; Helander, M. G.; Tang, W.-M.; Wang, Z.-B.; Qiu, J.; Lu, Z.-H. Universal Energy-Level Alignment of Molecules on Metal Oxides. *Nat. Mater.* **2012**, *11*, 76.

(280) Lin, Q.; Guan, W.; Meng, J.; Huang, W.; Wei, X.; Zeng, Y.; Li, J.; Zhang, Z. A New Insight into Continuous Performance Decay Mechanism of Ni-Rich Layered Oxide Cathode

for High Energy Lithium Ion Batteries. *Nano Energy* **2018**, *54*, 313–321.

(281) Xiao, B.; Sun, X. Surface and Subsurface Reactions of Lithium Transition Metal Oxide Cathode Materials: An Overview of the Fundamental Origins and Remedying Approaches. *Adv. Energy Mater.* **2018**, *8*, 1802057.

(282) Zhu, W.; Wang, Y.; Liu, D.; Gariépy, V.; Gagnon, C.; Vijh, A.; Trudeau, M. L.; Zaghib, K. Application of Operando X-Ray Diffractometry in Various Aspects of the Investigations of Lithium/Sodium-Ion Batteries. *Energies* **2018**, *11*, 2963.

(283) Chen, Z.; Qin, Y.; Amine, K.; Sun, Y.-K. Role of Surface Coating on Cathode Materials for Lithium-Ion Batteries. *J. Mater. Chem.* **2010**, *20*, 7606–7612.

(284) Song, B.; Li, W.; Oh, S.-M.; Manthiram, A. Long-Life Nickel-Rich Layered Oxide Cathodes with a Uniform Li2ZrO3 Surface Coating for Lithium-Ion Batteries. *ACS Appl. Mater. Interfaces* **2017**, *9*, 9718–9725.

(285) Sun, Y.; Lee, M.; Yoon, C. S.; Hassoun, J.; Amine, K.; Scrosati, B. The Role of AlF3 Coatings in Improving Electrochemical Cycling of Li-Enriched Nickel-Manganese Oxide Electrodes for Li-Ion Batteries. *Adv. Mater.* **2012**, *24*, 1192–1196.

(286) Zhang, X.; Belharouak, I.; Li, L.; Lei, Y.; Elam, J. W.; Nie, A.; Chen, X.; Yassar, R. S.; Axelbaum, R. L. Structural and Electrochemical Study of Al2O3 and TiO2 Coated Li1. 2Ni0. 13Mn0. 54Co0. 13O2 Cathode Material Using ALD. *Adv. Energy Mater.* **2013**, *3*, 1299–1307.

(287) Hu, S.-K.; Cheng, G.-H.; Cheng, M.-Y.; Hwang, B.-J.; Santhanam, R. Cycle Life Improvement of ZrO2-Coated Spherical LiNi1/3Co1/3Mn1/3O2 Cathode Material for Lithium Ion Batteries. *J. Power Sources* **2009**, *188*, 564–569.

(288) Miyashiro, H.; Seki, S.; Kobayashi, Y.; Ohno, Y.; Mita, Y.; Usami, A. All-Solid-State Lithium Polymer Secondary Battery with LiNi0. 5Mn1. 5O4 by Mixing of Li3PO4. *Electrochem. commun.* **2005**, *7*, 1083–1086.

(289) Chen, Z.; Chao, D.; Lin, J.; Shen, Z. Recent Progress in Surface Coating of Layered LiNixCoyMnzO2 for Lithium-Ion Batteries. *Mater. Res. Bull.* **2017**, *96*, 491–502.

(290) Sun, Y.-K.; Myung, S.-T.; Kim, M.-H.; Prakash, J.; Amine, K. Synthesis and Characterization of Li[(Ni0.8Co0.1Mn0.1)0.8(Ni0.5Mn0.5)0.2]O2 with the Microscale Core−Shell Structure as the Positive Electrode Material for Lithium Batteries. *J. Am. Chem. Soc.* **2005**, *127*, 13411–13418.

(291) Liu, Y.; Zhang, M.; Xia, Y.; Qiu, B.; Liu, Z.; Li, X. One-Step Hydrothermal Method Synthesis of Core–Shell LiNi0. 5Mn1. 5O4 Spinel Cathodes for Li-Ion Batteries. *J. Power Sources* **2014**, *256*, 66–71.

(292) Feng, X.; Shen, Q.; Shi, Y.; Zhang, J. One-Pot Hydrothermal Synthesis of Core-Shell Structured MnCO3@ C as Anode Material for Lithium-Ion Batteries with Superior Electrochemical Performance. *Electrochim. Acta* **2016**, *220*, 391–397.

(293) Li, C.; Zhang, H. P.; Fu, L. J.; Liu, H.; Wu, Y. P.; Rahm, E.; Holze, R.; Wu, H. Q. Cathode Materials Modified by Surface Coating for Lithium Ion Batteries. *Electrochim. Acta* **2006**,

51, 3872–3883.

(294) Kosova, N. V; Devyatkina, E. T. Comparative Study of LiCoO2 Surface Modified with Different Oxides. *J. Power Sources* **2007**, *174*, 959–964.

(295) Cheng, J.; Sivonxay, E.; Persson, K. A. Evaluation of Amorphous Oxide Coatings for High-Voltage Li-Ion Battery Applications Using a First-Principles Framework. *ACS Appl. Mater. Interfaces* **2020**, *12*, 35748–35756.

(296) Lebens-Higgins, Z. W.; Halat, D. M.; Faenza, N. V; Wahila, M. J.; Mascheck, M.; Wiell, T.; Eriksson, S. K.; Palmgren, P.; Rodriguez, J.; Badway, F.; Pereira, N.; Amatucci, G. G.; Lee, T.-L.; Grey, C. P.; Piper, L. F. J. Surface Chemistry Dependence on Aluminum Doping in Ni-Rich LiNi0.8Co0.2−yAlyO2 Cathodes. *Sci. Rep.* **2019**, *9*, 17720.

(297) Liu, W.; Li, X.; Xiong, D.; Hao, Y.; Li, J.; Kou, H.; Yan, B.; Li, D.; Lu, S.; Koo, A.; Adair, K.; Sun, X. Significantly Improving Cycling Performance of Cathodes in Lithium Ion Batteries: The Effect of Al2O3 and LiAlO2 Coatings on LiNi0.6Co0.2Mn0.2O2. *Nano Energy* **2018**, *44*, 111–120.

(298) Liu, J.; Manthiram, A. Understanding the Improvement in the Electrochemical Properties of Surface Modified 5 V LiMn1.42Ni0.42Co0.16O4 Spinel Cathodes in Lithium-Ion Cells. *Chem. Mater.* **2009**, *21*, 1695–1707.

(299) Li, X.; Zhang, K.; Mitlin, D.; Yang, Z.; Wang, M.; Tang, Y.; Jiang, F.; Du, Y.; Zheng, J. Fundamental Insight into Zr Modification of Li- and Mn-Rich Cathodes: Combined Transmission Electron Microscopy and Electrochemical Impedance Spectroscopy Study. *Chem. Mater.* **2018**, *30*, 2566–2573.

(300) Li, X.; Zhang, K.; Mitlin, D.; Paek, E.; Wang, M.; Jiang, F.; Huang, Y.; Yang, Z.; Gong, Y.; Gu, L.; Zhao, W.; Du, Y.; Zheng, J. Li-Rich Li[Li1/6Fe1/6Ni1/6Mn1/2]O2 (LFNMO) Cathodes: Atomic Scale Insight on the Mechanisms of Cycling Decay and of the Improvement Due to Cobalt Phosphate Surface Modification. *Small* **2018**, *14*, 1802570.

(301) Zuo, D.; Tian, G.; Li, X.; Chen, D.; Shu, K. Recent Progress in Surface Coating of Cathode Materials for Lithium Ion Secondary Batteries. *J. Alloys Compd.* **2017**, *706*, 24–40.

(302) Kalluri, S.; Yoon, M.; Jo, M.; Liu, H. K.; Dou, S. X.; Cho, J.; Guo, Z. Feasibility of Cathode Surface Coating Technology for High-Energy Lithium-Ion and Beyond-Lithium-Ion Batteries. *Adv. Mater.* **2017**, *29*, 1605807.

(303) Aykol, M.; Kirklin, S.; Wolverton, C. Thermodynamic Aspects of Cathode Coatings for Lithium-Ion Batteries. *Adv. Energy Mater.* **2014**, *4*, 1400690.

(304) Li, H.; Zhou, H. Enhancing the Performances of Li-Ion Batteries by Carbon-Coating: Present and Future. *Chem. Commun.* **2012**, *48*, 1201–1217.

(305) Cao, Q.; Zhang, H. P.; Wang, G. J.; Xia, Q.; Wu, Y. P.; Wu, H. Q. A Novel Carbon-Coated LiCoO2 as Cathode Material for Lithium Ion Battery. *Electrochem. commun.* **2007**, *9*, 1228–1232.

(306) Ma, Z.; Shao, G.; Qin, X.; Fan, Y.; Wang, G.; Song, J.; Liu, T. Ionic Conductor Cerous Phosphate and Carbon Hybrid Coating LiFePO4 with Improved Electrochemical Properties

for Lithium Ion Batteries. *J. Power Sources* **2014**, *269*, 194–202.

(307) Tan, G.; Wu, F.; Li, L.; Chen, R.; Chen, S. Coralline Glassy Lithium Phosphate-Coated LiFePO4 Cathodes with Improved Power Capability for Lithium Ion Batteries. *J. Phys. Chem. C* **2013**, *117*, 6013–6021.

(308) Lin, H.; Zheng, J.; Yang, Y. The Effects of Quenching Treatment and AlF3 Coating on LiNi0.5Mn0.5O2 Cathode Materials for Lithium-Ion Battery. *Mater. Chem. Phys.* **2010**, *119*, 519–523.

(309) Li, G. R.; Feng, X.; Ding, Y.; Ye, S. H.; Gao, X. P. AlF3-Coated Li(Li0.17Ni0.25Mn0.58)O2 as Cathode Material for Li-Ion Batteries. *Electrochim. Acta* **2012**, *78*, 308–315.

(310) Xin, F.; Zhou, H.; Zong, Y.; Zuba, M.; Chen, Y.; Chernova, N. A.; Bai, J.; Pei, B.; Goel, A.; Rana, J.; Wang, F.; An, K.; Piper, L. F. J.; Zhou, G.; Whittingham, M. S. What Is the Role of Nb in Nickel-Rich Layered Oxide Cathodes for Lithium-Ion Batteries? *ACS Energy Lett.* **2021**, *6*, 1377–1382.

(311) Lu, C.; Wu, H.; Zhang, Y.; Liu, H.; Chen, B.; Wu, N.; Wang, S. Cerium Fluoride Coated Layered Oxide Li1.2Mn0.54Ni0.13Co0.13O2 as Cathode Materials with Improved Electrochemical Performance for Lithium Ion Batteries. *J. Power Sources* **2014**, *267*, 682–691.

(312) Hu, S.; Li, Y.; Chen, Y.; Peng, J.; Zhou, T.; Pang, W. K.; Didier, C. R.; Peterson, V. K.; Wang, H.; Li, Q. Insight of a Phase Compatible Surface Coating for Long-Durable Li-Rich Layered Oxide Cathode. *Adv. Energy Mater.* **2019**, *9*, 1901795.

(313) Zheng, J.; Liu, T.; Hu, Z.; Wei, Y.; Song, X.; Ren, Y.; Wang, W.; Rao, M.; Lin, Y.; Chen, Z.; Lu, J.; Wang, C.; Amine, K.; Pan, F. Tuning of Thermal Stability in Layered Li(NixMnyCoz)O2. *J. Am. Chem. Soc.* **2016**, *138*, 13326–13334.

(314) Ortiz-Vitoriano, N.; Drewett, N. E.; Gonzalo, E.; Rojo, T. High Performance Manganese-Based Layered Oxide Cathodes: Overcoming the Challenges of Sodium Ion Batteries. *Energy Environ. Sci.* **2017**, *10*, 1051–1074.

(315) Hu, W.; Zhang, Y.; Zan, L.; Cong, H. Mitigation of Voltage Decay in Li-Rich Layered Oxides as Cathode Materials for Lithium-Ion Batteries. *Nano Res.* **2020**, *13*, 151–159.

(316) Liao, J.-Y.; Manthiram, A. Surface-Modified Concentration-Gradient Ni-Rich Layered Oxide Cathodes for High-Energy Lithium-Ion Batteries. *J. Power Sources* **2015**, *282*, 429–436.

(317) Kasnatscheew, J.; Röser, S.; Börner, M.; Winter, M. Do Increased Ni Contents in LiNixMnyCozO2 (NMC) Electrodes Decrease Structural and Thermal Stability of Li Ion Batteries? A Thorough Look by Consideration of the Li+ Extraction Ratio. *ACS Appl. Energy Mater.* **2019**, *2*, 7733–7737.

(318) Wood, M.; Li, J.; Ruther, R. E.; Du, Z.; Self, E. C.; Meyer, H. M.; Daniel, C.; Belharouak, I.; Wood, D. L. Chemical Stability and Long-Term Cell Performance of Low-Cobalt, Ni-Rich Cathodes Prepared by Aqueous Processing for High-Energy Li-Ion Batteries. *Energy Storage Mater.* **2020**, *24*, 188–197.

(319) Xu, J.; Hu, E.; Nordlund, D.; Mehta, A.; Ehrlich, S. N.; Yang, X.-Q.; Tong, W.

Understanding the Degradation Mechanism of Lithium Nickel Oxide Cathodes for Li-Ion Batteries. *ACS Appl. Mater. Interfaces* **2016**, *8*, 31677–31683.

(320) Wentker, M.; Greenwood, M.; Leker, J. A Bottom-Up Approach to Lithium-Ion Battery Cost Modeling with a Focus on Cathode Active Materials. *Energies* **2019**, *12*, 504.

(321) Ghatak, K.; Basu, S.; Das, T.; Sharma, V.; Kumar, H.; Datta, D. Effect of Cobalt Content on the Electrochemical Properties and Structural Stability of NCA Type Cathode Materials. *Phys. Chem. Chem. Phys.* **2018**, *20*, 22805–22817.

(322) Amatucci, G. G.; Schmutz, C. N.; Blyr, A.; Sigala, C.; Gozdz, A. S.; Larcher, D.; Tarascon, J. M. Materials' Effects on the Elevated and Room Temperature Performance of CLiMn2O4 Li-Ion Batteries. *J. Power Sources* **1997**, *69*, 11–25.

(323) Zhu, X.; Li, X.; Zhu, Y.; Jin, S.; Wang, Y.; Qian, Y. LiNi0. 5Mn1. 5O4 Nanostructures with Two-Phase Intergrowth as Enhanced Cathodes for Lithium-Ion Batteries. *Electrochim. Acta* **2014**, *121*, 253–257.

(324) Julien, C. M.; Mauger, A.; Zaghib, K.; Groult, H. Optimization of Layered Cathode Materials for Lithium-Ion Batteries. *Materials (Basel).* **2016**, *9*, 595.

(325) Qian, G.; Zhang, Y.; Li, L.; Zhang, R.; Xu, J.; Cheng, Z.; Xie, S.; Wang, H.; Rao, Q.; He, Y.; Shen, Y.; Chen, L.; Tang, M.; Ma, Z.-F. Single-Crystal Nickel-Rich Layered-Oxide Battery Cathode Materials: Synthesis, Electrochemistry, and Intra-Granular Fracture. *Energy Storage Mater.* **2020**, *27*, 140–149.

(326) Park, S. H.; Park, K. S.; Sun, Y. K.; Nahm, K. S.; Lee, Y. S.; Yoshio, M. Structural and Electrochemical Characterization of Lithium Excess and Al-Doped Nickel Oxides Synthesized by the Sol–Gel Method. *Electrochim. Acta* **2001**, *46*, 1215–1222.

(327) Noh, H.-J.; Myung, S.-T.; Lee, Y. J.; Sun, Y.-K. High-Energy Layered Oxide Cathodes with Thin Shells for Improved Surface Stability. *Chem. Mater.* **2014**, *26*, 5973–5979.

(328) Guo, B.; Zhao, J.; Fan, X.; Zhang, W.; Li, S.; Yang, Z.; Chen, Z.; Zhang, W. Aluminum and Fluorine Co-Doping for Promotion of Stability and Safety of Lithium-Rich Layered Cathode Material. *Electrochim. Acta* **2017**, *236*, 171–179.

(329) Liu, Q.; Su, X.; Lei, D.; Qin, Y.; Wen, J.; Guo, F.; Wu, Y. A.; Rong, Y.; Kou, R.; Xiao, X.; Aguesse, F.; Bareño, J.; Ren, Y.; Lu, W.; Li, Y. Approaching the Capacity Limit of Lithium Cobalt Oxide in Lithium Ion Batteries via Lanthanum and Aluminium Doping. *Nat. Energy* **2018**, *3*, 936–943.

(330) Kim, U.-H.; Kuo, L.-Y.; Kaghazchi, P.; Yoon, C. S.; Sun, Y.-K. Quaternary Layered Ni-Rich NCMA Cathode for Lithium-Ion Batteries. *ACS Energy Lett.* **2019**, *4*, 576–582.

(331) Manthiram, A. An Outlook on Lithium Ion Battery Technology. *ACS Cent. Sci.* **2017**, *3*, 1063–1069.

(332) Song, D.; Hou, P.; Wang, X.; Shi, X.; Zhang, L. Understanding the Origin of Enhanced Performances in Core–Shell and Concentration-Gradient Layered Oxide Cathode Materials. *ACS Appl. Mater. Interfaces* **2015**, *7*, 12864–12872.

(333) Li, W.; Erickson, E. M.; Manthiram, A. High-Nickel Layered Oxide Cathodes for Lithium-Based Automotive Batteries. *Nat. Energy* **2020**, *5*, 26–34.

(334) Gao, T.-P.; Wong, K. W.; Fung, K. Y.; Zhang, W.; Ng, K. M. A Rational Three-Step Calcination Strategy for Synthesizing High-Quality LiNi0. 5Mn0. 3Co0. 2O2 Cathode Materials: The Key Role of Suppressing Li2O Formation. *Electrochim. Acta* **2018**, *288*, 153–164.

(335) Phadke, S.; Anouti, M. Effect of Lithium Salt Concentration on the Capacity Retention of Lithium Rich NMC Cathodes. *Electrochim. Acta* **2017**, *223*, 31–38.

(336) Ravikumar, B.; Mynam, M.; Rai, B. Effect of Salt Concentration on Properties of Lithium Ion Battery Electrolytes: A Molecular Dynamics Study. *J. Phys. Chem. C* **2018**, *122*, 8173–8181.

(337) Botte, G. G.; White, R. E.; Zhang, Z. Thermal Stability of LiPF6–EC:EMC Electrolyte for Lithium Ion Batteries. *J. Power Sources* **2001**, *97–98*, 570–575.

(338) Wang, L.; Maxisch, T.; Ceder, G. A First-Principles Approach to Studying the Thermal Stability of Oxide Cathode Materials. *Chem. Mater.* **2007**, *19*, 543–552.

(339) Hu, W.; Wang, H.; Luo, W.; Xu, B.; Ouyang, C. Formation and Thermodynamic Stability of Oxygen Vacancies in Typical Cathode Materials for Li-Ion Batteries: Density Functional Theory Study. *Solid State Ionics* **2020**, *347*, 115257.

(340) Spinner, N. S.; Love, C. T.; Rose-Pehrsson, S. L.; Tuttle, S. G. Expanding the Operational Limits of the Single-Point Impedance Diagnostic for Internal Temperature Monitoring of Lithium-Ion Batteries. *Electrochim. Acta* **2015**, *174*, 488–493.

(341) Wang, E.; Wu, H.-P.; Chiu, C.-H.; Chou, P.-H. The Effect of Battery Separator Properties on Thermal Ramp, Overcharge and Short Circuiting of Rechargeable Li-Ion Batteries. *J. Electrochem. Soc.* **2019**, *166*, A125–A131.

(342) Erickson, E. M.; Schipper, F.; Tian, R.; Shin, J.-Y.; Erk, C.; Chesneau, F. F.; Lampert, J. K.; Markovsky, B.; Aurbach, D. Enhanced Capacity and Lower Mean Charge Voltage of Li-Rich Cathodes for Lithium Ion Batteries Resulting from Low-Temperature Electrochemical Activation. *RSC Adv.* **2017**, *7*, 7116–7121.

(343) Lee, S.; Jin, W.; Kim, S. H.; Joo, S. H.; Nam, G.; Oh, P.; Kim, Y.; Kwak, S. K.; Cho, J. Oxygen Vacancy Diffusion and Condensation in Lithium-Ion Battery Cathode Materials. *Angew. Chemie* **2019**, *131*, 10588–10595.

(344) Kong, F.; Liang, C.; Wang, L.; Zheng, Y.; Perananthan, S.; Longo, R. C.; Ferraris, J. P.; Kim, M.; Cho, K. Kinetic Stability of Bulk LiNiO2 and Surface Degradation by Oxygen Evolution in LiNiO2-Based Cathode Materials. *Adv. Energy Mater.* **2019**, *9*, 1802586.

(345) Xiao, P.; Shi, T.; Huang, W.; Ceder, G. Understanding Surface Densified Phases in Ni-Rich Layered Compounds. *ACS Energy Lett.* **2019**, *4*, 811–818.

(346) Toumar, A. J.; Ong, S. P.; Richards, W. D.; Dacek, S.; Ceder, G. Vacancy Ordering in $O3$-Type Layered Metal Oxide Sodium-Ion Battery Cathodes. *Phys. Rev. Appl.* **2015**, *4*, 64002.

(347) Bianchini, M.; Wang, J.; Clément, R. J.; Ouyang, B.; Xiao, P.; Kitchaev, D.; Shi, T.; Zhang, Y.; Wang, Y.; Kim, H.; Zhang, M.; Bai, J.; Wang, F.; Sun, W.; Ceder, G. The Interplay between Thermodynamics and Kinetics in the Solid-State Synthesis of Layered Oxides. *Nat. Mater.* **2020**, *19*, 1088–1095.

(348) Reed, J.; Ceder, G.; Van Der Ven, A. Layered-to-Spinel Phase Transition in Li[Sub x]MnO[Sub 2]. *Electrochem. Solid-State Lett.* **2001**, *4*, A78.

(349) Yurkiv, V.; Sharifi-Asl, S.; Ramasubramanian, A.; Shahbazian-Yassar, R.; Mashayek, F. Oxygen Evolution and Phase Transformation in LCO Cathode: A Phase-Field Modeling Study. *Comput. Mater. Sci.* **2017**, *140*, 299–306.

(350) Sun, Y.; Zan, L.; Zhang, Y. Enhanced Electrochemical Performances of Li2MnO3 Cathode Materials via Adjusting Oxygen Vacancies Content for Lithium-Ion Batteries. *Appl. Surf. Sci.* **2019**, *483*, 270–277.

(351) Mesnier, A.; Manthiram, A. Synthesis of LiNiO2 at Moderate Oxygen Pressure and Long-Term Cyclability in Lithium-Ion Full Cells. *ACS Appl. Mater. Interfaces* **2020**, *12*, 52826–52835.

(352) Guéguen, A.; Streich, D.; He, M.; Mendez, M.; Chesneau, F. F.; Novák, P.; Berg, E. J. Decomposition of LiPF6in High Energy Lithium-Ion Batteries Studied with Online Electrochemical Mass Spectrometry. *J. Electrochem. Soc.* **2016**, *163*, A1095–A1100.

(353) Berkes, B. B.; Jozwiuk, A.; Sommer, H.; Brezesinski, T.; Janek, J. Simultaneous Acquisition of Differential Electrochemical Mass Spectrometry and Infrared Spectroscopy Data for in Situ Characterization of Gas Evolution Reactions in Lithium-Ion Batteries. *Electrochem. commun.* **2015**, *60*, 64–69.

(354) Renfrew, S. E.; McCloskey, B. D. Quantification of Surface Oxygen Depletion and Solid Carbonate Evolution on the First Cycle of LiNi0.6Mn0.2Co0.2O2 Electrodes. *ACS Appl. Energy Mater.* **2019**, *2*, 3762–3772.

(355) Lebens-Higgins, Z. W.; Chung, H.; Zuba, M. J.; Rana, J.; Li, Y.; Faenza, N. V; Pereira, N.; McCloskey, B. D.; Rodolakis, F.; Yang, W.; Whittingham, M. S.; Amatucci, G. G.; Meng, Y. S.; Lee, T.-L.; Piper, L. F. J. How Bulk Sensitive Is Hard X-Ray Photoelectron Spectroscopy: Accounting for the Cathode–Electrolyte Interface When Addressing Oxygen Redox. *J. Phys. Chem. Lett.* **2020**, *11*, 2106–2112.

(356) Gu, L.; Zhu, C.; Li, H.; Yu, Y.; Li, C.; Tsukimoto, S.; Maier, J.; Ikuhara, Y. Direct Observation of Lithium Staging in Partially Delithiated LiFePO4 at Atomic Resolution. *J. Am. Chem. Soc.* **2011**, *133*, 4661–4663.

(357) Kleiner, K.; Strehle, B.; Baker, A. R.; Day, S. J.; Tang, C. C.; Buchberger, I.; Chesneau, F.-F.; Gasteiger, H. A.; Piana, M. Origin of High Capacity and Poor Cycling Stability of Li-Rich Layered Oxides: A Long-Duration in Situ Synchrotron Powder Diffraction Study. *Chem. Mater.* **2018**, *30*, 3656–3667.

(358) Wang, S.; Hua, W.; Zhou, S.; He, X.; Liu, L. In Situ Synchrotron Radiation Diffraction Study of the Li+ de/Intercalation Behavior in Spinel LiNi0.5Mn1.5O4-δ. *Chem. Eng. J.* **2020**, *400*, 125998.

(359) Yabuuchi, N.; Kim, Y.-T.; Li, H. H.; Shao-Horn, Y. Thermal Instability of Cycled LixNi0.5Mn0.5O2 Electrodes: An in Situ Synchrotron X-Ray Powder Diffraction Study. *Chem. Mater.* **2008**, *20*, 4936–4951.

(360) Wu, J.; Yang, Y.; Yang, W. Advances in Soft X-Ray RIXS for Studying Redox Reaction States in Batteries. *Dalt. Trans.* **2020**, *49*, 13519–13527.

(361) Lebens-Higgins, Z. W.; Faenza, N. V; Radin, M. D.; Liu, H.; Sallis, S.; Rana, J.; Vinckeviciute, J.; Reeves, P. J.; Zuba, M. J.; Badway, F.; Pereira, N.; Chapman, K. W.; Lee, T.-L.; Wu, T.; Grey, C. P.; Melot, B. C.; Van Der Ven, A.; Amatucci, G. G.; Yang, W.; Piper, L. F. J. Revisiting the Charge Compensation Mechanisms in LiNi0.8Co0.2−yAlyO2 Systems. *Mater. Horizons* **2019**, *6*, 2112–2123.

(362) Jiang, M.; Key, B.; Meng, Y. S.; Grey, C. P. Electrochemical and Structural Study of the Layered, "Li-Excess" Lithium-Ion Battery Electrode Material Li[Li1/9Ni1/3Mn5/9]O2. *Chem. Mater.* **2009**, *21*, 2733–2745.

(363) Liu, H.; Bugnet, M.; Tessaro, M. Z.; Harris, K. J.; Dunham, M. J. R.; Jiang, M.; Goward, G. R.; Botton, G. A. Spatially Resolved Surface Valence Gradient and Structural Transformation of Lithium Transition Metal Oxides in Lithium-Ion Batteries. *Phys. Chem. Chem. Phys.* **2016**, *18*, 29064–29075.

(364) Jin, Y.; Kneusels, N.-J. H.; Marbella, L. E.; Castillo-Martínez, E.; Magusin, P. C. M. M.; Weatherup, R. S.; Jónsson, E.; Liu, T.; Paul, S.; Grey, C. P. Understanding Fluoroethylene Carbonate and Vinylene Carbonate Based Electrolytes for Si Anodes in Lithium Ion Batteries with NMR Spectroscopy. *J. Am. Chem. Soc.* **2018**, *140*, 9854–9867.

(365) Seymour, I. D.; Middlemiss, D. S.; Halat, D. M.; Trease, N. M.; Pell, A. J.; Grey, C. P. Characterizing Oxygen Local Environments in Paramagnetic Battery Materials via 17O NMR and DFT Calculations. *J. Am. Chem. Soc.* **2016**, *138*, 9405–9408.

(366) Kim, J.; Lee, J.; Ma, H.; Jeong, H. Y.; Cha, H.; Lee, H.; Yoo, Y.; Park, M.; Cho, J. Controllable Solid Electrolyte Interphase in Nickel-Rich Cathodes by an Electrochemical Rearrangement for Stable Lithium-Ion Batteries. *Adv. Mater.* **2018**, *30*, 1704309.

(367) Shim, J.-H.; Han, J.-M.; Lee, J.-H.; Lee, S. Mixed Electronic and Ionic Conductor-Coated Cathode Material for High-Voltage Lithium Ion Battery. *ACS Appl. Mater. Interfaces* **2016**, *8*, 12205–12210.

(368) Zachman, M. J.; Tu, Z.; Choudhury, S.; Archer, L. A.; Kourkoutis, L. F. Cryo-STEM Mapping of Solid–Liquid Interfaces and Dendrites in Lithium-Metal Batteries. *Nature* **2018**, *560*, 345–349.

(369) Choi, D.; Xiao, J.; Choi, Y. J.; Hardy, J. S.; Vijayakumar, M.; Bhuvaneswari, M. S.; Liu, J.; Xu, W.; Wang, W.; Yang, Z.; Graff, G. L.; Zhang, J.-G. Thermal Stability and Phase Transformation of Electrochemically Charged/Discharged LiMnPO4 Cathode for Li-Ion Batteries. *Energy Environ. Sci.* **2011**, *4*, 4560–4566.

(370) Gachot, G.; Ribière, P.; Mathiron, D.; Grugeon, S.; Armand, M.; Leriche, J.-B.; Pilard, S.; Laruelle, S. Gas Chromatography/Mass Spectrometry As a Suitable Tool for the Li-Ion Battery Electrolyte Degradation Mechanisms Study. *Anal. Chem.* **2011**, *83*, 478–485.

(371) Pereira, S.; Gonçalves, A.; Correia, N.; Pinto, J.; Pereira, L.; Martins, R.; Fortunato, E. Electrochromic Behavior of NiO Thin Films Deposited by E-Beam Evaporation at Room Temperature. *Sol. energy Mater. Sol. cells* **2014**, *120*, 109–115.

(372) Jungjohann, K. L.; Evans, J. E.; Aguiar, J. A.; Arslan, I.; Browning, N. D. Atomic-Scale Imaging and Spectroscopy for in Situ Liquid Scanning Transmission Electron Microscopy. *Microsc. Microanal.* **2012**, *18*, 621–627.

(373) Parent, L. R.; Gnanasekaran, K.; Korpanty, J.; Gianneschi, N. C. 100th Anniversary of Macromolecular Science Viewpoint: Polymeric Materials by In Situ Liquid-Phase Transmission Electron Microscopy. *ACS Macro Lett.* **2021**, *10*, 14–38.

(374) Weber, W. J.; Duffy, D. M.; Thomé, L.; Zhang, Y. The Role of Electronic Energy Loss in Ion Beam Modification of Materials. *Curr. Opin. Solid State Mater. Sci.* **2015**, *19*, 1–11.

(375) Hirayama, T.; Aizawa, Y.; Yamamoto, K.; Sato, T.; Murata, H.; Yoshida, R.; Fisher, C. A. J.; Kato, T.; Iriyama, Y. Advanced Electron Holography Techniques for in Situ Observation of Solid-State Lithium Ion Conductors. *Ultramicroscopy* **2017**, *173*, 64–70.

(376) Parajuli, P.; Park, H.; Kwon, B. J.; Guo, J.; Key, B.; Vaughey, J. T.; Zapol, P.; Klie, R. F. Direct Observation of Electron Beam-Induced Phase Transition in MgCrMnO4. *Chem. Mater.* **2020**, *32*, 10456–10462.

(377) Kiuchi, H.; Hikima, K.; Shimizu, K.; Kanno, R.; Toshiharu, F.; Matsubara, E. Operando Hard X-Ray Photoelectron Spectroscopy of LiCoO2 Thin Film in an All-Solid-State Lithium Ion Battery. *Electrochem. commun.* **2020**, *118*, 106790.

(378) Liu, X.; Wang, D.; Liu, G.; Srinivasan, V.; Liu, Z.; Hussain, Z.; Yang, W. Distinct Charge Dynamics in Battery Electrodes Revealed by in Situ and Operando Soft X-Ray Spectroscopy. *Nat. Commun.* **2013**, *4*, 2568.

(379) Ju, Z.; Nai, J.; Wang, Y.; Liu, T.; Zheng, J.; Yuan, H.; Sheng, O.; Jin, C.; Zhang, W.; Jin, Z.; Tian, H.; Liu, Y.; Tao, X. Biomacromolecules Enabled Dendrite-Free Lithium Metal Battery and Its Origin Revealed by Cryo-Electron Microscopy. *Nat. Commun.* **2020**, *11*, 488.

(380) Li, Y.; Li, Y.; Pei, A.; Yan, K.; Sun, Y.; Wu, C.-L.; Joubert, L.-M.; Chin, R.; Koh, A. L.; Yu, Y.; Perrino, J.; Butz, B.; Chu, S.; Cui, Y. Atomic Structure of Sensitive Battery Materials and Interfaces Revealed by Cryo–Electron Microscopy. *Science (80-.).* **2017**, *358*, 506 LP – 510.

(381) Wang, J.; Huang, W.; Pei, A.; Li, Y.; Shi, F.; Yu, X.; Cui, Y. Improving Cyclability of Li Metal Batteries at Elevated Temperatures and Its Origin Revealed by Cryo-Electron Microscopy. *Nat. Energy* **2019**, *4*, 664–670.

(382) Xu, Y.; Wu, H.; Jia, H.; Zhang, J.-G.; Xu, W.; Wang, C. Current Density Regulated Atomic to Nanoscale Process on Li Deposition and Solid Electrolyte Interphase Revealed by Cryogenic Transmission Electron Microscopy. *ACS Nano* **2020**, *14*, 8766–8775.

(383) Huang, W.; Wang, J.; Braun, M. R.; Zhang, Z.; Li, Y.; Boyle, D. T.; McIntyre, P. C.; Cui, Y. Dynamic Structure and Chemistry of the Silicon Solid-Electrolyte Interphase Visualized

by Cryogenic Electron Microscopy. *Matter* **2019**, *1*, 1232–1245.

(384) Yuan, Y.; Amine, K.; Lu, J.; Shahbazian-Yassar, R. Understanding Materials Challenges for Rechargeable Ion Batteries with in Situ Transmission Electron Microscopy. *Nat. Commun.* **2017**, *8*, 15806.

(385) Sheng, O.; Zheng, J.; Ju, Z.; Jin, C.; Wang, Y.; Chen, M.; Nai, J.; Liu, T.; Zhang, W.; Liu, Y.; Tao, X. In Situ Construction of a LiF-Enriched Interface for Stable All-Solid-State Batteries and Its Origin Revealed by Cryo-TEM. *Adv. Mater.* **2020**, *32*, 2000223.

(386) Wang, X.; Zhang, M.; Alvarado, J.; Wang, S.; Sina, M.; Lu, B.; Bouwer, J.; Xu, W.; Xiao, J.; Zhang, J.-G.; Liu, J.; Meng, Y. S. New Insights on the Structure of Electrochemically Deposited Lithium Metal and Its Solid Electrolyte Interphases via Cryogenic TEM. *Nano Lett.* **2017**, *17*, 7606–7612.

(387) Nishikawa, K.; Shinoda, K. Characterization of Electrodeposited Li Metal by Cryo-Scanning Transmission Electron Microscopy/Electron Energy Loss Spectroscopy. *J. Phys. Chem. Lett.* **2021**, *12*, 3922–3927.

(388) Xu, Y.; Wu, H.; Jia, H.; Engelhard, M. H.; Zhang, J.-G.; Xu, W.; Wang, C. Sweeping Potential Regulated Structural and Chemical Evolution of Solid-Electrolyte Interphase on Cu and Li as Revealed by Cryo-TEM. *Nano Energy* **2020**, *76*, 105040.

(389) Lee, J. Z.; Wynn, T. A.; Schroeder, M. A.; Alvarado, J.; Wang, X.; Xu, K.; Meng, Y. S. Cryogenic Focused Ion Beam Characterization of Lithium Metal Anodes. *ACS Energy Lett.* **2019**, *4*, 489–493.

(390) Bordes, A.; De Vito, E.; Haon, C.; Boulineau, A.; Montani, A.; Marcus, P. Multiscale Investigation of Silicon Anode Li Insertion Mechanisms by Time-of-Flight Secondary Ion Mass Spectrometer Imaging Performed on an In Situ Focused Ion Beam Cross Section. *Chem. Mater.* **2016**, *28*, 1566–1573.

(391) Zhang, H.; Wang, C.; Zhou, G. Ultra-Microtome for the Preparation of TEM Specimens from Battery Cathodes. *Microsc. Microanal.* **2020**, *26*, 867–877.

(392) Zankel, A.; Wagner, J.; Poelt, P. Serial Sectioning Methods for 3D Investigations in Materials Science. *Micron* **2014**, *62*, 66–78.

(393) Lu, X.; Zhao, L.; He, X.; Xiao, R.; Gu, L.; Hu, Y.; Li, H.; Wang, Z.; Duan, X.; Chen, L. Lithium Storage in Li4Ti5O12 Spinel: The Full Static Picture from Electron Microscopy. *Adv. Mater.* **2012**, *24*, 3233–3238.

(394) Schneider, N. M.; Norton, M. M.; Mendel, B. J.; Grogan, J. M.; Ross, F. M.; Bau, H. H. Electron–Water Interactions and Implications for Liquid Cell Electron Microscopy. *J. Phys. Chem. C* **2014**, *118*, 22373–22382.

(395) Grogan, J. M.; Schneider, N. M.; Ross, F. M.; Bau, H. H. Bubble and Pattern Formation in Liquid Induced by an Electron Beam. *Nano Lett.* **2014**, *14*, 359–364.

(396) Strauss, F.; Teo, J. H.; Schiele, A.; Bartsch, T.; Hatsukade, T.; Hartmann, P.; Janek, J.; Brezesinski, T. Gas Evolution in Lithium-Ion Batteries: Solid versus Liquid Electrolyte. *ACS Appl. Mater. Interfaces* **2020**, *12*, 20462–20468.

(397) Zhou, D.; Spruit, R. G.; Pen, M.; Garza, H. P.; Xu, Q. Correlative In-Situ Gas and Heating TEM: Integrating Calorimetry and Mass Spectroscopy. *Microsc. Microanal.* **2020**, *26*, 3044–3046.

(398) Unocic, K.; Griffin, M.; Yung, M.; Wegener, E.; Krause, T.; Wang, H.; Schaidle, J.; Allard, L.; Meyer, H. Operando S/TEM Reactions of Pt/TiO2 Catalysts for Catalytic Fast Pyrolysis. *Microsc. Microanal.* **2020**, *26*, 1696–1697.

(399) Zhang, H.; Karki, K.; Huang, Y.; Whittingham, M. S.; Stach, E. A.; Zhou, G. Atomic Insight into the Layered/Spinel Phase Transformation in Charged LiNi0. 80Co0. 15Al0. 05O2 Cathode Particles. *J. Phys. Chem. C* **2017**, *121*, 1421–1430.

(400) Singer, A.; Zhang, M.; Hy, S.; Cela, D.; Fang, C.; Wynn, T. A.; Qiu, B.; Xia, Y.; Liu, Z.; Ulvestad, A.; Hua, N.; Wingert, J.; Liu, H.; Sprung, M.; Zozulya, A. V; Maxey, E.; Harder, R.; Meng, Y. S.; Shpyrko, O. G. Nucleation of Dislocations and Their Dynamics in Layered Oxide Cathode Materials during Battery Charging. *Nat. Energy* **2018**, *3*, 641–647.

(401) Singh, P.; Khare, N.; Chaturvedi, P. K. Li-Ion Battery Ageing Model Parameter: SEI Layer Analysis Using Magnetic Field Probing. *Eng. Sci. Technol. an Int. J.* **2018**, *21*, 35–42.

(402) Wang, M.; Xiao, X.; Huang, X. A Multiphysics Microstructure-Resolved Model for Silicon Anode Lithium-Ion Batteries. *J. Power Sources* **2017**, *348*, 66–79.

(403) An, Z.; Shah, K.; Jia, L.; Ma, Y. Modeling and Analysis of Thermal Runaway in Li-Ion Cell. *Appl. Therm. Eng.* **2019**, *160*, 113960.

(404) Cai, L.; White, R. E. Mathematical Modeling of a Lithium Ion Battery with Thermal Effects in COMSOL Inc. Multiphysics (MP) Software. *J. Power Sources* **2011**, *196*, 5985–5989.

(405) Yu, H.; So, Y.-G.; Ren, Y.; Wu, T.; Guo, G.; Xiao, R.; Lu, J.; Li, H.; Yang, Y.; Zhou, H. Temperature-Sensitive Structure Evolution of Lithium–Manganese-Rich Layered Oxides for Lithium-Ion Batteries. *J. Am. Chem. Soc.* **2018**, *140*, 15279–15289.

TOC Graphic

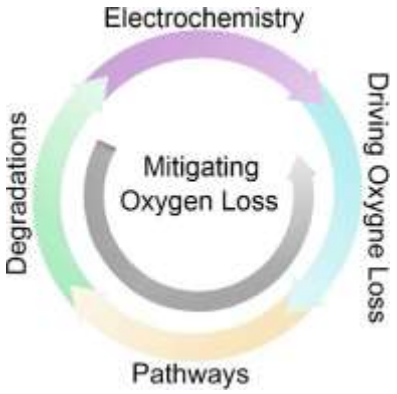
Electrochemistry
Driving Oxygne Loss
Pathways
Degradations
Mitigating
Oxygen Loss

Hanlei Zhang's Bio:

Hanlei Zhang received his Ph.D. in Materials Science & Engineering from State University of New York at Binghamton in 2019, with his mentor being Dr. Guangwen Zhou. Before joining University of Pittsburgh as a research associate, he worked as a research scholar in both Pacific Northwest National Laboratory and China University of Geosciences. He is dedicated to the application of *operando* TEM techniques in the study of energy, nano- and structural materials, as well as atomistic mechanisms governing the structure and functionality of materials.

Hao Liu's Bio:

Hao Liu received his B.Eng in Materials Engineering at the City University of Hong Kong, and M.Phil and Ph.D in Chemistry at the University of Cambridge. Following his thesis work on the phase transition of electrode materials, he joined the Structural Science Group at the Advanced Photon Source (Argonne, IL) as a postdoc to employ X-ray scattering techniques for the in-situ investigation of the function and failure of layered cathode materials for Li-ion batteries. In 2018, he joined the Chemistry Department at Binghamton University as an Assistant Professor. His group focuses on the structure-function relationship of materials for energy applications.

Louis F. Piper's Bio:

Louis F. J. Piper received his BSc and PhD in Physics at the University of Warwick, with his thesis work focusing on semiconductor surfaces and interfaces. After completing his PhD in Physics at Warwick University in 2006, he spent 4 years at the National

Synchrotron Light Source (Upton, NY) for Boston University studying a range of nitride, oxide and organic compounds using X-ray spectroscopy techniques. In 2010, he joined Binghamton University and focused his research on understanding the electrochemical, optical and transport properties of functional metal oxides using a range of novel x-ray techniques. At Binghamton University, he was Professor of Physics, Applied Physics and Astronomy and Director of the Materials Science & Engineering Program (2017 – 2020) and won the SUNY Chancellor's Award for Creative Activities (2018) for his work on understanding Li-ion electrode-electrolyte interfaces. In 2020, Louis joined WMG at University of Warwick as Professor of Electrochemical Materials and remains a visiting Professor with Binghamton University.

M. Stanley Whittingham's Bio:

M. Stanley Whittingham was born in Nottingham, England, and received his B.A. and D.Phil. degrees in Chemistry from Oxford University working with Peter Dickens. In 1968 he went to Robert A. Huggins' research group in the Materials Science Department at Stanford University as a Postdoctoral Research Associate to study fast-ion transport in solids. In 1972 he joined Exxon Research and Engineering Company to initiate a program in alternative energy production and storage. After 16 years in industry he joined the Binghamton campus of the State University of New York to initiate an academic program in Materials Chemistry. Presently he is also Distinguished Professor of Chemistry and Materials. He was awarded the Young Author Award of the Electrochemical Society in 1971, a JSPS Fellowship in the Physics Department of the University of Tokyo in 1993, the Battery Research Award of the Electrochemical Society in 2002 and was elected a

Fellow of the Electrochemical Society in 2004 and of the Materials Research Society in 2013. He received from IBA the Yeager Award for Lifetime Contributions to Lithium Battery Materials Research, 2012, and in 2010 the ACS NERM Award for Contributions to Chemistry. He was Principal Editor of the journal Solid State Ionics for 20 years. He received the 2019 Chemistry Nobel Laureate for pioneering the Li battery. He is a Fellow of The Royal Society, a Foreign Member of Real Academia de Ciencias Exactas, Físicas y Naturales de España, and an Honorary Fellow of New College, Oxford.

Guangwen Zhou's Bio

Guangwen Zhou is a Professor of Materials Science and Mechanical Engineering at the State University of New York (SUNY), Binghamton. He received a PhD in Materials Science from the University of Pittsburgh, MS in Condensed Matter Physics from Beijing University of Technology and BS in Physics from Xiangtan University, China. He conducted postdoc research at Argonne National Laboratory prior to joining SUNY Binghamton faculty in 2007. His research focuses on atomistic mechanisms of surface and interface phenomena; materials for energy storage/conversion and heterogeneous catalysis; materials stability in harsh environments including oxidation and corrosion; and materials characterization using dynamic in situ electron microscopy and spectroscopy techniques. He is a recipient of the NSF CAREER Award and SUNY Chancellor's Award for Excellence in Scholarship and Creative Activities.